2
07

This is to certify that the
dissertation entitled

# DESIGN, FABRICATION, AND TESTING OF SUPERCONDUCTING RF CAVITIES FOR HIGH AVERAGE BEAM CURRENTS

presented by

David Joseph Meidlinger

has been accepted towards fulfillment
of the requirements for the

Ph.D. degree in Physics

Walter Hartung
Major Professor's Signature

20 APRIL 2007
Date

*MSU is an affirmative-action, equal-opportunity employer*

# DESIGN, FABRICATION, AND TESTING OF SUPERCONDUCTING RF CAVITIES FOR HIGH AVERAGE BEAM CURRENTS

By

David Joseph Meidlinger

A DISSERTATION

Submitted to
Michigan State University
in partial fulfillment of the requirements
for the degree of

DOCTOR OF PHILOSOPHY

Department of Physics and Astronomy

2007

# ABSTRACT

## DESIGN, FABRICATION, AND TESTING OF SUPERCONDUCTING RF CAVITIES FOR HIGH AVERAGE BEAM CURRENTS

By

David Joseph Meidlinger

For high current applications, it is desirable for the cavity shape to have a low longitudinal loss factor and to have a high beam-breakup threshold current. This dissertation describes three different cavities designed for this purpose: a six-cell elliptical cavity for particles traveling at the speed of light, a two-cell elliptical cavity for subluminal particle speeds, and a single cell cavity which uses the TM012 mode for acceleration. SUPERFISH simulations predict the peak fields in both of the elliptical cavities will not exceed the TeSLA values by more than 10% but both will have 28.7% larger apertures. The elliptical designs assume the bunch frequency equals the accelerating mode frequency. The beam pipe radius is chosen so that the cutoff frequency is less than twice that of the accelerating mode. Hence all of the monopole and dipole higher-order modes (HOMs) that can be driven by a Fourier component of the beam have low loaded $Q$ values. This simplifies the problem of HOM damping. The TM012 cavity is predicted to have much higher peak fields than a $\pi$-mode elliptical cavity, but offers potential advantages from its simplified shape; it is essentially a circular waveguide with curved end plates. This basic shape results in easier fabrication and simplified tuning. Two prototype two-cell cavities were fabricated and tested at cryogenic temperatures without beam.

ACKNOWLEDGMENTS

I would like to thank my adviser, Walter Hartung, for his guidance, his professionalism, and his many helpful conversations throughout the years. I am the most grateful for the unequivocal support, heartfelt encouragement, and selfless sacrifice of my wife; Without her, none of this would be possible. This work was supported by the National Science Foundation and the National Superconducting Cyclotron Laboratory Fellowship.

# Contents

# List of Figures



`Images in this dissertation are presented in color.`

# List of Tables

# Chapter 1

# Introduction

Since the late nineteenth century, advances in electrical and vacuum technology have enabled scientists to probe the properties of matter by giving a beam of charged particles a large kinetic energy and then allowing that beam to collide with a target material: Advances in electrical technology enabled high voltages to be produced, which allowed particles to have high energy; Advances in vacuum technology removed most of the air so that the beam only collided with the intended target. As an example, consider an early method for producing a high voltage by creating a large direct current with a parallel bank of voltaic cells and passing the current through a large inductor. By opening the circuit, the magnetic field collapsed and, by Faraday's law, the energy stored in the magnetic field produced an electric field. Under the right conditions, the electric field was large enough for electrons to overcome the attractive forces of ions in the lattice of the metal electrode and leave the surface (a process generally known as field emission), producing a spark. By encasing the electrodes in an evacuated chamber containing a low-pressure gas, the electron beam collided with the gas atoms and produced the characteristic line spectra of the gas atoms. Further advances made even higher voltages possible, and x-rays were discovered experimentally when an electron beam with thousands of electron volts of energy collided with a solid metal electrode. These x-rays were quickly used to show by diffraction exper-

iments that the metal electrode did indeed consist of a lattice of individual atoms. In the early twentieth century, electrostic voltages on the order of a million volts could be produced with a Cockroft-Walton generator which allowed experimenters to study nuclear reactions. The use of alternating electric fields eventually proved to be superior for producing even higher beam energies corresponding to several millions of volts. The advances in accelerator physics during the first half of the twentieth century were primarily focussed on producing beams of higher energies, enabling further study of subatomic particles. However, the size of the beam also increased with beam energy, and the practical limitations on the size of a beam limited the final energy. The development of strong focussing in the 1950's separated the focussing requirements, and therefore the beam size, from the beam energy, allowing even higher energies to be achieved. The Tevatron, a modern high-energy accelerator at Fermilab, produces a final interaction energy equivalent to one trillion volts, a remarkable increase by twelve orders of magnitude in less than a century.

The goal of accelerator physics is generally to deliver a high flux of particle energy to a chosen target. This may be done with high beam energy, high beam current, or by decreasing the beam emittance (*i.e.* by decreasing the amount of phase space occupied by the beam): The particular application determines the significance of these three areas of energy, current, and emittance. For example, a hospital may use a cyclotron to artificially produce radioactive isotopes for cancer therapy. Since relatively small samples are needed, generating large beam currents at high energy is not necessary. In contrast, a facility designed for transmutation of radioactive waste [1] would ideally use the largest feasible beam current to convert waste at the highest possible rate. Facilities which use a primary beam to produce a secondary beam often need the highest possible primary beam current to produce the "brightest" secondary beam. This is the case for numerous x-ray light sources [2–4] which produce x-rays by accelerating electrons and for the Spallation Neutron Source [5] at Oak Ridge National Laboratory which uses a proton beam to produce spalled neutrons. Electron

microscopy serves as an example where there is ample beam energy and current for the application, but the beam optics limits the resolution, and therefore usefulness, of the device.

The development of superconducting cavities for accelerating charged particles has enabled new applications not previously possible with normal-conducting structures. The low dissipative power losses and high quality factor of superconducting cavities permit continuous wave (CW) operation at high field. CW operation means that energy is continuously delivered to the cavities without interruption, in contrast to pulsed operation where the power is periodically switched off and back on. Also because of the low losses, the aperture may be large, reducing interactions between the beam and higher order modes (HOMs) of the cavity. This smaller interaction has the advantage of reducing the heating of the cavity due to beam energy dissipating in the HOMs, while also increasing the threshold current for beam instabilities caused by HOMs. The advancement of superconducting technology has therefore resulted in a proliferation of the number of high beam current accelerator projects. A number of projects rely on superconducting cavities operating in an energy-recovery mode to accelerate a low-emittance electron beam for the purpose of producing x-ray radiation. The energy-recovery linear accelerator (ERL) concept has been demonstrated at Thomas Jefferson National Accelerator Facility [6]. ERL projects such as the Cornell ERL and 4GLS in Daresbury, United Kingdom are underway. Electron storage rings have historically been used for high brightness x-ray sources. Because the electrons continually circulate through the ring, a relatively small number of cavities is needed to replenish the energy lost to collisions and to radiation. The x-rays produced, whether by a linear accelerator or synchrotron, have found numerous uses in fields such as condensed matter physics, material science, biology, and medicine. Scattering experiments can reveal information about the onset of phase transitions, the atomic lattice of new materials, and the molecular structure of proteins and viruses.

Interest in superconducting cavities has increased since the recent decision to use

this technology for the proposed International Linear Collider (ILC), the highest energy linear accelerator conceived to date. This global commitment to superconducting radio frequency (SRF) cavities has spurred research and development efforts for existing accelerators and new projects [7]: the B-factories at KEK and Cornell, the CEBAF upgrade at JLAB, SNS at Oak Ridge, XFEL at DESY, ERL projects at Cornell, 4GLS at Daresbury, ELBE at Forschungszentrum Rossendorf, BESSY-ERL, and the ERL/FEL at JLAB.

Since a large part of this thesis describes the design and prototyping of cavities intended for use with an ERL, the following sections provides general background information on the development of linear accelerators. The distinction of a linear accelerator operating with energy recovery may then be better understood.

## 1.1 Linear Accelerators

The first linear accelerator (linac) using alternating fields was constructed and tested by Wideröe in 1927 [8, Sec.1.1]. A voltage of 25 kV at 1 MHz was applied to a single drift tube with the entrance and exit tubes grounded. Singly charged ions would arrive at the first accelerating gap at the peak of the radio frequency (RF) cycle, gaining 25 keV of energy. The ions then travelled through a drift tube which shielded them from the electric fields for half a RF period. The ions then emerged from the drift tube where the electric field at the next accelerating gap was at its peak value, gaining an additional 25 keV of energy. There was no reason why more gaps could not be used in the same arrangement to produce a higher final energy. Also, since the exterior of the device was grounded, multiple sections could be combined. This experiment demonstrated how alternating voltages can produce final beam energies greater than that achieved in an electrostatic accelerator.

After World War II, high power microwave sources became available. Using a higher frequency voltage source in the Wideröe design had the advantage of reducing

the length of the drift tubes needed. The disadvantage was that there would be significant radiation losses at high frequencies because of the unshielded capacative gaps in between the drift tubes [9]. A solution proposed by Alvarez was to excite a large cylindrical cavity containing drift tubes inside to shield the particle during half of the RF cycle. The Alvarez structure may be viewed as several short cylindrical cells coupled to each other and oscillating in phase. The currents flowing along the wall shared between two neighboring cells will cancel each other completely, rendering the walls superfluous.

Another major advancement in linear particle acceleration was the method of launching a travelling wave with a velocity equal to that of the particle [8, Sec.1.1]. The longitudinal electric field of the travelling wave would continually push the particle, transferring energy to it. A single cylindrical tube cannot accomplish this, since the phase velocities of the waveguide modes are greater than the speed of light. A periodic placement of disks with holes cut in the center for the beam are used to reduce the phase velocity to the speed of light. Such a structure may be viewed as a series of cylindrical cells, with each cell coupled to its nearest neighbors. This method of particle acceleration was eventually used at the Stanford Linear Accelerator Center.

An alternative method for accelerating a beam with coupled cylindrical cells is to form a series of independent multicell cavities. Each cavity is independent in the sense that it is powered separately with its own adjustable amplitude and phase. A standing wave is established in each cavity, with the electric field in each cell 180° out of phase with respect to both of its neighboring cells. The length of each cell is set to $\frac{\beta\lambda}{2}$ where $\beta$ is the particle velocity divided by the speed of light and $\lambda$ is the speed of light divided by the RF frequency. This cell length ensures that the particle is in a given cell for half of the RF period and can therefore be accelerated by the electric field in every cell. This is the method used for superconducting cavities and has the operational advantage of greater flexibility: each individual cavity may be adjusted as needed or even shut down if necessary.

One of the primary characteristics of all linacs is the ability to produce high-energy, low-emittance beams. In circular machines such as electron storage rings, the emittance of the beam is determined by the synchrotron radiation emitted in the bending magnets. The emittance of the beam in a linac is essentially determined by the source, not the machine lattice. Some other advantages of linacs [8, Sec.1.1]:

1. Strong focusing can easily be provided to confine a high-intensity beam.
2. The beam experiences a single pass, avoiding resonances which can occur when beam is fed back in a circular machine.
3. The final energy of the beam is not limited by synchrotron radiation losses since there are no bending magnets.
4. Injection and extraction are simpler.
5. A linac can operate at any duty factor, including CW.

### 1.1.1 Energy Recovery Linacs

Superconducting cavities allow large electron beam currents which can be used for applications such x-ray free electron lasers (FELs) and electron cooling of a heavy ion beam. The low emittance electron beam of a linear accelerator is capable of producing very bright, coherent x-rays. However, FELs only convert approximately 1% of the available beam energy to x-ray energy. For example, a 10 kW laser would require 1 MW of beam power, with 990 kW of beam power left over after lasing. Simply disposing this high-energy, high-power beam would be economically unattractive and would produce enormous amounts of radioactivity at the beam dump. Energy recovery is a method to generate a high-energy, high-current beam using only a small fraction of the available beam power.

The concept is to first start with a high-energy, low-emittance source of electrons, such as an RF or DC photo-injector. Electron bunches leave the source with speeds

near that of light. They are then further accelerated, providing the power that the application, such as lasing or cooling, will later extract. The bunches are then accelerated to high energy through a main linac consisting of several independently phased cavities. After reaching high energy, the bunches are used for the intended application. Bending magnets then recirculate the beam back to the main linac. The bunches enter the main linac 180° out of phase with the RF, so the bunches decelerate, giving their energy back to the cavity mode. When the bunches leave the main linac, they have the same relatively low energy they started with when they left the source, and can be safely dumped. The cavities in the main linac act as energy storage devices. The energy stored in the accelerating mode will decrease during the first half of an RF period when a bunch is being accelerated, but the energy will be restored during the second half of the RF cycle as a subsequent bunch is decelerated. Averaged over an RF period, the net beam loading of the cavity is zero, and power must only be supplied to compensate for the dissipative losses of the cavities. The situation is analogous to reactive elements in a lumped circuit, where the instantaneous power going into or out of the element can be large but there is no net power consumed by the lossless element.

## 1.2 Radio-Frequency Cavities

An RF cavity is essentially a closed metal structure which uses one of its electromagnetic modes of oscillation to accelerate beam. A standing wave is established in which the field pattern has an electric field pointing primarily in the direction that the beam travels. By driving the cavity at the mode's resonant frequency, the relatively small field of the forward travelling wave from the power supply can result in a large field in the cavity. The only power which must be externally supplied is to compensate for the dissipative losses of the metal walls of the cavity and the power transferred to the beam. The basic shape used for superconducting cavities and the salient features of

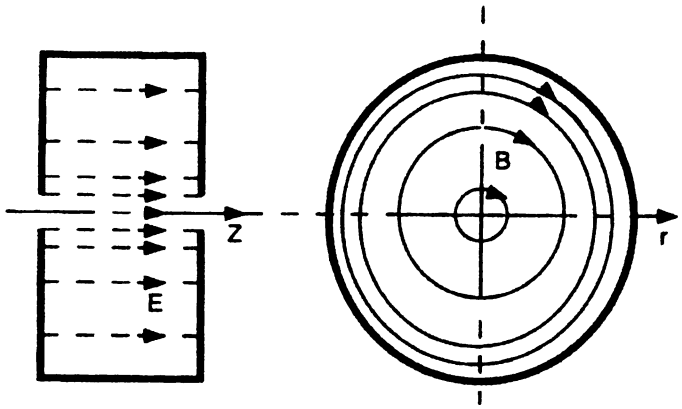


Figure 1.1: The TM010 field pattern has a large electric field along the beam axis [8, Sec.1.2].

the accelerating mode field pattern will be described in the following section.

### 1.2.1 The Elliptical Cavity

As the name implies, the pillbox cavity is a cylinder with the diameter larger than the radius. The lowest frequency resonant mode for such a structure is the TM010 mode. As can be seen in Figure 1.1, the electric field along the beam axis is very high. The electric field is highest along the beam axis if there is no hole to allow the beam to pass through the cavity. When an opening is made for the beam pipe, the peak electric field will occur along the surface of this opening. The peak magnetic field occurs at a radius that is approximately 73% of the cavity's outer radius. For superconducting cavities, all corners are rounded with an elliptical profile. The purpose of rounding the corner at the iris is to reduce the peak electric field and therefore reduce the chance of field emission ocurring at high field. The purpose of rounding the outer equatorial edge is to avoid hard multipacting barriers and reduce the peak magnetic field on the surface of the cavity. Large surface magnetic fields are maintained by large electrical currents on the surface and therefore locally dissipate large amounts of power. If this heating occurs near a defect in the material, the increased temperature could initiate a thermal instability which destroys the superconducting state. Figure 1.2 shows the

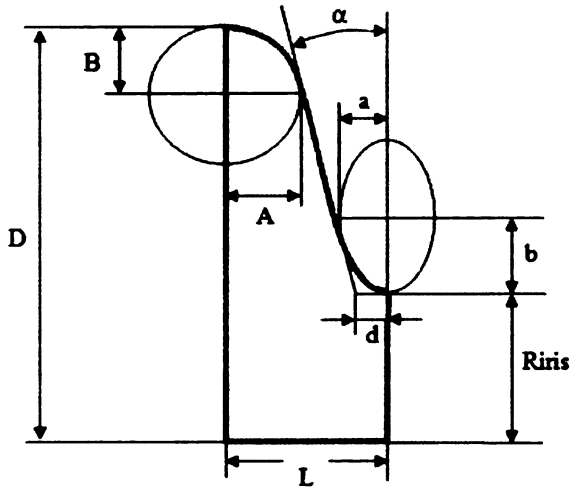


Figure 1.2: An elliptical profile is used for the equator and iris of the cell with a straight section connecting the two ellipses.

geometrical parameters which characterize the cell shape:

$D =$ equatorial radius of the cell. It is adjusted primarily to tune the resonant frequency to the design value.

$L =$ half-length of the cell. It is set equal to $\frac{\beta\lambda}{4}$, where $\beta$ is the particle velocity divided by the velocity of light and $\lambda$ is the speed of light divided by the resonant frequency.

$R_{\text{iris}} =$ beam tube radius.

$\alpha =$ angle that the straight section connecting the two ellipses makes with the vertical.

$d =$ location where the straight section would intersect the beam tube if both were continued indefinitely.

$a =$ minor semi-axis of the iris ellipse.

$A =$ minor semi-axis of the equator ellipse.

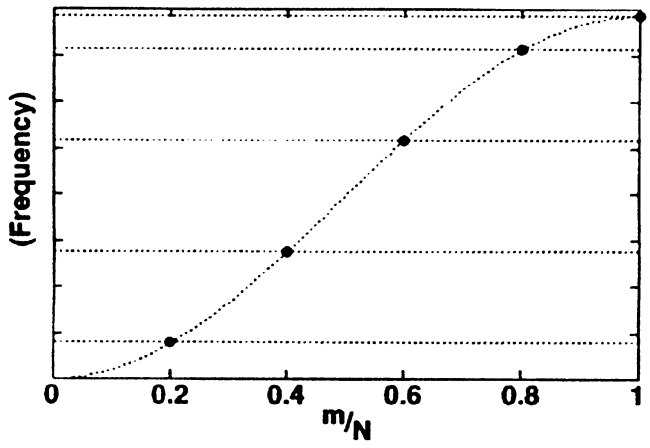


Figure 1.3: The dispersion diagram for the TM01 passband [10, p.134].

$b =$ major semi-axis of the iris ellipse.

$B =$ major semi-axis of the equator ellipse.

Several elliptical cells are welded together to form a single multicell cavity. The TM010 mode of a cell couples to those of its neighboring cells via the electric field. This coupling causes the TM010 mode to split into a passband of closely spaced modes equal in number to the number of cells. The dispersion diagram for the TM010 passband of a hypothetical 5-cell cavity is shown in Figure 1.3.

The width of the passband (range of frequencies of the modes in the passband) is determined by the strength of the cell-to-cell coupling, which is primarily determined by the iris radius. A longer cavity with more cells would have more modes in the same frequency range, therefore increasing the number of cells reduces the difference in frequency between the adjacent modes of the passband.

Figure 1.4 shows an example of a 5-cell cavity, illustrating the electric field lines for the accelerating mode. The accelerating mode has the highest frequency in the passband and is referred to as the $\pi$-mode since the phase advances by 180° from cell to cell. The field pattern in each cell is TM010 for the accelerating mode. The higher-order modes have their own passbands, and the field pattern in each cell is

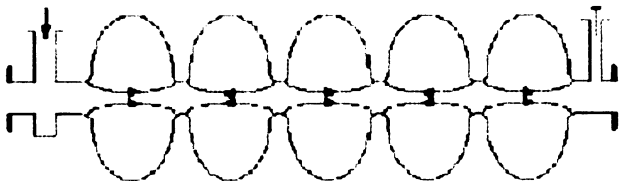

Figure 1.4: Conceptual schematic showing the alternating electric field lines of the $\pi$-mode [10, p.4].

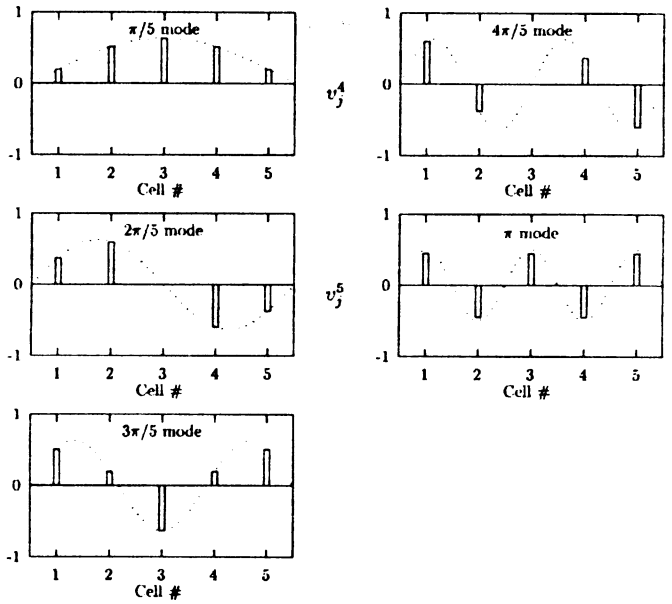


Figure 1.5: The modes within a passband are characterized by the sinusoidal variation in electric field amplitude from cell to cell [10, p.132].

that of the HOM. All passbands will contain as many modes as there are cells. For the $m^{\text{th}}$ passband mode, the amplitude in the $j^{\text{th}}$ cell is proportional to

$$\sin\left[m\pi\left(\frac{2j-1}{2N}\right)\right] \tag{1.1}$$

where $N$ is the total number of cells in the cavity. This variation in cell amplitude is graphically depicted in Figure 1.5 for the case of a 5-cell cavity.

### 1.2.2 Superconductivity

There are several advantages to using superconducting (SC) cavities made from bulk niobium instead of normal-conducting (NC), copper cavities for particle accelerators [10, Sec.1.2]. High gradients may be achieved with both technologies, but the mechanical properties of copper and the quality of the cavity vacuum degrade if a copper cavity's temperature exceed approximately 100°C. To prevent excessive heating at high gradients, the duty factor is typically lower than 1%. Because the $Q$ of a SC cavity is typically $10^5$ times greater than a copper structure, high gradients are possible at high duty cycles and up to CW operation. The high $Q$ of SC cavities reduces the power dissipated, in the range of 1-10 W. This power must be dissipated at cryogenic temperatures however, which is inherently inefficient due to the low Carnot efficiency of refrigeration at or below 4 K. When the Carnot efficiency is combined with the mechanical efficiency of the refrigeration system, the overall efficiency is approximately 0.3%. However, when the efficiency of the klystron used to power a NC cavity is taken into account, a SC structure would require approximately 200 times less AC wall power to operate than a NC structure at the same duty cycle. The high $Q$ also enables larger cavity apertures to be used, which significantly reduces any interactions between the beam and the cavity HOMs. The beam will deposit less energy in the HOMs; The HOMs will degrade the beam emittance less and higher beam currents can be accelerated before HOM-induced beam instabilities arise. Larger apertures thus allow for higher average beam currents.

SC cavities bring not only improved performance but also additional challenges. To attain high $Q$'s, cleanliness during fabrication and processing of bulk niobium SC cavities is crucial. The power per unit area dissipated locally on the inner surface of a cavity is given by the expression

$$P = \frac{1}{2} R_s H^2, \tag{1.2}$$

where $H$ is the local magnetic field on the surface and $R_s$ is the surface resistance. The BCS theory of superconductivity predicts that at temperatures below half of the critical temperature, the surface resistance has the approximate form [10, Sec.3.4],

$$R_{\mathrm{BCS}} = A\omega^2 \, \mathrm{e}^{-\frac{\Delta(0)}{k_{\mathrm{B}}T}}. \tag{1.3}$$

Here $\omega$ is the angular frequency of the RF, $\Delta(0)$ is the energy gap at zero temperature, $k_{\mathrm{B}}$ is Boltzmann's constant, $T$ is the temperature, and $A$ is a temperature and frequency independent constant whose value is determined by the properties of the material. The surface resistance measured in experiments is consistent with the BCS prediction, therefore lowering the temperature of the helium bath can dramatically reduce the surface resistance. However, the decrease in surface resistance with temperature does not continue indefinitely. Eventually the measured surface resistance reaches a constant value independent of temperature. This residual resistance ($R_o$) is essentially due to impurities and foreign material on the niobium surface or trapped magnetic flux. The surface resistance of a SC cavity therefore has the form

$$R_{\mathrm{S}} = A\omega^2 \, \mathrm{e}^{-\frac{\Delta(0)}{k_B T}} + R_{\mathrm{O}}. \tag{1.4}$$

The value of $R_{\mathrm{O}}$ typically attained is in the range of 10 to 20 n$\Omega$. For cavities operating at frequencies around 1.5 GHz, the temperature must be less than or equal to approximately 2 K for the BCS resistance to drop below this level [10, Sec.9.1]. To achieve these low limiting values of surface resistance and to ensure adequate rates of heat transfer to the helium bath, careful precautions must be taken.

The BCS resistance has a strong dependence on temperature, so it is desirable to increase the rate of heat transfer through the bulk niobium as much as possible to ensure that the temperature rise from the outer to inner surface is as small as possible. Electron-phonon scattering essentially determines the value of both the

electrical and thermal conductivities of a metal at room temperature. These conductivities are higher at cryogenic temperatures since the number of phonons is reduced [10, Sec.3.2.1]. The conductivities eventually saturate at limiting values where electron scattering with impurities dominates. Since it is relatively easy to make precise measurements of electrical conductivity, the ratio of the saturated electrical conductivity to the room-temperature electrical conductivity is used as a measure of the purity of bulk niobium. High values of this ratio, called the residual resistance ratio (RRR), are therefore desirable. High purity niobium is expensive, with the cost roughly proportional to the RRR: A RRR of 250 is typical. During the stamping of elliptical half-cells and machining of weld preps, care must be taken to avoid using steel. This prevents any iron from contaminating the surface and providing magnetic flux to be trapped during cooldown. Also, high permeability metal must be used to shield the cavity from stray magnetic fields (including the Earth's magnetic field) during cooldown. Convential welding techniques such as tungsten-inert-gas (TIG) welding would contaminate the niobium surface, so all welds are typically done with an electron beam under high vacuum. If hydrogen concentrations are above 2 ppm by weight, then there is a risk of a lossy hydride forming on the Nb surface at temperatures between 60 K and 150 K [10, Sec.9.4]. The acid used for etching the cavity surface must be chilled below 20°C to avoid excessive hydrogen to be released on the surface. Baking at 700°C to 900°C under vacuum is necessary to ensure that hydrogen concentrations are low enough to preclude precipitaion of hydrides. An alternative approach to baking, which was adopted here at MSU, mitigates the formation of the hydride by cooling down quickly (approximately 1 hour) while in the temperature range of 60 K to 150 K.

### 1.2.3 Issues Driving Cavity Design

Superconducting cavities are an ideal choice when large beam currents and high duty cycles are desired. These characteristics combined with the efficient use of beam power

in an ERL have lead to a number of projects striving for 100's of mA of electron beam current for use in a high power FEL or for electron cooling. The primary challenges for the cavity at these high beam currents are to reduce the amount of beam-induced HOM power as much as possible and to effectively damp the dipole HOMs that are primarily responsible for the multipass beam breakup (BBU) instabilities that ultimately limit the maximum available beam current.

If a particle enters a cavity on the central axis when a dipole HOM has been excited, then the particle will leave with a deflection in the horizontal or vertical direction. The optics of the recirculation line will cause the tranverse momentum imparted to the particle by the HOM to result in the particle entering the cavity with a transverse displacement when it returns for deceleration. The transverse offset can cause the particle to further excite the HOM and this process can continue until the particle collides with the cavity wall [6]. The threshold current at which a multipass BBU occurs is predicted to the correct order of magnitude by the expression [11]

$$I_{\text{th}} = \frac{-2pc}{e\left(\frac{R}{Q}\right)QkM_{12}}. \tag{1.5}$$

Here $p$ is the momentum of the particle, $c$ is the speed of light, $e$ is the charge of the electron, $\frac{R}{Q}$ is the shunt impedance of the HOM, $Q$ is the quality factor of the HOM, $k = \frac{\omega}{c}$ is the wavenumber of the HOM, and $M_{12}$ is the transfer matrix element relating the transverse momentum at the cavity exit to the transverse displacement of the particle at the entrance of the same cavity during the next pass. The HOM of concern is the one which corresponds to the lowest threshold current. The beam-induced power dissipated by a longitudinal HOM is given by

$$P = \frac{\omega I|q|}{4}\left(\frac{R}{Q}\right), \tag{1.6}$$

where $\omega$ is the angular frequency of the HOM, $q$ is the bunch charge, $I$ is the average

beam current, and $\frac{R}{Q}$ is the shunt impedance of the HOM. The goal is then to minimize both the $\frac{R}{Q}$ and loaded $Q$ values for all HOMs which interact with the beam. In contrast, strong interactions between the cavity accelerating mode and the beam are desirable for efficient acceleration, so the general aim for this case is to maximize both $\frac{R}{Q}$ and $Q$.

### 1.2.4 Outline

This dissertation will present the design of three superconducting cavities intended for acceleration of beams with high average current. Elliptical cavities with two cells and six cells have been designed for use in an ERL. The two-cell cavity is designed for use as an injector cavity, operating without energy recovery. The six-cell cavity is suitable for acceleration in the main linac. The third cavity shape is a single cell suitable for use in an electron storage ring. All three cavities have large apertures, which reduce the HOM heat load and increase the threshold currents for beam instabilities. Chapter 2 describes the solution for general cavity fields and the key figures of merit used to describe these field patterns. The figures of merit allow one to compare different cavity shapes and judge which shape is better for an intended application. The figures of merit are therefore important for understanding the design goals of the three different cavities. Chapter 3 describes the design criteria for the shape of the six-cell cavity and the method used to meet these criteria. Here the basic approach to avoiding HOM-induced beam instabilities is described and will constitute one of the primary design criteria. Chapter 4 describes the design and shape of the two-cell cavity. Two copies of the two-cell cavity shape were prototyped and tested. The details of this fabrication process and the results of the tests are presented. Chapter 6 describes the basic concept of using a HOM in a single cell cavity as the accelerating mode. The purpose of using the HOM is that it allows the aperture of the cavity to increase significantly without significantly increasing the heat dissipated in the accelerating mode. The increased aperture has the advantage of diminishing interactions between

the undesirable HOMs and the beam and therefore enabling larger beam currents to be used.

# Chapter 2

# Superconducting Cavity Design

The main design considerations for superconducting radio-frequency cavities will be described in this chapter. We begin with the waveguide modes in Section 2.1 and then proceed to cavities in Section 2.2; the standing wave fields in a cavity can be thought of as being the superposition of travelling wave fields of a waveguide. The effects of wall losses and coupling ports are discussed in Sections 2.3.3 and 2.3.4. The main figures of merit that guided the design of the 2-cell, 6-cell, and HOM cavity are then described in Section 2.4.

## 2.1 Waveguide Modes

A brief review of the electromagnetic field patterns of waveguides will be useful for describing closed cavities, which may be viewed as a waveguide with its ends shorted, and for understanding how the energy stored in cavity modes may couple out through a beam pipe, which may be viewed as a waveguide with a circular cross section.

The modes of propagation in a waveguide can be derived from Maxwell's equations, as done in several texts [12–14], as well as in Appendix A. The starting point is a hollow tube of constant cross-section with vacuum inside and conducting walls. A solution of Maxwell's equations is sought with the fields varying sinusoidally in time

as $e^{j\omega t}$. In the vacuum region with no source terms and perfectly conducting walls, the electric and magnetic field both satisfy the wave equation. Solutions are sought which vary sinusoidally in the axial direction ($z$) as $e^{-j\beta z}$. One can then separate out the axial component of the fields from the transverse components.

In order to satisfy the boundary conditions imposed by the conducting walls of the waveguide, longitudinal field components must be introduced. This is in contrast to plane travelling waves, for which the components are purely transverse. Likewise, the simple proportionality between the frequency and the wavenumber of a plane wave becomes more complicated for a waveguide.

An expression relating the frequency of a waveguide mode to its wavenumber generally has the form

$$k_0^2 = k_c^2 + \beta^2 \tag{2.1}$$

This Pythagorean relation between the critical wavenumber $k_c$, the free space wavenumber $k_o$, and the axial wavenumber $\beta$ in Equation (2.1) provides a simple physical interpretation of a waveguide mode. Below a critical frequency, $\omega_c = ck_c$, a mode may only be excited evanescently. Evanescent is a general term used to describe modes which diminish rapidly beyond the point of excitation and therefore do not propagate electromagnetic energy. Mathematically, these evanescent solutions arise in the same way that exponentially diminishing state functions appear in a classically forbidden region as solutions to the Schrödinger equation. Physically, the mode responds as a combination of a lumped inductor and lumped capacitor: The mode can only store energy during one half of an RF cycle before delivering it back to the RF source, similar to the behavior of a lumped capacitor or inductor in low frequency circuits. At $\omega_c$, a standing wave is established in the transverse direction. The wave is a superposition of a wave travelling away from the axis and a reflected wave travelling toward the axis. The type of mode and the shape of the waveguide cross section will

determine the value of $k_c$ when the appropriate solution to the wave equation is found. For frequencies above $\omega_c$, a wave travelling in the axial direction is established with the wavenumber $\beta$. The field pattern can therefore be viewed as the superposition of two travelling waves which propagate in equal but opposite directions slightly off axis and continually reflect off of the walls of the waveguide. The two waves travel with the free-space wavenumber $\mathbf{k_0}$ which has $k_c$ as a transverse component and $\beta$ as an axial component.

The notion of impedance is a useful but potentially confusing one for RF applications, since the term impedance is used to describe four different, but related, quantities [13, page 188].

### Intrinsic Impedance

There is the intrinsic impedance, $\eta$, of the medium which is the ratio $\frac{E}{H}$ for a plane wave in the medium.

### Wave Impedance

The wave impedance, $Z$, is the ratio $\frac{e}{h}$ of the transverse fields for a travelling wave of a given mode and its value is a function of the waveguide geometry, the medium of the guide, and the mode number.

### Characteristic Impedance

The characteristic impedance, $Z_o$, is uniquely defined only for transmission lines as the ratio of the voltage to current in a travelling wave. The product of voltage and current is the instantaneous power passing through the transverse plane and may be calculated by integrating the Poynting vector over the area of the plane. The characteristic impedance is therefore a function of the transmission line geometry and the wave impedance. Since voltage and current may not be uniquely defined for a waveguide mode, the characteristic impedance is not uniquely defined either. In

this thesis, the characteristic impedance for waveguide modes is chosen to be equal to the wave impedance. Once voltage or current is defined in terms of the transverse fields of the mode, the remaining quantity must be defined such that the product of voltage and current is equal to the integrated energy flux at the plane. A suitable set of reference transverse fields, $\mathbf{E}_t$ and $\mathbf{H}_t$, may be normalized such that $\mathbf{E}_t$ is real and satisfies the expression

$$\int E_t^2 \mathrm{d}a = 1. \tag{2.2}$$

Let the transverse fields of the mode then be expressed as,

$$\mathbf{e} = v\mathbf{E}_t \tag{2.3}$$

$$\mathbf{h} = iZ\mathbf{H}_t \tag{2.4}$$

with the coefficients calculated by evaluating the following integrals,

$$v = \int (\mathbf{e} \cdot \mathbf{E}_t)\, \mathrm{d}a \tag{2.5}$$

$$i = Z^2 \int (\mathbf{h} \cdot \mathbf{H}_t)\, \mathrm{d}a. \tag{2.6}$$

These coefficients serve as an equivalent voltage and current since the ratio of $v$ to $i$ is equal to the wave impedance and the product of $v$ and $i$ is equal to the total power passing through the plane,

$$\frac{e}{h} = \frac{vE_t}{iZH_t} = \frac{v}{i} \tag{2.7}$$

$$\frac{1}{2}\mathrm{Re}\left[\int (\mathbf{e} \times \mathbf{h}) \cdot \mathrm{da}\right] = \frac{1}{2}\mathrm{Re}\left(vi^* \int E_t^2 \mathrm{d}a\right) = \frac{1}{2}\mathrm{Re}(vi^*). \tag{2.8}$$

### Load Impedance

The impedance of a load, $Z_l$, attached to a transmission line or waveguide is generally not equal to the characteristic impedance. In this case, a travelling wave will be par-

tially reflected at the load and a standing wave will be established in the transmission line or waveguide. By measuring the amplitude and phase of the reflected wave, the impedance of the load may be established. The load impedance is defined as the ratio of voltage to current for the superposition of the forward and reverse travelling waves,

$$Z_l = \left( \frac{V_f + V_r}{I_f - I_r} \right). \tag{2.9}$$

Here $V_f, I_f$ and $V_r, I_r$ are the voltage and current of a wave travelling in the forward and reverse direction respectively.

### Circular Waveguide Modes

The case of a circular waveguide is of particular interest for the present work. In the case of a conducting wall of circular cross-section, separation of variables may be done in cylindrical coordinates. The solutions to the wave equation are trigonometric functions of the azimuthal coordinate, while the radial dependence takes the form of Bessel functions.

As in all waveguides, the modes of propagation in the circular waveguide can be classified as either TE (transverse electric, with zero longitudinal electric field) or TM (transverse magnetic, with zero longitudinal magnetic field). The lowest modes of each classification are referred to as TE11 and TM01.

For the TM01 mode in a circular waveguide of radius $a$, we obtain $k_c = 2.405/a$, and the fields in a cylindrical coordinate system (radial, axial, and azimuthal coordinate = $\rho$,$z$, and $\phi$, respectively) are

$$e_z = J_0 \left( 2.405 \frac{\rho}{a} \right). \tag{2.10}$$

$$\mathbf{e} = -\frac{\mathrm{j}\beta}{k_c} J_1 (k_c \rho)\, \mathbf{n}_\rho \tag{2.11}$$

$$\mathbf{h} = h_\phi \mathbf{n}_\phi = -\frac{\mathrm{j}\, k_o}{\eta k_c} J_1 (k_c \rho)\, \mathbf{n}_\phi. \tag{2.12}$$

## 2.2 General Expansion of Electromagnetic Fields Inside a Hollow Cavity

Any electric or magnetic field pattern in a cavity may be expressed as a superposition of the corresponding field of the eigenmodes. This representation of the cavity fields is useful for determining the cavity figures of merit and for modelling interactions between the cavity and the beam. The derivation of the modal expansion of the fields can be found in the text by Slater [14], and in Appendix B. The results are summarized briefly in this section.

Any vector field is determined uniquely once the values of the curl and divergence are known at all points. A general vector field may then be described as a combination of two different sets of orthogonal functions. One set contains solenoidal functions for which the divergence is zero. The other set contains irrotational functions for which the curl is zero.

Considering a hollow cavity with boundary conditions imposed on its bounding surface, one can solve for a set of orthonormal functions (solenoidal fields $\mathbf{E}_a$ and $\mathbf{H}_a$ and an irrotational field $\mathbf{F}_a$). The electric field, magnetic field, current density, and charge density in the cavity can then be expressed as linear combinations of these functions:

$$\mathbf{E} = \sum_a (e_\mathrm{a}\mathbf{E}_\mathrm{a} + f_\mathrm{a}\mathbf{F}_\mathrm{a}) \tag{2.13}$$

$$\mathbf{H} = \sum_a h_\mathrm{a}\mathbf{H}_\mathrm{a} \tag{2.14}$$

$$\mathbf{J} = \sum_a (j_\mathrm{a}\mathbf{E}_\mathrm{a} + g_\mathrm{a}\mathbf{F}_\mathrm{a}) \tag{2.15}$$

$$\rho = \sum_a r_\mathrm{a}\psi_\mathrm{a}. \tag{2.16}$$

In order for the functions to be orthonormal, they cannot have the same dimensions as the actual electric and magnetic fields. The properly dimensioned electric

fields $\widetilde{E}_a$ and $\widetilde{H}_a$ are related to the orthonormal functions via

$$\mathbf{E_a} = \sqrt{\frac{\epsilon}{2U_a}}\widetilde{\mathbf{E_a}} \tag{2.17}$$

$$\mathbf{H_a} = \sqrt{\frac{\mu}{2U_a}}\widetilde{\mathbf{H_a}}. \tag{2.18}$$

With the proper mathematical operations, Maxwell's equations can be written in terms of the coefficients and the appropriate surface integrals:

$$\kappa_a g_a = \frac{dr_a}{dt} \tag{2.19}$$

$$k_a h_a = j_a + \oint (\mathbf{E_a} \times \mathbf{H}) \cdot \mathbf{da} + \epsilon \frac{de_a}{dt} \tag{2.20}$$

$$k_a e_a = -\oint (\mathbf{E} \times \mathbf{H_a}) \cdot \mathbf{da} - \mu \frac{dh_a}{dt}. \tag{2.21}$$

The time evolution of the coefficients $e_a$ and $h_a$ can be described in terms of ordinary differential equations:

$$\frac{d^2 e_a}{dt^2} + \omega_a^2 e_a = -\frac{1}{\epsilon}\frac{d}{dt}\left[j_a + \oint (\mathbf{E_a} \times \mathbf{H}) \cdot \mathbf{da}\right] - \frac{\omega_a^2}{k_a}\left[\oint (\mathbf{E} \times \mathbf{H_a}) \cdot \mathbf{da}\right] \tag{2.22}$$

$$\frac{d^2 h_a}{dt^2} + \omega_a^2 h_a = \frac{\omega_a^2}{k_a}\left[j_a + \oint (\mathbf{E_a} \times \mathbf{H}) \cdot \mathbf{da}\right] - \frac{1}{\mu}\frac{d}{dt}\left[\oint (\mathbf{E} \times \mathbf{H_a}) \cdot \mathbf{da}\right]. \tag{2.23}$$

When the terms on the right hand side are zero, the fields oscillate sinusoidally in time with angular frequency $\omega_a$, as one would expect. The first term on the right hand side, $j_a$ allows for energy to be transferred into or out of the cavity via the beam. The other terms allow for power to be lost in the walls of the cavity, or for the power to arrive into or to leak out of the cavity through an external port.

## 2.3 Applications

### 2.3.1 Lossless Cavity

If the cavity walls and dielectric material are both lossless, then Equations (2.22) and (2.23) reduce to

$$\frac{d^2 h_{\mathbf{a}}}{dt^2} + \omega_a^2 h_{\mathbf{a}} = \frac{d^2 e_{\mathbf{a}}}{dt^2} + \omega_a^2 e_{\mathbf{a}} = 0. \tag{2.24}$$

An excited cavity mode will therefore freely oscillate sinusoidally with angular frequency, $\omega_a = \frac{k_{\mathbf{a}}}{\sqrt{\epsilon\mu}}$. These frequencies and field patterns correspond to the eigenvalues found in numerical simulations.

### 2.3.2 Cavity with Losses and Quality Factor

There are various energy-loss mechanisms which are proportional to the square of the cavity fields and contribute to the overall $Q$ of the cavity. Of these "quadratic" losses, heating of the dielectric medium filling the cavity is not directly relevant to the work of this thesis since the cavities addressed are all operated under vacuum. However, a brief description of the effects of dielectric losses is useful for clarifying the treatment of resistive wall losses, which will be addressed in the next section. A cavity with a lossy dielectric has finite conductivity and will therefore have an associated volume current, $\mathbf{J} = \sigma\mathbf{E}$, which has expansion coefficients

$$j_{\mathbf{a}} = \sigma e_{\mathbf{a}}. \tag{2.25}$$

Substituting Equation (2.25) into Equation (2.22) results in

$$\frac{d^2 e_{\mathbf{a}}}{dt^2} + \frac{\sigma}{\epsilon}\frac{de_{\mathbf{a}}}{dt} + \omega_a^2 e_{\mathbf{a}} = 0. \tag{2.26}$$

A similar equation is produced by combining Equations (2.21), (2.23), and (2.25):

$$\frac{d^2 h_{\mathrm{a}}}{dt^2} + \frac{\sigma}{\epsilon}\frac{dh_{\mathrm{a}}}{dt} + \omega_a^2 h_{\mathrm{a}} = 0. \tag{2.27}$$

Either equation may be solved by assuming a sinusoidal solution with complex angular frequency. The equation for the angular frequency of free, damped oscillations is then

$$\omega_a^2 - \omega^2 + \frac{\mathrm{j}\sigma}{\epsilon}\omega = 0, \tag{2.28}$$

which has the solution

$$\omega = \mathrm{j}\frac{\omega_a}{2Q} \pm \omega_a\sqrt{1 - \left(\frac{1}{2Q}\right)^2} \qquad \text{with } Q = \frac{\epsilon\omega_a}{\sigma}. \tag{2.29}$$

The electromagnetic field pattern of the modes with dielectric losses are identical to those of the loss-free case, but the damping produces a frequency shift which is of order $\frac{1}{Q^2}$. This is the familiar shift in natural frequency of a damped harmonic oscillator.

The general definition of the $Q$ of a mode with angular frequency $\omega$, stored energy $U$, and power loss $P$ is

$$Q = \frac{\omega U}{P}. \tag{2.30}$$

Dissipative losses are not the only mechanism that causes stored energy to leave a cavity mode. There must be some means of coupling power to the cavity, and this port therefore also provides a means for energy to leak out of the cavity. Also, a charge bunch passing through the cavity can be accelerated and therefore take energy from the mode. If the cavity mode initially starts with some stored energy and is allowed to oscillate freely without being driven by an external RF generator, then the power leaving the cavity through the various loss mechanisms will cause the cavity fields to

decay. The rate of decay is faster when the lost power is larger,

$$\frac{dU}{dt} = -P = -\frac{\omega U}{Q} \tag{2.31}$$

$$U(t) = U_o \mathrm{e}^{-\frac{\omega t}{Q}} . \tag{2.32}$$

The rate of decay of the cavity fields may be found from the fact that the stored energy is proportional to the square of the cavity fields:

$$\sqrt{U(t)} = \sqrt{U_o}\,\mathrm{e}^{-\frac{\omega t}{2Q}} . \tag{2.33}$$

The rate of decay is a function of what is referred to as the loaded $Q$ (denoted $Q_L$), which is the $Q$ calculated using the total power leaving through all mechanisms. It also has significance when the cavity mode is being driven under steady state conditions, since the impedance of the mode is the Fourier transform of the impulse response. The loaded $Q$ is therefore also equal to the ratio of the resonant frequency to the mode bandwidth. Just as the loaded $Q$ is defined in terms of the total power leaving the mode, separate $Q$ values are defined for each loss mechanism. The loaded $Q$ may then be written as a function of the separate $Q$'s,

$$P = P_0 + P_{\mathrm{ext}} + P_{\mathrm{b}} \tag{2.34}$$

$$\frac{P}{\omega U} = \frac{P_0}{\omega U} + \frac{P_{\mathrm{ext}}}{\omega U} + \frac{P\mathrm{b}}{\omega U} \tag{2.35}$$

$$\frac{1}{Q_{\mathrm{L}}} = \frac{1}{Q_0} + \frac{1}{Q_{\mathrm{ext}}} + \frac{1}{Q_{\mathrm{b}}}. \tag{2.36}$$

The intrinsic $Q$ (denoted $Q_0$) , external $Q$ (denoted $Q_{\mathrm{ext}}$), and the beam $Q$ (denoted $Q_{\mathrm{b}}$ are due to dissipative losses, power leaving through any external ports, and power taken by an accelerated beam respectively.

### 2.3.3 Wall Losses

All hollow, metallic cavities will experience some power loss due to the non-zero surface resistance of the metal walls. There will be a small tangential electric field on the metal surface and a correspondingly small energy flux into the metal. These modes must then in general be represented by a superposition of the $\mathbf{E_a}$'s or $\mathbf{H_a}$'s since a single member of either set will not satisfy the correct boundary conditions. However, for all cases of interest the wall losses will be small and therefore the fields in the interior of the cavity for a given mode will be essentially identical with those of a single member of the $\mathbf{E_a}$'s or $\mathbf{H_a}$'s. The rest of the superposition consists of a sum of small, higher-order corrections to satisfy the boundary conditions at the surface. Since the tangential electric field on the metal surface is non-zero, it is convenient to use Equation (2.23), setting the $\mathbf{E_a} \times \mathbf{H}$ term equal to zero:

$$\frac{d^2 h_\mathbf{a}}{dt^2} + \omega_a^2 h_\mathbf{a} = -\frac{1}{\mu}\frac{d}{dt}\left[\oint (\mathbf{E} \times \mathbf{H_a}) \cdot d\mathbf{a}\right]. \tag{2.37}$$

The intrinsic impedance of a material in which the conduction current is much larger than the displacement current is

$$\eta = (1 + \mathrm{j})\sqrt{\frac{\omega\mu}{2\sigma}}. \tag{2.38}$$

The intrinsic impedance may be used to eliminate the electric field from the previous equation:

$$\frac{d^2 h_\mathbf{a}}{dt^2} + \omega_a^2 h_\mathbf{a} = -\frac{\eta}{\mu}\frac{d}{dt}\left[\oint (\mathbf{H} \cdot \mathbf{H_a})\, \mathrm{d}a\right]. \tag{2.39}$$

If there are no losses, the magnetic field pattern would be that of $\mathbf{H_a}$ and the frequency would be $\omega_a$. In the case of wall losses, the frequency of the mode will be slightly different due to the higher-order contributions of the superposition. To find the $n^{\mathrm{th}}$-order correction to the frequency requires use of the $(n-1)^{\mathrm{th}}$-order correction of the field pattern. For all cases of interest, the wall losses are small enough that a first-

order correction to the frequency is sufficient and therefore the zero-order correction to the magnetic field may be used in the equation above,

$$\mathbf{H} = h_{\mathrm{a}}\mathbf{H}_{\mathrm{a}}, \tag{2.40}$$

$$\frac{d^2h_{\mathrm{a}}}{dt^2} + \omega_a^2 h_{\mathrm{a}} + \frac{\eta}{\mu}\frac{d}{dt}\left[h_{\mathrm{a}} \oint (\mathbf{H}_{\mathrm{a}} \cdot \mathbf{H}_{\mathrm{a}})\,\mathrm{d}a\right] = 0, \tag{2.41}$$

$$\frac{d^2h_{\mathrm{a}}}{dt^2} + \frac{\eta}{\mu}\left(\oint H_{\mathrm{a}}^2 \mathrm{d}a\right)\frac{dh_{\mathrm{a}}}{dt} + \omega_a^2 h_{\mathrm{a}} = 0. \tag{2.42}$$

Assuming that $h_{\mathrm{a}}$ varies harmonically with time, the equation above may be solved for the complex angular frequency,

$$\omega = \frac{\mathrm{j}\eta}{2\mu}\oint H_{\mathrm{a}}^2 \mathrm{d}a \pm \frac{1}{2}\sqrt{4\omega_a^2 + \left(\frac{\eta}{\mu}\oint H_{\mathrm{a}}^2 \mathrm{d}a\right)^2}. \tag{2.43}$$

The first term on the right side contains an imaginary portion and is therefore responsible, to first order, for the decay of the fields. We can therefore solve for the Q after substituting Equation (2.38) using $\omega_{\mathrm{r}}$ (the real part of $\omega$),

$$\frac{\omega_{\mathrm{r}}}{Q} = \mathrm{Im}\left[\frac{j\eta}{\mu}\oint H_{\mathrm{a}}^2 \mathrm{d}a\right], \tag{2.44}$$

$$\frac{\omega_{\mathrm{r}}}{Q} = \sqrt{\frac{\omega_{\mathrm{r}}}{2\mu\sigma}}\oint H_{\mathrm{a}}^2 \mathrm{d}a, \tag{2.45}$$

$$\Rightarrow \frac{1}{Q} = \sqrt{\frac{1}{2\omega_{\mathrm{r}}\sigma\mu}}\oint H_{\mathrm{a}}^2 \mathrm{d}a = \frac{\delta}{2}\oint H_{\mathrm{a}}^2. \tag{2.46}$$

The distance at which the fields in the metal have decayed by the factor $\frac{1}{e}$ is defined to be $\delta$, the skin depth. The expression, correct to first order in $\frac{1}{Q}$, for the angular frequency of a mode with wall losses is then

$$\omega = \omega_a - \frac{\omega_a}{2Q} + \frac{\mathrm{j}\omega_a}{2Q}. \tag{2.47}$$

In this case there is a first-order shift in the natural frequency of the mode, in contrast to the second-order shift in the case of dielectric losses.

### 2.3.4 External Ports and External Q

A beam pipe must be added to a cavity in order to introduce charge bunches to be accelerated, and the beam pipe may also be viewed as a waveguide with a circular cross section. According to Equation (2.1), a waveguide mode will not have a real axial wave number, and therefore propagate energy down the guide, unless it is driven above a cutoff frequency which is determined from the value of the critical wavenumber for the guide mode. To ensure that the cavity accelerating mode only excites the beam pipe modes evanescently, the frequency of the accelerating mode is set below the lowest cutoff frequency of the beam pipe. Various cavity HOMs are excited by the beam as it passes through and it is desirable to minimize this excitation as much as possible to prevent instabilities which arise from further interactions with the beam and to reduce the cryogenic load. Ideally, a cavity would have the frequencies of all HOMs above the cutoff frequency of the beam pipe: It would then be possible for the HOM fields to propagate away from the cavity and be damped by a resistive load or coupling antenna connected to an external load. In addition to high frequency, a mode must have sufficient coupling to the beam pipe mode for damping to be effective. The coupling strength is quantified by the value of $Q_{\text{ext}}$. A low $Q_{\text{ext}}$ value means that a relatively large amount of power leaks out of the cavity through the beam pipe.

The system of interest is a hollow cavity connected to a circular waveguide. We wish to develop an expression for the input impedance seen looking into the cavity through the guide. The surface, $S'$, is far enough away from the cavity that evanescent fields are negligible. Then the cavity field, $\mathbf{E_a}$, at the surface $S'$ is proportional to the transverse field of the waveguide mode

$$\mathbf{E_a} = v\mathbf{E_t}. \tag{2.48}$$

The magnetic field at $S'$ may then be expressed as

$$\mathbf{H} = iZ\mathbf{H}_\mathrm{t}. \tag{2.49}$$

The value of $i$ determines the input current which excites the cavity mode, resulting in a particular value of $e_\mathrm{a}$ and therefore $v$. The ratio of the equivalent voltage to the equivalent current at $S'$ is the input impedance of the cavity seen at $S'$. To calculate this impedance it is necessary then to formulate an expression for $e_\mathrm{a}$. Equation (2.22) reduces to

$$\frac{d^2 e_\mathrm{a}}{dt^2} + \omega_a^2 e_\mathrm{a} = -\frac{1}{\epsilon}\frac{d}{dt}\left[\oint (\mathbf{E_a} \times \mathbf{H}) \cdot \mathrm{da}\right]. \tag{2.50}$$

Substituting Equations (2.48) and (2.49) into the integral, we obtain

$$-\oint (\mathbf{E_a} \times \mathbf{H}) \cdot \mathrm{da} = -\int_{S'} [(v\mathbf{E}_\mathrm{t}) \times (iZ\mathbf{H}_\mathrm{t})] \cdot (-\mathbf{n}\mathrm{d}a) = vi, \tag{2.51}$$

so that Equation (2.22) becomes

$$\frac{d^2 e_\mathrm{a}}{dt^2} + \omega_a^2 e_\mathrm{a} = \frac{1}{\epsilon}\frac{d\,(vi)}{dt}. \tag{2.52}$$

The driving term, $i$, will vary sinusoidally, so $e_\mathrm{a}$ is also assumed to vary sinusoidally with the same frequency,

$$-\omega^2 e_\mathrm{a} + \omega_a^2 e_\mathrm{a} = \left(\frac{\mathrm{j}\omega}{\epsilon}\right) vi. \tag{2.53}$$

We can now solve for $e_\mathrm{a}$

$$e_\mathrm{a} = \frac{\left(\frac{\mathrm{j}\omega}{\epsilon}\right) vi}{\omega_a^2 - \omega^2} \tag{2.54}$$

or, equivalently,

$$e_\mathrm{a} = \frac{\frac{vi}{\epsilon\omega_a}}{\mathrm{j}\left(\frac{\omega}{\omega_a} - \frac{\omega_a}{\omega}\right)}. \tag{2.55}$$

Now that the electric field has been determined, $\mathbf{E} = e_{\mathrm{a}}\mathbf{E}_{\mathrm{a}}$, the impedance may be calculated by forming the ratio of the amplitudes of the transverse electric and magnetic fields, $Z_l = \frac{E}{H}$. Substituting Equations (2.49) and (2.48) produces

$$Z_l = \frac{e_{\mathrm{a}} v E_{\mathrm{t}}}{iZH_{\mathrm{t}}} = \frac{e_{\mathrm{a}} v}{i}, \tag{2.56}$$

$$Z_l = \frac{\frac{v^2}{\epsilon\omega_a}}{\mathrm{j}\left(\frac{\omega}{\omega_a} - \frac{\omega_a}{\omega}\right)}. \tag{2.57}$$

The total impedance generally consists of a sum over all of the cavity modes,

$$Z_l = \sum_a \frac{\frac{v_a^2}{\epsilon\omega_a}}{\mathrm{j}\left(\frac{\omega}{\omega_a} - \frac{\omega_a}{\omega}\right)}, \tag{2.58}$$

however for frequencies near a particular mode the contribution from other modes is small and it is convenient to lump them together into an additional term $Z_\alpha$:

$$Z_l = \frac{\frac{v^2}{\epsilon\omega_a}}{\mathrm{j}\left(\frac{\omega}{\omega_a} - \frac{\omega_a}{\omega}\right)} + Z_\alpha. \tag{2.59}$$

The natural frequency of the cavity mode may be found by terminating the guide with the characteristic impedance, $Z_o$. The impedance described by Equation (2.59) will then be the negative of this value,

$$Z_l = -Z_o, \tag{2.60}$$

$$\frac{\frac{v^2}{\epsilon\omega_a}}{\mathrm{j}\left(\frac{\omega}{\omega_a} - \frac{\omega_a}{\omega}\right)} + Z_\alpha + Z_o = 0, \tag{2.61}$$

$$\frac{\frac{v^2}{\epsilon\omega_a}}{Z_o + Z_\alpha} + \mathrm{j}\left(\frac{\omega}{\omega_a} - \frac{\omega_a}{\omega}\right) = 0. \tag{2.62}$$

It is convenient to define $g + \mathrm{j}\,b = \frac{Z}{Z_o + Z_\alpha}$ and $\frac{1}{Q_V} = \frac{v^2}{\epsilon\omega_a Z}$ where $Z$ is the wave

impedance of the guide,

$$\omega^2 - \omega_a^2 + \left(\frac{\omega_a b}{Q_V}\right)\omega - \left(\frac{jg\omega_a}{Q_V}\right)\omega = 0, \tag{2.63}$$

$$\omega^2 - \left[\frac{\mathrm{j}\,\omega_a\,(g + \mathrm{j}\,b)}{Q_V}\right]\omega - \omega_a^2 = 0. \tag{2.64}$$

The cavity mode "rings" down as energy is propagated out through the guide, providing a loss in an otherwise lossless cavity. The cavity frequency will then generally be complex, with the imaginary part describing the decay rate of the mode. Solving the last equation for $\omega$ results in

$$\omega = \frac{j\,(g + \mathrm{j}\,b)\,\omega_a}{2Q_V} \pm \sqrt{\omega_a^2 - \left[\frac{\omega_a\,(g + \mathrm{j}\,b)}{2Q_V}\right]^2}. \tag{2.65}$$

To first order in $\frac{(g+\mathrm{j}\,b)}{2Q_V}$, the frequency is then

$$\omega = \omega_a + \frac{\mathrm{j}\,\omega_a\,(g + \mathrm{j}\,b)}{2Q_V}. \tag{2.66}$$

The impedance $Z_\alpha$ represents the combined impedance of the other cavity modes which will be small if the resonant frequencies of the other modes are all sufficiently far from the mode of interest. However, a surface $S'$ may always be found where $Z_\alpha = 0$ and therefore $g = \frac{Z}{Z_o}$. In this case $Q_V = Q_{ext}$.

The derivation of the input admittance is similar to that of the input impedance. The magnetic field on a surface, $S$, is defined in terms of the transverse magnetic field of the dominant waveguide mode and the electric field imposed on $S$ is defined in terms of the transverse electric field of the dominant waveguide mode,

$$\mathbf{H_a} = i\mathbf{H_t} \tag{2.67a}$$

$$\mathbf{E} = vY\mathbf{E_t}. \tag{2.67b}$$

The driving term in Equation (2.23) is evaluated,

$$\int_S (\mathbf{E} \times \mathbf{H_a}) \cdot \mathrm{da} = \int_S [(vY\mathbf{E_t}) \times (i\mathbf{H_t})] \cdot (-\mathbf{n}da) = -vi \tag{2.68}$$

The value of $h_\mathrm{a}$ may then be obtained using Equation (2.23),

$$h_\mathrm{a} = \frac{\frac{vi}{\mu\omega_a'}}{\mathrm{j}\left(\frac{\omega}{\omega_a'} - \frac{\omega_a'}{\omega}\right)}. \tag{2.69}$$

By using Equations (2.67a) and (2.67b) the expression for the input admittance becomes

$$Y_l = \frac{H}{E} = \frac{h_\mathrm{a} i H_\mathrm{t}}{vYE_\mathrm{t}} = \frac{h_\mathrm{a} i}{v} = \frac{\frac{i^2}{\mu\omega_a'}}{\mathrm{j}\left(\frac{\omega}{\omega_a'} - \frac{\omega_a'}{\omega}\right)}. \tag{2.70}$$

The general expression for the input admittance when a particular mode dominates is then

$$Y_l = \frac{\frac{i^2}{\mu\omega_a}}{\mathrm{j}\left(\frac{\omega}{\omega_a} - \frac{\omega_a'}{\omega}\right)} + Y_\alpha. \tag{2.71}$$

To solve for the frequency of free oscillations it is convenient to define $r + \mathrm{j}\,x = \frac{Y}{Y_o + Y_\alpha}$ and $\frac{i^2}{\mu\omega_a Y} = \frac{1}{Q_I}$. If $S$ is terminated with a characteristic admittance, $Y_o$, then

$$Y_l = -Y_o, \tag{2.72}$$

$$\mathrm{j}\left[\left(\frac{\omega}{\omega_a'}\right) - \left(\frac{\omega_a'}{\omega}\right) + \left(\frac{x}{Q_I}\right)\right] + \frac{r}{Q_I} = 0, \tag{2.73}$$

$$\Rightarrow \omega = \omega_a' + \frac{\mathrm{j}\,(r + \mathrm{j}\,x)\,\omega_a'}{2Q_I}. \tag{2.74}$$

A location may be found for $S$ such that $Y_\alpha = 0$. In this case, $x = 0$, $r = 1$, and $Q_I = Q_{ext}$.

The fields of a lossless cavity with a waveguide port may be found numerically and two different solutions can be found corresponding to the different boundary

conditions of $S$ and $S'$. Since $S$ and $S'$ have the same location, the value of $Q_{ext}$ will not generally be equal to $Q_V$ or $Q_I$. From Equations (2.66) and (2.74) a single expression for the $Q_{ext}$ may be formulated with the assumption that $\omega_a$ and $\omega'_a$ are both approximately equal to $\omega_o$,

$$\frac{1}{Q_{\text{ext}}} = \frac{g}{Q_V} \tag{2.75}$$

$$\frac{1}{Q_{\text{ext}}} = \frac{r}{Q_I} \tag{2.76}$$

$$\Rightarrow (g+r)\,Q_{\text{ext}} = Q_V + Q_I. \tag{2.77}$$

The sum $g + r$ may then be expanded and simplified:

$$g + \mathrm{j}b = \frac{Z}{Z_o + Z_\alpha} = \frac{Z}{R_o + \mathrm{j}\,X_\alpha} = \frac{Z\,(R_o - \mathrm{j}\,X_\alpha)}{R_o^2 + X_\alpha^2} \Rightarrow g = \frac{R_o Z}{R_o^2 + X_\alpha^2}. \tag{2.78}$$

$$r + \mathrm{j}x = \frac{Y}{Y_o + Y_\alpha} = \frac{Y}{G_o + \mathrm{j}\,B_\alpha} = \frac{Y\,(G_o - \mathrm{j}\,B_\alpha)}{G_o^2 + B_\alpha^2} \Rightarrow r = \frac{G_o Y}{G_o^2 + B_\alpha^2}. \tag{2.79}$$

$$g + r = \frac{R_o Z}{R_o^2 + X_\alpha^2} + \frac{\frac{1}{R_o Z}}{\frac{1}{R_o^2} + \frac{1}{X_\alpha^2}} = \frac{R_o Z + \frac{R_o^2 X_\alpha^2}{R_o Z}}{R_o^2 + X_\alpha^2}. \tag{2.80}$$

If the guide is connected to a matched load then $Z = R_o$ and

$$g + r = \frac{R_o^2 + X_\alpha^2}{R_o^2 + X_\alpha^2} = 1. \tag{2.81}$$

Substituting this value into Equation (2.77) gives a relatively simple expression for calculating the $Q$ of a cavity mode from the results of two simulations,

$$Q_{\text{ext}} = Q_V + Q_I = \frac{\epsilon \omega_a R_o}{v^2} + \frac{\mu \omega_a}{i^2 R_o}. \tag{2.82}$$

There are two potential advantages when applying Slater's method to the problem of predicting external $Q$s from simulation results:

- for the case of a heavily damped mode, $\omega_a \approx \omega'_a \approx \omega_o$ is no longer valid but

an expression similar to Equation (2.82) may still be derived with a frequency dependent coefficient next to $Q_I$ and $Q_V$;

- the method may, in principle, be extended to describe the case in which the resonance of neighboring modes overlaps with that of the mode of interest.

### 2.3.5 Slater's Theorem

If the field pattern of a cavity mode is slightly perturbed by introducing a small metallic bead or by slightly deforming the cavity at a small localized region on the boundary, then the mode frequency will shift by an amount which depends on the field level at the location of the perturbation. If the perturbation is small, then the new field pattern will be a superposition of primarily the old field pattern with small contributions from other modes. The surface currents associated with the discontinuity in the magnetic field on the perturbed boundary will be the source of a driving term on the right sides of Equations (2.22) and (2.23),

$$\oint (\mathbf{E_a} \times \mathbf{H}) \cdot \mathrm{d}\mathbf{a}', \tag{2.83}$$

where the integration is over the area of the small perturbed volume. To find the first-order shift in frequency, the zeroth-order field pattern ($\mathbf{H} \approx h_\mathrm{a}\mathbf{H_a}$) is used:

$$\oint (\mathbf{E_a} \times \mathbf{H}) \cdot \mathrm{d}\mathbf{a}' = h_\mathrm{a} \oint (\mathbf{E_a} \times \mathbf{H_a}) \cdot \mathrm{d}\mathbf{a}', \tag{2.84}$$

and the divergence theorem is used to convert the surface integral to a volume integral:

$$h_\mathrm{a} \oint (\mathbf{E_a} \times \mathbf{H_a}) \cdot \mathrm{d}\mathbf{a}' = h_\mathrm{a} \int \nabla \cdot (\mathbf{E_a} \times \mathbf{H_a})\, \mathrm{d}\tau'. \tag{2.85}$$

Using Equations (B.1) and (B.2), the volume integral may be written as,

$$h_{\mathrm{a}} \int \left[\mathbf{H}_{\mathrm{a}} \cdot (\nabla \times \mathbf{E}_{\mathrm{a}}) - \mathbf{E}_{\mathrm{a}} \cdot (\nabla \times \mathbf{H}_{\mathrm{a}})\right] \mathrm{d}\tau' = h_{\mathrm{a}} k_{\mathrm{a}} \int \left(H_{\mathrm{a}}^2 - E_{\mathrm{a}}^2\right) \mathrm{d}\tau'. \tag{2.86}$$

Substituting this form into Equation (2.23) and assuming harmonic time variation of the fields results in

$$-\omega^2 + \omega_{\mathrm{a}}^2 = \omega_{\mathrm{a}}^2 \int \left(H_{\mathrm{a}}^2 - E_{\mathrm{a}}^2\right) \mathrm{d}\tau'. \tag{2.87}$$

The first order fractional change in the mode frequency therefore becomes,

$$\frac{\omega - \omega_{\mathrm{a}}}{\omega_{\mathrm{a}}} \approx \frac{1}{2} \int \left(H_{\mathrm{a}}^2 - E_{\mathrm{a}}^2\right) \mathrm{d}\tau'. \tag{2.88}$$

## 2.4 Cavity Figures of Merit

There is no single, universal cavity shape which will always provide the best performance for any given accelerator. Each cavity shape is optimized as needed to achieve the design goals of a particular machine. The optimization generally requires a compromise between competing design goals. The purpose of this section is to briefly describe some figures of merit which are used in the design of the cavity shape.

### 2.4.1 Accelerating Gradient and Transit Time Factor

A charged particle passing through a cavity will gain energy from the accelerating mode. The voltage gain is calculated by integrating the electric field of the mode along the path of the particle,

$$V = \int_{s_i}^{s_f} \mathbf{E}(\mathrm{s}, t) \cdot \mathrm{ds} = \mathrm{Re}\left[\int_{t_i}^{t_f} \mathrm{e}^{\mathrm{j}(\omega t + \phi)} \, \mathbf{E}(\mathrm{s}) \cdot \mathbf{v}(t) \mathrm{d}t\right]. \tag{2.89}$$

The cavity fields oscillate sinusoidally with angular frequency $\omega$ and phase $\phi$. The integral in Equation (2.89) cannot be evaluated further without knowing how $\mathbf{E}$ varies

along the particle's path. Additionally, the particle's path is not known without solving the full dynamical problem. Once the particle trajectory is known and $V$ is calculated, then an average accelerating gradient may be defined as

$$E_{acc} = \frac{V}{d} \tag{2.90}$$

with $d = \int_{s_i}^{s_f} \mathrm{d}s$. The actual voltage gain is always lower than would be expected for the case in which the same electric field pattern was somehow able to remain fixed at its maximum amplitude and pointing in the direction of particle motion at all times while the particle travelled through the cavity. The transit time factor, $T$, is a measure of how much the voltage gain is reduced because of the variation of the cavity field with time. The transit time factor is therefore always less than or equal to 1 and is defined by the following relation,

$$V = T \int_{s_i}^{s_f} |\mathbf{E}(\mathrm{s})| \cdot \mathrm{ds}. \tag{2.91}$$

If the particle enters the cavity with a speed close to the speed of light or if the energy gain is small, then the particle velocity may be approximated as being constant. This approximation simplifies the calculation of the voltage gain, however the variation of the cavity field with time must still be taken into account,

$$V = \mathrm{Re}\left[\mathrm{e}^{\mathrm{j}\,\phi} \int_{s_i}^{s_f} \mathrm{e}^{\mathrm{j}(\frac{\omega}{v})s}\, \mathbf{E} \cdot \mathbf{n_s} ds\right]. \tag{2.92}$$

Since the portion of the accelerating mode fields that penetrate into the beam pipe diminishes exponentially with the distance away from the cavity opening, the limits of the integral in Equation (2.92) may be extended to infinity. The integral is then equal to the Fourier transform of the electric field component along the particle path,

$$V = \mathrm{Re}\left[\mathrm{e}^{\mathrm{j}\,\phi} F\left(\frac{\omega}{v}\right)\right]. \tag{2.93}$$

The Fourier transform is generally a complex function of the real variable $\frac{\omega}{v}$ and the RF phase $\phi$ is an independent parameter. Equation (2.93) indicates that the voltage gain varies sinusoidally as a function of RF phase, as one would expect. The maximum voltage gain is achieved when the RF phase is set equal to the negative of the phase of the Fourier transform. In this case, the voltage gain is equal to the magnitude of the Fourier transform of the electric field along the particle path:

$$V = \left| F\left(\frac{\omega}{v}\right) \right|. \tag{2.94}$$

### 2.4.2 Quality Factor and Geometry Factor

By combining Equations (2.18), (2.45), and (2.30), an expression for the power dissipated in the cavity walls may be derived:

$$P_o = \frac{\omega U}{Q_o} = \frac{1}{2}\sqrt{\frac{\omega\mu}{2\sigma}} \oint \widetilde{H_{\mathrm{a}}}^2 \mathrm{d}a. \tag{2.95}$$

An expression for the intrinsic $Q$ may now be written in terms of the magnetic field integrals:

$$U = \frac{\mu_o}{2} \int \widetilde{H_{\mathrm{a}}}^2 \mathrm{d}\tau, \tag{2.96}$$

$$R_s = \sqrt{\frac{\omega\mu}{2\sigma}}, \tag{2.97}$$

$$Q_o = \frac{\omega\mu_o}{R_s} \left( \frac{\int \widetilde{H_{\mathrm{a}}}^2 \mathrm{d}\tau}{\oint \widetilde{H_{\mathrm{a}}}^2 \mathrm{d}a} \right). \tag{2.98}$$

$R_s$ is the surface resistance of the metal boundary (either normal conducting, for which Equation (2.97) is valid, or superconducting). When it is factored out of the right side of Equation (2.98), what remains is referred to as the geometry factor,

$$G = \frac{\omega\mu_o \int \widetilde{H_{\mathrm{a}}}^2 \mathrm{d}\tau}{\oint \widetilde{H_{\mathrm{a}}}^2 \mathrm{d}a}. \tag{2.99}$$

The value of the geometry factor is determined by the shape of the cavity, regardless of the size. It is seen to be proportional to the ratio of cavity volume to surface area weighted by the value of the square of the magnetic field magnitude. For the cavity to have a large intrinsic $Q$, there must be a large amount of stored energy with very little dissipated power. The total stored energy is equal to twice the average energy stored in the magnetic field, and the dissipated power depends on the square magnitude of the magnetic field on the surface of the cavity. Therefore large values of $G$ are desirable since it indicates that the energy stored in the magnetic field is concentrated in a region with comparatively little field on the inner surface of the cavity. So to maximize $Q_o$, the shape should be optimized such that the volume containing the high magnetic field region is maximized while the surface magnetic field is minimized.

### 2.4.3 Geometric Shunt Impedance

Just as the geometry factor is a size-independent parameter which characterizes the magnetic field of a cavity mode, the geometric shunt impedance is a parameter which characterizes the electric field. Borrowing terminology from lumped circuit theory, the shunt impedance $R_0$ of a mode is defined in terms of the dissipated power and the voltage gain:

$$P_0 = \frac{V^2}{R_0}. \tag{2.100}$$

When this expression for $P_o$ is substituted into Equation (2.30) and $V$ expanded using Equation (2.91), the ratio of the shunt impedance to $Q_o$ is

$$\frac{R_0}{Q_0} = \frac{V^2}{\omega U} = \frac{\left(T \int_{s_i}^{s_f} |\mathbf{E}|(\mathbf{s}) \cdot \mathrm{ds}\right)^2}{\omega U}. \tag{2.101}$$

The ratio $\frac{R_0}{Q_0}$ is referred to as the geometric shunt impedance. The stored energy in the mode is equal to twice the average energy stored in the electric field. Large values

of $\frac{R_0}{Q_0}$ are desirable then since it indicates that the energy stored in the electric field is concentrated in the field tangential to the particle path. However, Equation (2.101) shows that transit time effects also affect the value of $\frac{R_0}{Q_0}$. For example, the cavity could be perturbed slightly in a high magnetic field region causing a significant shift in the resonant frequency of the mode with comparatively little change in the electric field pattern. The detuning of the mode would cause the voltage to drop and therefore lower $\frac{R_0}{Q_0}$. The single parameter which affects the $\frac{R_0}{Q_0}$ the most is the radius of the beam tube. A larger beam tube pulls the electric field lines away from the central axis and therefore lowers the shunt impedance.

### 2.4.4 Surface Electric Field Ratio

Field emission of electrons will reduce the cavity $Q$ and reduce the maximum achievable accelerating gradient. High pressure rinsing the interior of the cavity with ultrapure water reduces the risk of field emission but does not completely eliminate the possibility. The peak surface electric field, $E_{\mathrm{p}}$, typically occurs near the iris of an elliptical cavity. A larger beam tube radius generally produces a larger $E_{\mathrm{p}}$ value for a given $E_{\mathrm{acc}}$ value. A low value of $\frac{E_{\mathrm{p}}}{E_{\mathrm{acc}}}$ is generally desirable since it reduces the possibility of field emission.

### 2.4.5 Surface Magnetic Field Ratio

A large peak surface magnetic field, $B_p$, is undesirable for two reasons. First, a large magnetic field near a defect in the cavity surface can cause a small region of the cavity to go normal conducting. The increased resistance causes the temperature to further increase, which in turn causes more of the surrounding niobium to go normal conducting. This process continues rapidly, causing the entire inner surface to go normal conducting with the cavity fields simultaneously collapsing in the new lossy environment. This thermal breakdown will prevent the cavity from reaching

higher fields and is therefore undesirable. Second, when the surface magnetic field reaches a critical value, superconductivity ceases. This is a fundamental feature of superconductivity and cannot be improved upon with processing techniques. The theoretical critical field therefore represents a hard limit which can only be raised by using different materials. A low value of $\frac{B_{\mathrm{p}}}{E_{\mathrm{acc}}}$ is therefore desirable for achieving the maximum possible gradient before the transition to the normal state.

### 2.4.6 Cell-to-cell Coupling

When identical elliptical cells are welded together at the iris, the TM010 mode of one cell couples to the TM010 mode of the neighboring cells via the electric field. The cell-to-cell coupling ($k_{\mathrm{cc}}$) causes the frequencies to shift by typically a few percent, forming a narrow passband with as many resonances as there are cells in the cavity. Since the width of the passband is determined by the value of $k_{\mathrm{cc}}$, increasing the number of cells will increase the density of the modes as more modes occur within the same frequency band. The cell-to-cell coupling is calculated from $\nu_\pi$ and $\nu_0$, the frequencies of the $\pi$-mode and 0-mode,

$$k_{cc} = 2\left(\frac{\nu_\pi - \nu_0}{\nu_\pi + \nu_0}\right). \tag{2.102}$$

It is preferable to weld many elliptical cells to form the longest possible multicell cavity. The motivation for doing so is simply to reduce costs. Reducing the total number of cavities reduces the number of separate cryomodules, input power couplers and higher-order mode couplers in addition to reducing the overall length of a linear accelerator.

The number of cells chosen for a given cavity design is generally a compromise between competing design goals. The fields in the end cells are reduced by a factor of $\sin\left(\frac{\pi}{2N}\right)$ for the $\frac{\pi}{N}$-mode, where $N$ is the number of cells. As $N$ increases, the $\frac{\pi}{N}$-modes of the HOM passbands couple out less effectively because of the weaker

fields in the end cells. This reduces the damping of the HOMs and can lead to beam instabilities or excessive heat loads. A larger cavity must supply more beam power; the maximum power carrying capability of input couplers can limit the number of cells. It is impossible to fabricate perfectly identical cells, and the small variations in shape from cell to cell will cause the $\pi$-mode field pattern to be distorted. A multicell cavity must be adjusted cell-by-cell to tune the accelerating mode and to produce a flat $\pi$-mode. The adjustments are done iteratively until the magnitude of the accelerating field in each cell is approximately equal; typically variations less than 3% are sufficient. The distortions are proportional to the square of the number of cells in the cavity but inversely proportional to $k_{\mathrm{cc}}$, therefore large values of $k_{\mathrm{cc}}$ are desirable. The iris radius is the primary parameter which determines the value of $k_{cc}$.

### 2.4.7 Longitudinal Loss Factor

When a charge passes through a cavity, it will excite any cavity mode which has an electric field component in the same direction as the velocity of the charge. By superposition, it is seen that the wake left by a particle is proportional to the charge of the particle. For very high average current beams, the power dissipated by the HOMs can be a large fraction of the total heat load. Monopole HOMs are of concern in this respect since the electric fields on axis will overlap significantly with the ideal particle trajectory. Equation (2.22) may be used to calculate how much a given beam current will excite a particular mode. The solution for the case of a single point charge passing through the cavity is found first. This impulse response may then be convoluted with the beam current to find the wake of a stream of charge bunches.

According to Equations (2.13) and (2.17), the electric field may be written as a sum over the electric fields of the cavity modes. We begin by finding the integrated

voltage gain,

$$\int \mathbf{E}\cdot \mathrm{ds} = \sum_a e_{\mathbf{a}} \sqrt{\frac{\epsilon}{2U_{\mathbf{a}}}} \int \widetilde{\mathbf{E}}_{\mathbf{a}}\cdot \mathrm{ds} = \sum_a e_{\mathbf{a}} \left( \sqrt{\frac{\epsilon}{2U_{\mathbf{a}}}} \int \widetilde{E}_{\mathbf{az}} \mathrm{d}z \right), \tag{2.103}$$

as a function of time when a uniform line current exists in the cavity. The line current lies on the $z$ axis which is also chosen to be the central axis of the cavity. The time dependence is contained completely in the expansion coefficients $e_{\mathbf{a}}$. Multiplying Equation (2.22) by the combination of constants appearing above and setting the surface integrals equal to zero gives

$$\begin{aligned} &\frac{d^2}{dt^2}\left[ e_{\mathbf{a}} \left( \sqrt{\frac{\epsilon}{2U_{\mathbf{a}}}} \int \widetilde{E}_{\mathbf{az}} \mathrm{d}z \right) \right] + \omega_a^2 \left[ e_{\mathbf{a}} \left( \sqrt{\frac{\epsilon}{2U_{\mathbf{a}}}} \int \widetilde{E}_{\mathbf{az}} \mathrm{d}z \right) \right] \\ = \; & -\frac{1}{\epsilon} \left( \sqrt{\frac{\epsilon}{2U_{\mathbf{a}}}} \int \widetilde{E}_{\mathbf{az}} \mathrm{d}z \right) \frac{dj_{\mathbf{a}}}{dt}. \end{aligned} \tag{2.104}$$

The value of $j_{\mathbf{a}}$ may be expressed in terms of the line current $I(t)$:

$$\begin{aligned} j_{\mathbf{a}} &= \int \mathbf{J}\cdot \mathbf{E}_{\mathbf{a}} \mathrm{d}\tau = \sqrt{\frac{\epsilon}{2U_{\mathbf{a}}}} \int \mathbf{J}\cdot \widetilde{\mathbf{E}}_{\mathbf{a}} \mathrm{d}\tau = \sqrt{\frac{\epsilon}{2U_{\mathbf{a}}}} \int I(t)\delta(x)\delta(y)\widetilde{E}_{\mathbf{az}} \mathrm{d}\tau \\ &= \left( \sqrt{\frac{\epsilon}{2U_{\mathbf{a}}}} \int \widetilde{E}_{\mathbf{az}} \mathrm{d}z \right) I(t). \end{aligned} \tag{2.105}$$

Substituting into Equation (2.106), we obtain

$$\begin{aligned} &\frac{d^2}{dt^2}\left[ e_{\mathbf{a}} \left( \sqrt{\frac{\epsilon}{2U_{\mathbf{a}}}} \int \widetilde{E}_{az} \mathrm{d}z \right) \right] + \omega_a^2 \left[ e_{\mathbf{a}} \left( \sqrt{\frac{\epsilon}{2U_{\mathbf{a}}}} \int \widetilde{E}_{\mathbf{az}} \mathrm{d}z \right) \right] \\ = \; & -\frac{1}{2U_{\mathbf{a}}} \left( \int \widetilde{E}_{\mathbf{az}} \mathrm{d}z \right)^2 \frac{dI}{dt}. \end{aligned} \tag{2.106}$$

By setting $I(t) = q\delta(t)$, with $q$ equal to the charge of the point particle, the impulse response of the mode may be found. This expression for the current is acceptable in modelling a point charge in the sense that the instantaneous pulse of current at $t = 0$ carries the total charge $q$ through the cavity. However, the integrated voltage gain $\int E_{\mathbf{az}} \mathrm{d}z$ from the $a^{\mathrm{th}}$ mode for a spatially uniform line current is greater than

the voltage gain a point particle would experience because of transit time effects. By modifying Equation (2.107) with the substitution $\int E_{\mathrm{az}} \mathrm{d}z \rightarrow T_a \int |E_{\mathrm{az}}| dz$, the impulse response due to a point charge may be found. In the case of the voltage $V$ acting on a point charge, Equation (2.103) becomes

$$V = \sum_a e_{\mathrm{a}} \sqrt{\frac{\epsilon}{2U_{\mathrm{a}}}} T_a \int E_{az} dz = \sum_a e_{\mathrm{a}} \sqrt{\frac{\epsilon}{2U_{\mathrm{a}}}} V_a = \sum_a v_a, \tag{2.107}$$

with the following definitions,

$$V_a = T_a \int E_{az} dz. \tag{2.108a}$$

$$v_a = e_{\mathrm{a}} \sqrt{\frac{\epsilon}{2U_{\mathrm{a}}}} V_a. \tag{2.108b}$$

Substituting Equations (2.108) into Equation (2.107) gives a differential equation for the voltage of the $a^{\mathrm{th}}$ mode,

$$\frac{d^2 v_a}{dt^2} + \omega_a^2 v_a = -\frac{V_a^2}{2U_{\mathrm{a}}} \frac{dI}{dt}. \tag{2.109}$$

Using Equation (2.101), the above equation takes the form

$$\frac{d^2 v_a}{dt^2} + \omega_a^2 v_a = -\frac{\omega_a}{2} \left(\frac{R}{Q}\right)_a \frac{dI}{dt}. \tag{2.110}$$

The impulse response due to a point charge $q$ is then zero for $t < 0$ and

$$V(t) = \sum_a v_a(t) = \sum_a -\frac{q\omega_a}{2} \left(\frac{R}{Q}\right)_a \cos(\omega_a t) \text{ for } t \geq 0. \tag{2.111}$$

According to the fundamental theorem of beam loading, the energy a charge deposits in a mode is equal to one half of the product of its charge and the voltage it induces.

The total energy a point charge loses to all of the HOMs is then equal to

$$-\Delta E_{point} = -\frac{q}{2}V = \sum_{a}^{\text{all HOMs}} \frac{q^2\omega_a}{4}\left(\frac{R}{Q}\right)_a. \tag{2.112}$$

The longitudinal loss factor $k_{||}$ is defined in terms of $\Delta E$ and $q$ as

$$k_{||} = \frac{-\Delta E}{q^2} \tag{2.113}$$

The loss factor for a point charge may be expressed as a sum over the individual loss factors of the cavity modes,

$$k_{||} = \sum_a k_{||a} = \sum_a \frac{\omega_a}{4}\left(\frac{R}{Q}\right)_a. \tag{2.114}$$

The general expression for a mode loss factor suggests there are two ways to reduce the amount of energy a charge loses. The value of $\frac{R}{Q}$ depends only on the shape of the cavity, so a shape change such as reducing the $\frac{R}{Q}$ by increasing the radius of the beam pipe and iris reduces $k_{||}$. Also, simply scaling the same shape to a larger size would reduce $\omega_a$ and therefore reduce the $k_{||}$ as well. The voltage for a charge bunch can be calculated by convoluting the induced voltage of a point charge with the bunch charge distribution.

# Chapter 3

# Six-Cell Elliptical Cavity

Historically, hard x-rays for scientific studies have been produced via synchrotron radiation by electron storage ring sources. Since the brilliance and quality of the x-rays produced is tied to the electrons which produce them, the accelerator physics challenges for storage rings are related to producing large electron currents with low transverse and longitudinal emittances. Because electrons in a storage ring undergo thousands of revolutions, the final emittance is the cumulative result of many perturbations: magnetic forces in the ring lattice, emission of synchrotron radiation, electron-electron interactions, and periodic acceleration through RF cavities [15]. In storage rings, the lattice effectively determines the beam emittance.

The beam emittance from a laser driven photocathode source can be lower than the equilibrium emittance of a storage ring, but to preserve the low emittance, the beam must not be recirculated. For a 500 mA beam at 1 GeV, this would result in an unacceptable 500 MW of beam power being dumped. By recirculating the beam once and recovering the energy in the cavities of the main linac, high-current, high emittance beams with a low emittance may be produced. Research and development for ERL based light sources is underway at Cornell and 4GLS at Daresbury, U.K. X-ray production is not the only application which can benefit from high electron beam currents with low emittance. The electron beam may also be used for electron

cooling of hadron beams, which lowers the emittance of the hadron beam, and for collision experiments involving polarized electrons and hadrons [16]. Research is underway at Brookhaven National Laboratory on a superconducting electron cooler and collision experiments are envisioned as possible upgrades to existing facilities, ELIC for CEBAF at Thomas Jefferson National Laboratory and eRHIC at Brookhaven National Laboratory.

The general scheme is outlined in Figure 3.1. A photocathode produces the low emittance beam. The electrons pass through a series of two-cell injector cavities. The limitation to low cell numbers is due primarily to limitations on the maximum power capabilities of RF input couplers: *e.g.* a 500 mA beam gaining 1 MeV would require 500 kW of RF power. The electrons would attain high energy by passing through a series of six-cell cavities and then be used for the intended application: x-ray production, electron cooling, or collision experiments. The choice of six cells per cavity is determined by higher order mode damping requirements. The electrons are then recirculated back to the main linac consisting of six-cell cavities where they are decelerated, giving most of their energy back to the main linac cavities. The low energy electrons are then sent to a beam dump. The power delivered to the beam by the injection cavities is then roughly equal to the power used for the application and the power dissipated at the beam dump. The remaining beam energy is stored in the main linac. Superconducting cavities are a natural choice for large current ERLs because of their large irises and superior performance at large duty cycles. The lower dissipated power of superconducting cavities is also desirable for the main linac of the ERL, shown in the block diagram of Figure 3.1.

The two main challenges to achieving average beam currents on the order of 100 mA are in avoiding excessive amounts of beam-induced HOM power dissipation and avoiding multipass transverse beam breakup. A 6-cell cavity was designed which addresses both of these concerns and is suitable for use in the main linac of an ERL.

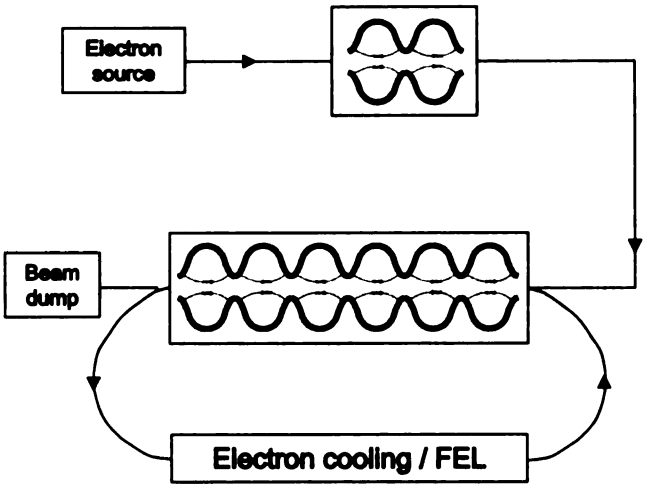


Figure 3.1: The main components of an ERL consist of a source of electrons, a series of small injection cavities operating with full beam loading, a main linac of multi-cell cavities operating with little or no beam loading, the insertion device for the application, and a beam dump.

## 3.1 The Approach to High Beam Currents

One approach to reducing HOM power and avoiding beam breakup is to fill every available RF bucket with a beam bunch, *i.e.* set the bunch frequency equal to the RF frequency $f_{\mathrm{rf}}$ of the accelerating mode. By increasing the bunch frequency, a given average current corresponds to a smaller amount of charge per bunch. The beam-induced HOM power, from Equation (2.113) is

$$P = qk_{||}I_{\mathrm{avg}}, \tag{3.1}$$

with $I_{\mathrm{avg}} = qf_{\mathrm{rf}}$. By reducing the bunch charge, a given beam current is achieved with lower HOM power dissipation. A simplified way to see physically why this occurs is to imagine a single charge $q$ having passed through the cavity and inducing a voltage $2V$ corresponding to an effective voltage of $V$ (from the fundamental theorem of beam loading) and an energy loss of $qV$. The same amount of charge is divided into two pieces and transferred separately through the cavity. The smaller bunch charge $\frac{q}{2}$

induces a smaller effective voltage $\frac{V}{2}$ resulting in an energy loss of $\frac{qV}{4}$ per bunch. The total loss of both bunches $\frac{qV}{2}$ is one half of the single bunch energy loss. Reducing the bunch charge ensures that, at any given moment, less charge is flowing through the cavity, and therefore perturbing the cavity less, reducing the amplitude of the wake field.

Increasing the bunch frequency can also simplify HOM damping and increase the threshold current for beam break up (BBU). The top of the cartoon in Figure 3.2 depicts some common features of the magnitude of the impedance for a multicell cavity as a function of frequency. The diagram shows a resonance for each mode of the cavity which has an electric field in the direction of the charge motion. The lowest frequency modes are in the TM010 passband with the frequency of the $\pi$-mode denoted as $f_{\mathrm{rf}}$. The next two passbands contain higher order modes. All three passbands contain very high-$Q$ modes with narrow resonances. The frequencies of these modes are below the cutoff frequency for the lowest waveguide mode. Since the cavity cannot couple to a propagating waveguide mode at these frequencies, these modes lose energy through dissipation in the superconducting walls only. The cavity modes above the cutoff frequency are able to couple out through the beam pipe and can be readily damped by either a ferrite load or a HOM coupler and therefore have much broader resonances. The beam current is assumed to consist of a steady state series of bunches with a Gaussian charge distribution. The Fourier transform of a single Gaussian bunch is itself a Gaussian, and forms an envelope for the Fourier components of the beam. From Equation (2.110), it is seen that the beam acts to excite the HOMs. The spectra of the cavity and the beam are overlapped at the bottom of Figure 3.2, showing that the beam can drive the high-$Q$ modes below cutoff.

The cartoon in Figure 3.3 illustrates some of the benefits of a high bunch frequency. The bunch charge has been reduced, resulting in less HOM power at the same beam current, and the spacing between the harmonics of the beam is larger. The shape of

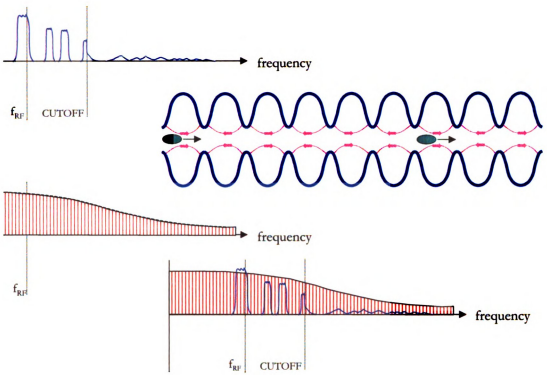


Figure 3.2: Top: coupling impedance of a multi-cell cavity as a function of frequency. Middle: Fourier spectrum of a beam with low bunch frequency. Bottom: superposition of the coupling impedance and beam spectrum. At low bunch frequencies, the bunch charge is high and the beam harmonics are close together, so all HOMs must be heavily damped to avoid driving them to high levels.

the cavity may be designed to take full advantage of decrease in the density of the beam harmonics to simplify HOM damping. By making the radius of the beam tube large enough such that the cutoff frequencies of the lowest frequency monopole and dipole waveguide modes is less than $2f_{\mathrm{rf}}$, the beam harmonics will only be driving HOMs in which energy may propagate away through the beam pipe. Both a 2-cell and 6-cell cavity were designed to meet this condition.

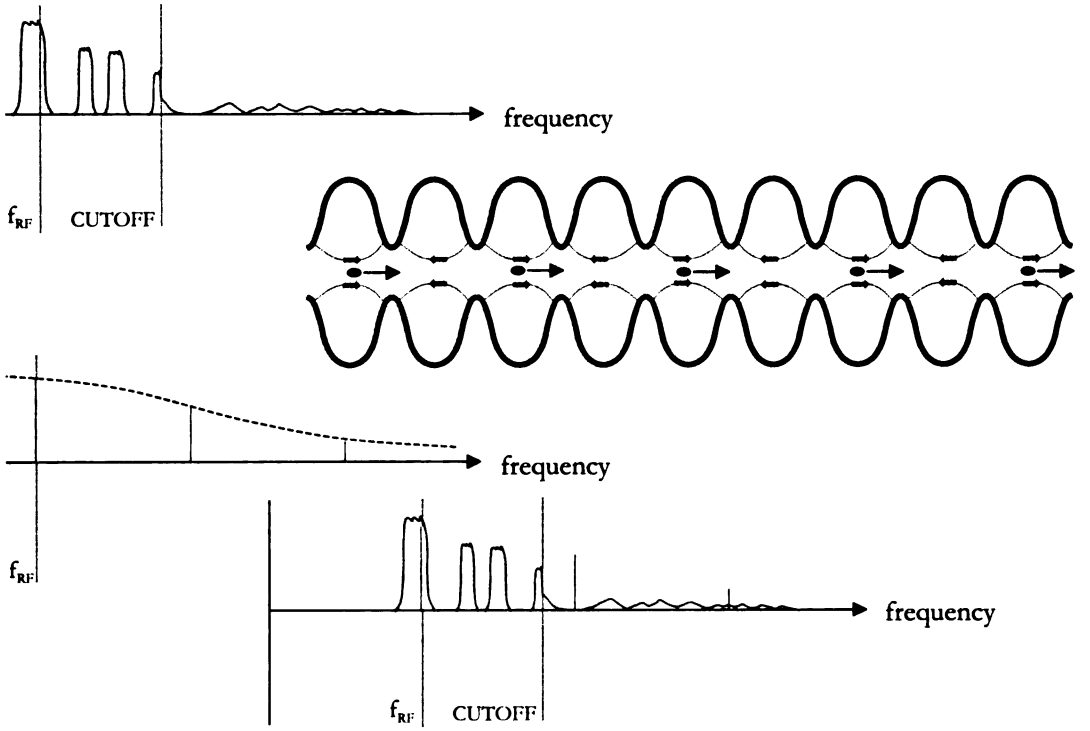


Figure 3.3: Top: coupling impedance of a multi-cell cavity as a function of frequency. Middle: Fourier spectrum of a beam with high bunch frequency. Bottom: superposition of the coupling impedance and beam spectrum. At high bunch frequencies, the bunch charge is low and the spacing between the beam harmonics may be large enough so as only to drive propagating HOMs.

## 3.2 Six-Cell Design

The cavity shape for the main linac must be designed for electrons travelling at speeds $v$ approximately equal to that of light ($\beta = \frac{v}{c} \approx 1$). The length $l$ of each cell is then determined from the condition that it takes half an RF period for an electron to traverse a cell: this ensures that the electrons will only experience electric forces in the direction of motion when the cavity is operated in the $\pi$-mode,

$$l = \frac{v}{2f_{\mathrm{rf}}}. \tag{3.2}$$

The resonant frequency of the TM010 $\pi$-mode was set equal to 2.45 GHz by adjusting the value of the equatorial radius. An advantage of choosing a relatively high accelerating mode frequency of 2.45 GHz is that an inexpensive 200W solid state amplifier could be used for vertical RF testing. Also, a smaller cavity is generally less expensive to fabricate. However, if the cavity shape were used for an ERL, the size could be scaled to a lower frequency. As explained in Section 2.4.6, a large number of cells is desirable but, with many cells, there is an increased risk that some HOMs will not couple strongly enough to the beam pipe. A prudent choice of six cells was used to ensure adequate HOM coupling. The angle that the straight section makes with the vertical is set equal to 6°. Smaller angles benefit the electromagnetic performance of the accelerating mode, but a lower limit exists because of the need to have fluids drain out of the cavity during processing. Inadequate draining could result in microparticles remaining in the cavity after high pressure rinsing and ultimately lead to field emission. The mode of propagation with the lowest cutoff frequency for a circular waveguide is TE11. It was shown in Section A.2.2 that the cutoff wavenumber for the TE11 mode is

$$k_c = \frac{1.841}{R_{\text{iris}}}, \tag{3.3}$$

which corresponds to a cutoff frequency of

$$f_c = \frac{1.841c}{2\pi R_{\text{iris}}}. \tag{3.4}$$

The speed of light is $c$ and $R_{\text{iris}}$ is the radius of the cavity iris which is set equal to the radius of the beam tube. The beam tube radius must be large enough so that $f_c < 2f_{\text{rf}}$ to ensure that only propagating dipole HOMs can be excited by the beam. Monopole HOMs will not couple to a dipole waveguide mode. The monopole waveguide mode with the lowest cutoff frequency is TM01. From Section A.2.4, it is

seen that the cutoff wavenumber for this mode is

$$k_c = \frac{2.405}{R_{\text{iris}}}, \tag{3.5}$$

which corresponds to a cutoff frequency of

$$f_c = \frac{2.405c}{2\pi R_{\text{iris}}}. \tag{3.6}$$

To ensure that $f_c < 2f_{\text{rf}}$, the value of the iris radius for the 6-cell design must satisfy

$$R_{\text{iris}} > \frac{2.405c}{4\pi f_{\text{rf}}} = 2.34 \text{ cm}. \tag{3.7}$$

The risk of field emission is reduced in cavities with a low ratio of peak electric field $E_p$ to accelerating field $E_a$, while the risk of thermal breakdown is reduced in cavities with a low value of peak magnetic field $B_p$ to accelerating field $E_a$. The aspect ratio of the ellipses primarily determine the values of these peak-field ratios, and it is generally found that choosing a shape which reduces one peak-field ratio invariably increases the other. The ratio of $E_p$ to $B_p$ serves as a useful measure of the compromise made between reducing the chances of field emission versus thermal breakdown. The TeSLA Test Facility (TTF) [17] cavity shape has been very successful at achieving high fields reliably, so the TTF ratio of $\frac{E_p}{B_p}$ was adopted for the 6-cell cavity. Since the 6-cell cavity will have a larger iris than the TTF cavity, the values of $\frac{E_p}{E_{acc}}$ and $\frac{B_p}{E_{acc}}$ for the 6-cell cavity will both be higher than those of the TTF cavity. To reduce the possibility of field emission or thermal breakdown, the increase in the peak-field ratios of the 6-cell cavity did not exceed the TTF values by more than 10%.

SUPERFISH [18] was used for the cavity design calculations. Finding a cavity shape to meet these criteria required hundreds of simulations, with relatively minor adjustments in the cavity shape between simulations. In addition, the different

elements of the cavity shape must be joined together smoothly, *i.e.* the elements must join at locations tangent to one another. A program was therefore developed in Microsoft Excel to generate the cavity shape for a given set of parameters. The geometrical parameters for a half-cell are shown in Figure 1.2. The user supplies the values of $\frac{B}{A}$, $\frac{b}{a}$, the vertical height $h = D - B$ of the center of the equatorial ellipse, the vertical height $z = b + R_{\text{iris}}$ of the center of the iris ellipse, $L$, $R_{\text{iris}}$, $d$, $\alpha$, and $f_{\text{rf}}$: the origin of the coordinate system is located at the lower left of the diagram in Figure 1.2. The values of the equatorial radius $D$, the coordinates of the equatorial-ellipse-to-straight-section union $(x_1,y_1)$, the coordinates of the iris-ellipse-to-straight-section union $(x_2,y_2)$, the major and minor semi-axes of the equatorial ellipse ($A$, $B$), and the major and minor semi-axes of the iris ellipse ($a$, $b$) are then computed with the following equations:

$$m = \frac{-1}{\tan(\alpha)} \tag{3.8}$$

$$x_1 = \frac{\left[L - d + \frac{(h - R_{\text{iris}})}{m}\right]}{1 + \left[\frac{\left(\frac{B}{A}\right)}{m}\right]^2} \tag{3.9}$$

$$y_1 = m(x_1 - L + d) + R_{\text{iris}} \tag{3.10}$$

$$B = \sqrt{\left(\frac{B}{A}\right)^2 x_1^2 + (y_1 - h)^2} \tag{3.11}$$

$$A = \frac{B}{\left(\frac{B}{A}\right)} \tag{3.12}$$

$$x_2 = \frac{\frac{L}{m}\frac{b}{a}^2 + m(L - d) + z - R_{\text{iris}}}{m + \frac{\left(\frac{b}{a}\right)^2}{m}} \tag{3.13}$$

$$y_2 = m(x_2 - L + d) + R_{\text{iris}} \tag{3.14}$$

$$b = z - R_{\text{iris}} \tag{3.15}$$

$$a = \frac{b}{\left(\frac{b}{a}\right)} \tag{3.16}$$

Table 3.1: Final geometrical parameters for the mid-cell of the 6-cell cavity (left) and corresponding figures of merit for the $\pi$-mode of an infinitely long periodic structure (right).

| | |
|---|---|
| $A$ | 2.216 cm |
| $B$ | 1.884 cm |
| $h$ | 3.693 cm |
| $a$ | 0.813 cm |
| $b$ | 1.165 cm |
| $z$ | 3.555 cm |
| $L$ | 3.062 cm |
| $d$ | 0.7 cm |
| $R_{\text{iris}}$ | 2.39 cm |
| $R_{\text{equator}}$ | 5.58 cm |
| $\alpha$ | 6.0° |

| | |
|---|---|
| $\frac{R}{Q}$ | 89.6 Ω |
| $\frac{E_{\text{p}}}{E_{\text{acc}}}$ | 2.15 |
| $\frac{B_{\text{p}}}{E_{\text{acc}}}$ | 4.63 $\frac{\text{mT}}{\frac{\text{MV}}{\text{m}}}$ |
| $G$ | 275 Ω |
| $k_{\text{cc}}$ | 4.18% |

A screen shot of the interface is shown in Figure 3.4.

A sketch of the half-cell is produced by the program and a SUPERFISH input file is created for that cell shape. Short-circuit boundary conditions are placed on the left plane (the plane of the equator), while open-circuit boundary conditions are placed on the right plane (the plane of the iris). The resulting field pattern from SUPERFISH corresponds to that of the $\pi$-mode for an infinitely long periodic structure. The figures of merit are extracted from the SUPERFISH output file and displayed by the interface. A second input file is created in which the boundary condition on the right plane is changed to a short circuit. The resulting field pattern corresponds to the 0-mode of an infinitely long periodic structure. The frequencies of the two simulations are then used to compute $k_{cc}$ according to Equation (2.102). These final values are shown in Table 3.1.

The figures of merit in Table 3.1 are valid for an infinitely long periodic structure, however the same mid-cell field pattern may be reproduced in a real cavity with beam tubes attached by varying the shape of the end-cells. Leaving the end-cell geometry equal to the mid-cell geometry most likely will cause the peak surface fields in the cavity to be located in the end-cells. Additionally, it is likely that the axial electric

Table 3.2: Final geometrical parameters for the end-cells of the 6-cell cavity (left) and figures of merit for the $\pi$-mode of the full 6-cell cavity (right).

| | |
|---|---|
| $A$ | 2.312 cm |
| $B$ | 2.820 cm |
| $h$ | 2.757 cm |
| $a$ | 0.813 cm |
| $b$ | 1.165 cm |
| $z$ | 3.555 cm |
| $l$ | 3.062 cm |
| $d$ | 0.63 cm |
| $R_{\text{iris}}$ | 2.39 cm |
| $R_{\text{equator}}$ | 5.58 cm |
| $\alpha$ | 9.93° |

| | |
|---|---|
| $\frac{R}{Q}$ | 535.2 Ω |
| $\frac{E_{\text{p}}}{E_{\text{acc}}}$ | 2.19 |
| $\frac{B_{\text{p}}}{E_{\text{acc}}}$ | 4.68 $\frac{\text{mT}}{\frac{\text{MV}}{\text{m}}}$ |
| $G$ | 275 Ω |
| $k_{\text{cc}}$ | 4.18% |
| $T$ | 0.77 |

field will be higher in the end-cells. The values of $E_{\text{p}}$ and $B_{\text{p}}$ determine the maximum achievable gradient for a cavity, so untuned end-cells ultimately result in lowering the maximum gradient. The goal of the end-cell tuning is therefore to reduce the peak field values to a level at or below the peak fields in the mid-cells while simultaneously providing "flat" axial electric fields. Each cell in a cavity with completely "flat" fields would have the same magnitude for the peak axial electric field.

Table 3.2 shows the geometrical parameters for the end-cell shape used for the 6-cell cavity. The figures of merit for the full 6-cell cavity are also shown. Figure 3.5 shows a picture of the cavity shape with the $\pi$-mode electric field lines predicted by SUPERFISH. The peak electric and magnetic fields are seen in Figure 3.6 to occur in the midcells and the axial field magnitudes shown in Figure 3.7 are "flat" to within 3%. The flatness was measured by forming the ratio,

$$\frac{2(|E_{\text{zo}}^{\text{max}}| - |E_{\text{zo}}^{\text{min}}|)}{|E_{\text{zo}}^{\text{max}}| + |E_{\text{zo}}^{\text{min}}|}, \tag{3.17}$$

where $E_{\text{zo}}$ is the peak axial electric field within a cell. The transit time curve for the 6-cell cavity is shown in the next chapter (Figure 4.4).

## 3.3 Higher Order Modes of Interest

The six-cell cavity is designed such that, when operating CW in the energy recovery mode with every RF bucket filled, the beam will only drive HOMs which have frequencies above the cutoff frequency of the beam pipe. It is desirable for the modes which can be driven by the beam to have strong coupling to the beam pipe in order to ensure that the energy of these modes may couple out. To help address the question of coupling strength, a HOM analysis following the technique for the BNL "Ampere Class" cavity was done [19]. The calculations were done using Analyst [20]. For the six-cell HOMs, simulations were carried out by Analyst: one set of simulations used electric boundary conditions for the end of the beam pipe while another set used magnetic boundary conditions. Electric boundary conditions mean that the tangential electric field and the normal magnetic are both zero on the boundary. Magnetic boundary conditions mean that the tangential magnetic field and normal electric field are both zero on the boundary. A strongly coupled HOM will have high field throughout the beam pipe. In this case, the different boundary conditions will result in different frequencies and this frequency difference may be used as a rough meaure of the HOM coupling strength. The frequency from the electric boundary condition simulation $f_e$ and the frequency from the magnetic boundary condition $f_h$ are combined in a single expression to measure the coupling strength:

$$\chi = \log\left[\frac{f_e + f_h}{2|f_e - f_h|}\right]. \tag{3.18}$$

Low $\chi$ values indicate high coupling.

The $\frac{R}{Q}$ was calculated by integrating the voltage gain over a path along the central axis of the cavity and between the cavity end cell irises. Simulation results for 700 monopole HOMs below approximately 20 GHz are shown in Figures 3.8 and 3.9. In energy recovery mode with every bucket filled, there are two charge bunches for every RF period, hence the beam spectrum consists of multiples of 4900 MHz. It is worth

noting that the simulations for the HOM spectrum of the six-cell cavity were extended to a higher frequency (20000 MHz) than in the BNL 5-cell study (1800 MHz with an accelerating mode frequency of 703 MHz). If the Ampere-class cavity is rescaled for an accelerating mode frequency of 2450 MHz, then the original 1800 MHz range HOM study is rescaled to a range of 6273 MHz. The HOM analysis of the six-cell cavity below 6273 MHz may then be compared to the Ampere-class results.

The six-cell cavity does have some weakly coupled modes below 4900 MHz, but the $\chi$ values near 4900 MHz are below 3, which is the maximum $\chi$ value for the Ampere-class cavity. It is therefore reasonable to expect the dangerous HOMs of the six-cell cavity to propagate as effectively as those of the Ampere-class.

Simulation results for 700 dipole HOMs below approximately 20000 MHz are shown in Figures 3.10 and 3.11. The $\frac{R}{Q}$ was calculated using an integration path between the cavity end cell irises and offset from the central axis by 5 mm. Comparing these results with those of the Ampere-class, where the same type of calculations resulted in $\chi$ between 3 and 4 for the dipole modes, similar performance is again expected for the six-cell cavity. For the six-cell cavity, $\chi$ is less than 4 for the dipole modes at frequencies which are multiples of 4900 MHz. It is seen in Figure 3.11 that each dipole $\frac{R}{Q}$ is less than 30 $\frac{\Omega}{\text{cm}^2}$, whereas the Ampere-class contains dipole modes with $\frac{R}{Q}$s as high as 55 $\frac{\Omega}{\text{cm}^2}$. According to Equation (1.5), the threshold current for beam breakup is inversely proportional to the HOM shunt impedance. It is therefore not unreasonable to expect slightly higher threshold currents for the six-cell cavity.

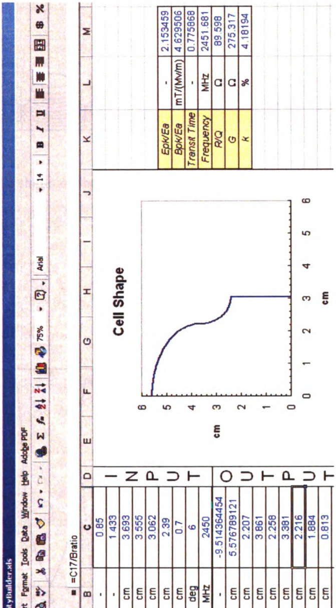

| | A | B | C | D |
|---|---|---|---|---|
| 1 | B/A | - | 0.85 | I |
| 2 | b/a | - | 1.433 | N |
| 3 | h | cm | 3.693 | P |
| 4 | z | cm | 3.555 | U |
| 5 | L | cm | 3.062 | T |
| 6 | $r_{iris}$ | cm | 2.39 | |
| 7 | d | cm | 0.7 | |
| 8 | slope | deg | 6 | |
| 9 | Target Freq. | MHz | 2450 | |
| 10 | m | - | -9.514364454 | O |
| 11 | $R_{equator}$ | cm | 5.576789121 | U |
| 12 | x1 | cm | 2.207 | T |
| 13 | y1 | cm | 3.861 | P |
| 14 | x2 | cm | 2.258 | U |
| 15 | y2 | cm | 3.381 | T |
| 16 | A | cm | 2.216 | |
| 17 | B | cm | 1.884 | |
| 18 | a | cm | 0.813 | |

| K | L | M |
|---|---|---|
| Epk/Ea | - | 2.153459 |
| Bpk/Ea | mT/(Mv/m) | 4.629506 |
| Transit Time | - | 0.775868 |
| Frequency | MHz | 2451.681 |
| R/Q | Ω | 89.598 |
| G | Ω | 275.317 |
| k | % | 4.18194 |

Figure 3.4: Five free parameters $\frac{B}{A}$, $\frac{b}{a}$, $h$, $z$, and $d$ uniquely determine the cell shape displayed at center and the corresponding figures of merit displayed on the right.

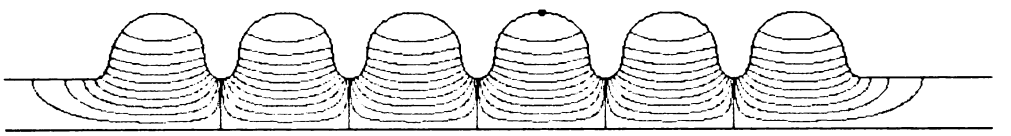

Figure 3.5: The shape of the 6-cell cavity with electric field lines calculated by SUPERFISH.

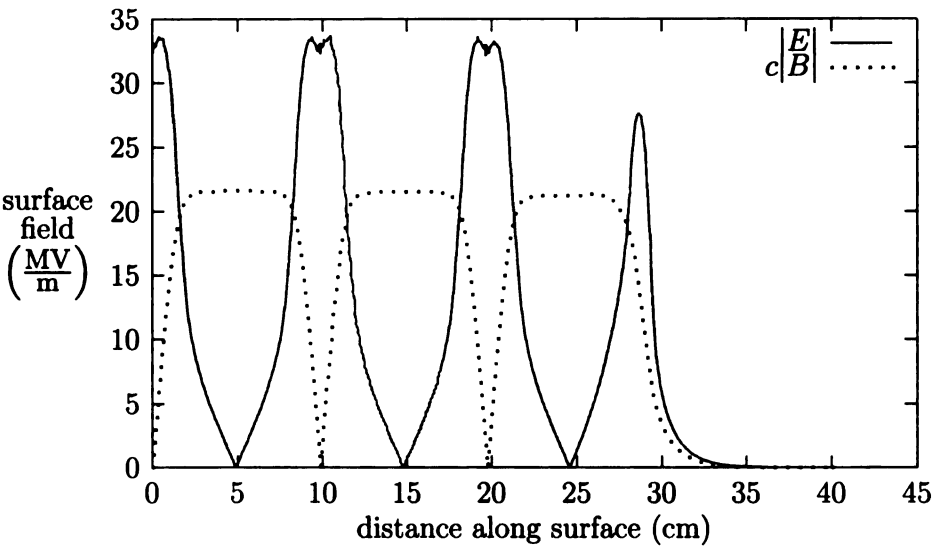


Figure 3.6: Magnitudes of the electric and magnetic fields for the 6-cell cavity as a function of distance along the surface. The origin is located at the middle of the cavity on the iris. The path moves along the surface and toward the beam pipe. The fields are normalized to an accelerating gradient of $15.3\,\frac{\text{MV}}{\text{m}}$.

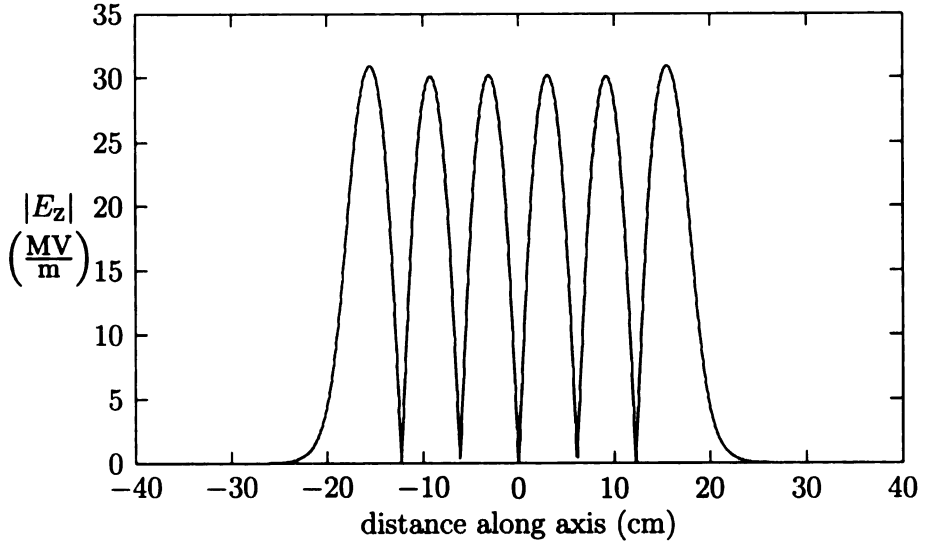


Figure 3.7: Variation of the magnitude of the axial field for the $\pi$-mode for the 6-cell cavity as a function of the axial distance. The fields are normalized to an accelerating gradient of 15.3 $\frac{MV}{m}$. The origin is at the middle iris of the cavity.

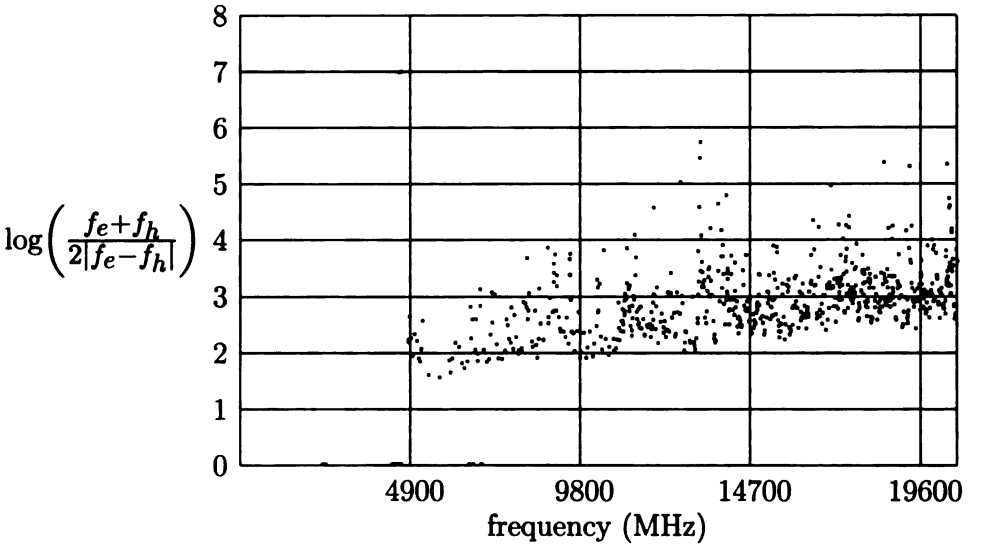


Figure 3.8: Two different simulations were done for each monopole mode: one with electric boundary conditions on the beam pipe and the other with magnetic boundary conditions on the beam pipe. Large differences in the frequencies for these two simulations indicates large field in the beam pipe and corresponding large coupling of the HOM. It should be noted that the zero values seen correspond to numerically divergent results where the frequencies of the two simulations are equal.

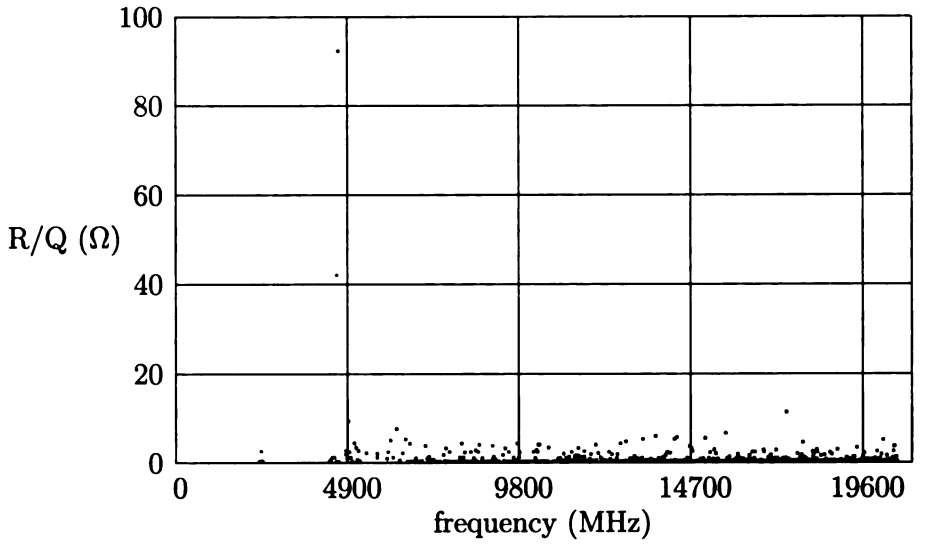


Figure 3.9: The $R/Q$s for the monopole modes as a function of frequency.

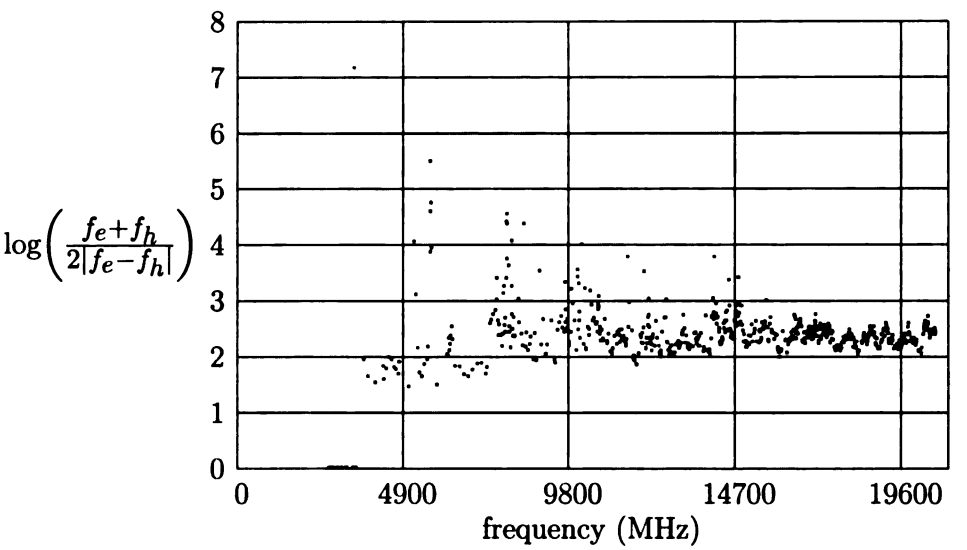


Figure 3.10: Two different simulations were done for each dipole mode: one with electric boundary conditions on the beam pipe and the other with magnetic boundary conditions on the beam pipe. Large differences in the frequencies for these two simulations indicates large field in the beam pipe and corresponding large coupling of the HOM. It should be noted that the zero values seen correspond to numerically divergent results where the frequencies of the two simulations are equal.

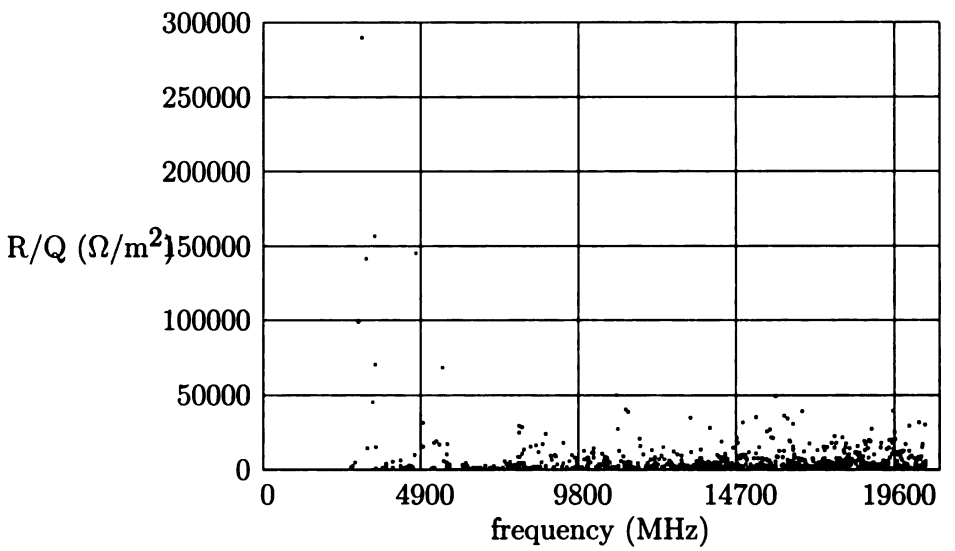


Figure 3.11: The $R/Q$s for the dipole modes as a function of frequency.

# Chapter 4

# Two-Cell Elliptical Cavity

## 4.1 Two-Cell Cavity Design

### 4.1.1 SUPERFISH Simulations

The 2-cell cavity will share the same design criteria as the 6-cell cavity:

- 2.45 GHz $\pi$-mode frequency
- TM01 cutoff $< 1.95 f_{\mathrm{rf}}$
- TE11 cutoff $< 1.5 f_{\mathrm{rf}}$
- 6° wall angle
- $\frac{E_{\mathrm{p}}}{B_{\mathrm{p}}}$ equal to TTF value.

In addition, the 2-cell cavity was designed to accelerate electrons with low initial energy. Electrons from a gun with an energy of approximately 50 keV could be accelerated by two 2-cell cavities to an injection energy between 1 and 2 MeV for injection into the ERL main linac.

A final cell geometry was determined using SUPERFISH simulations and the half-cell parameters are listed in Table 4.1 along with the figures of merit. In the 2-cell

case, a single half-cell geometry was used; the half-cells which are welded to the beam pipe have the same shape as the half-cells welded together at the middle iris. The cavity shape is shown in Figure 4.1. The magnitudes of the electric and magnetic fields on the surface of the right half of the cavity are shown in Figure 4.2. It is seen that the peak electric field occurs on the middle iris.

Table 4.1: Final geometrical parameters for the 2-cell cavity (left) and figures of merit (right) for $\beta = 1$. The value of $k_{cc}$ was calculated using the same cell geometry but assuming an infinitely long periodic structure.

| | |
|---|---|
| $A$ | 1.643 cm |
| $B$ | 1.479 cm |
| $h$ | 4.120 cm |
| $a$ | 0.732 cm |
| $b$ | 1.049 cm |
| $z$ | 3.439 cm |
| $l$ | 2.462 cm |
| $d$ | 0.630 cm |
| $r_{\text{iris}}$ | 2.390 cm |
| $R_{\text{equator}}$ | 5.599 cm |
| $\alpha$ | 6.0° |

| | |
|---|---|
| $\frac{R}{Q}$ | 164.6 Ω |
| $\frac{E_p}{E_{acc}}$ | 2.16 |
| $\frac{B_p}{E_{acc}}$ | 4.59 $\frac{\text{mT}}{\frac{\text{MV}}{\text{m}}}$ |
| $G$ | 228 Ω |
| $k_{cc}$ | 5.62% |

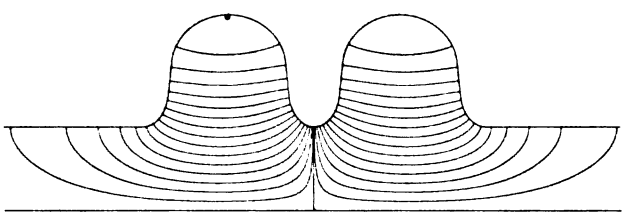

Figure 4.1: The shape of the 2-cell cavity with the electric field lines for the $\pi$-mode.

Figure 4.3 shows a plot of the magnitude of the axial electric field $E_z$ along the axis of the right half of the cavity. The field goes through zero at the middle of the cavity since it is the $\pi$-mode, and trails off exponentially with the evanescent fields in the beam pipe. For an infinitely long structure with the same cell shape, the field would go through zero at every iris. In this case, maximum energy gain would occur for particles with a constant speed of $\beta = \frac{4 f_{rf} L}{c}$, the so called geometric $\beta$.

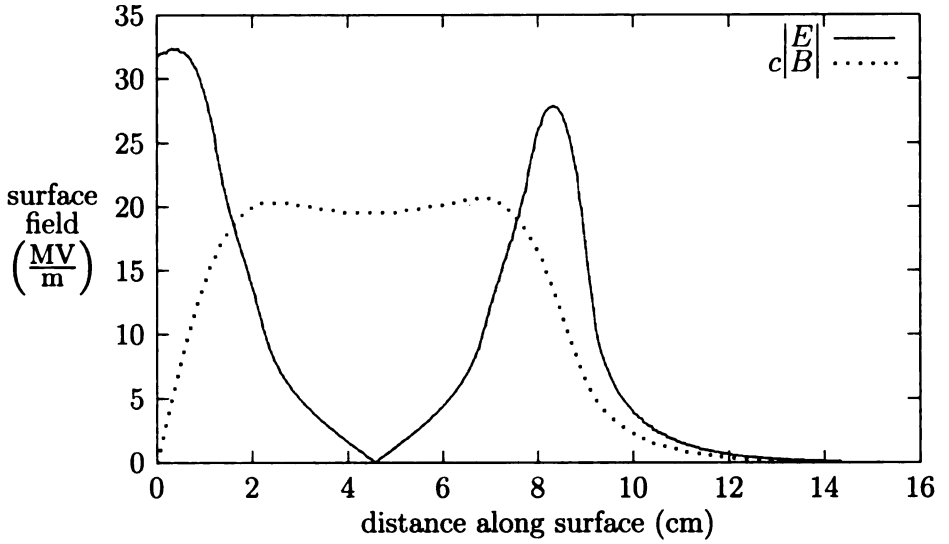


Figure 4.2: Magnitudes of the electric and magnetic fields as a function of the distance along the surface. The origin is located at the middle of the cavity on the iris. The path moves along the surface and toward the beam pipe. The fields are normalized to an accelerating gradient of $10\frac{\text{MV}}{\text{m}}$.

Substituting $f_{\text{rf}} = 2.45\,\text{GHz}$ and $L = 2.462\,\text{cm}$ results in a geometric $\beta$ of 0.805 for the 2-cell cavity. Adding a large-diameter beam pipe cause the field to fringe out into the beam pipe. The cell length $L = 2.462\,\text{cm}$ was chosen so because most of the high field region is then contained within a distance of $\frac{c\pi}{\omega} = 6.12$ cm from the center. This improves the transit time factor for velocity of light particles. For a particle to travel the iris-to-iris distance in exactly half a RF period would require a constant speed of $\beta = \frac{v}{c} = 0.805$. It is the extension of the axial electric field into the beam pipe which causes the energy gain for $\beta = 1$ to be larger than $\beta = 0.805$.

Figure 4.4 shows a plot of the transit time factor as a function of particle $\beta$ for both the 2-cell and 6-cell cavities. The transit time factors were calculated using a constant velocity approximation. By squeezing the 2-cell cavity to a geometric $\beta$ of 0.805, the transit time factor is comparable to the 6-cell cavity at particle speeds equal to the speed of light. Electrons will quickly approach the speed of light and efficient acceleration at these speeds is therefore desirable. Also, if a more elaborate electron source such as a superconducting photocathode is used, then the particles

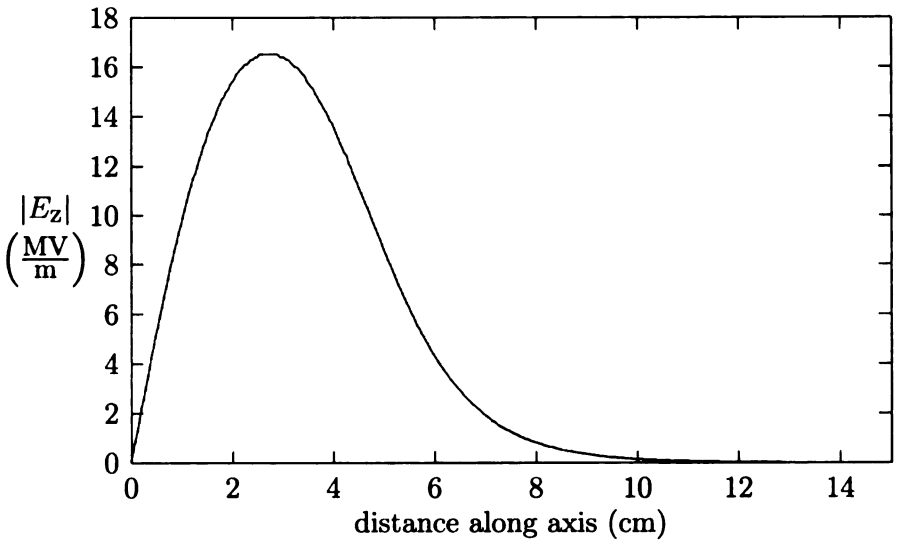


Figure 4.3: Magnitude of the axial electric field along the central axis of the 2-cell cavity, normalized to an accelerating gradient of $10\frac{MV}{m}$.

would enter the injection cavity with speeds comparable to that of light, and efficient acceleration at $\beta = 1$ is again desirable.

Because only two cells are used to form the injection cavity, the transit time values at low particle speeds are much better than for the 6-cell cavity. This allows low energy electrons with speeds of approximately $0.5c$ from a normal conducting gun to be accelerated by the 2-cell cavity. Limiting the injection cavity to two cells is also necessary because of the limitations in the maximum power capabilities of input couplers. The 2-cell cavity would be operated with full beam loading, in contrast to the 6-cell cavity which would operate in energy recovery mode. Providing 500 kV of voltage gain to 100 mA of beam would require 50 kW of input power; this is close to the power handling limits of input couplers. This translates to a design accelerating gradient of approximately 5 $\frac{MV}{m}$. Operation at 2 K with a $Q_0 = 5 \cdot 10^9$ is feasible. Operation at or below 2 K would be necessary if a relatively high frequency such as 2.45 GHz is used, since the BCS resistance increases with frequency.

Table 4.2 compares the figures of merit and aperture dimensions of the 2-cell cavity to those of the Cornell ERL injector cavity [21]. Both cavities are designed for 100

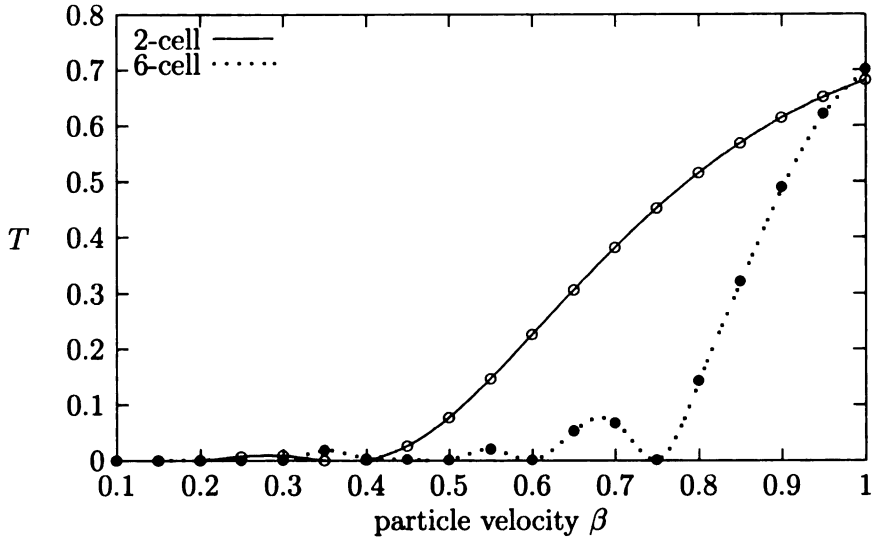


Figure 4.4: Transit time factor $T$ as a function of particle speed calculated with SUPERFISH for the 2-cell and 6-cell cavities. The particle velocity is assumed constant for the evaluation of $T$.

mA of beam current and both consist of 2 cells. The Cornell cavity has a better $\frac{R}{Q}$, $\frac{E_p}{E_{acc}}$, and $\frac{B_p}{E_{acc}}$ due primarily to its smaller iris radius; the 2-cell cavity iris radius is 28% larger when both cavities are scaled to have the same frequency. An advantage of the larger iris radius of the 2-cell cavity is a lower overall loss factor, and it is worth noting that $\frac{E_p}{E_{acc}}$ and $\frac{B_p}{E_{acc}}$ are only 11% and 7% larger respectively.

## 4.2 Higher Order Modes of Interest

The two-cell cavity is designed such that, when operating CW with every RF bucket filled, the beam will only drive HOMs which have frequencies above the cutoff frequency of the beam pipe. It is desirable for the modes which can be driven by the beam to have strong coupling to the beam pipe in order to ensure that the energy of these modes may couple out. The technique for analyzing the 2-cell HOMs is identical to that in Section 3.3 for the six-cell cavity. For the 2-cell cavity, beam loading is present and Fourier components of the beam are present at multiples of 2450 MHz. Simulation results for 425 monopole HOMs below approximately 30 GHz are shown

Table 4.2: Comparison of the 2-cell cavity figures of merit to those of the Cornell ERL injector cavity(also a 2-cell cavity).

| cavity | 2-cell | Cornell Injector |
|---|---|---|
| $\frac{R}{Q}$ | 164.6 Ω | 218 Ω |
| $\frac{E_{\mathrm{p}}}{E_{\mathrm{acc}}}$ | 2.16 | 1.94 |
| $\frac{B_{\mathrm{p}}}{E_{\mathrm{acc}}}$ | 4.59 $\frac{\mathrm{mT}}{\frac{\mathrm{MV}}{\mathrm{m}}}$ | 4.28 $\frac{\mathrm{mT}}{\frac{\mathrm{MV}}{\mathrm{m}}}$ |
| $k_{\mathrm{cc}}$ | 5.62% | 0.7 % |
| frequency | 2450 MHz | 1300 MHz |
| left beam pipe radius | 2.39 cm | 3.9 cm |
| iris radius | 2.39 cm | 3.5 cm |
| right beam pipe radius | 2.39 cm | 5.3 cm |

in Figures 4.5 and 4.6. The $\frac{R}{Q}$ was calculated by integrating the voltage gain over a path along the central axis of the cavity and between the end cell irises. The relatively weak coupling seen in Figure 4.5 for modes near 17,150 MHz, 22,050 MHz, and 26,950 MHz may lead to high resonant HOM fields if adequate damping is not present.

Simulation results for 400 dipole HOMs below approximately 30 GHz are shown in Figures 4.7 and 4.8. The $\frac{R}{Q}$ was calculated using an integration path between the ends of the cavity and offset from the central axis by 5 mm. For the two-cell cavity, $\chi$ is highest between 6 to 7 for the monopole modes and between 4 to 5 for the dipole modes at frequencies which are multiples of 2450 MHz.

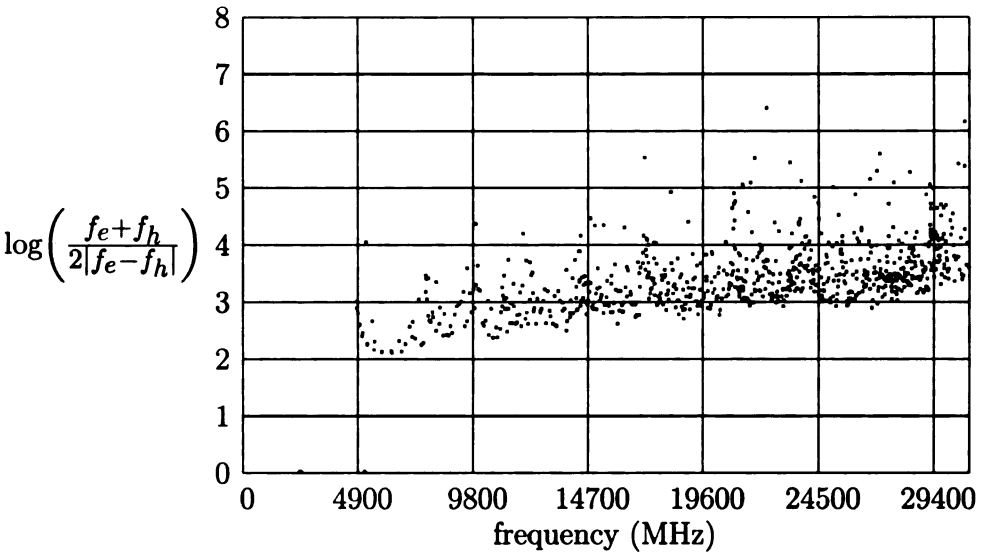


Figure 4.5: Two different simulations were done for each monopole mode: one with electric boundary conditions on the beam pipe and the other with magnetic boundary conditions on the beam pipe. Large differences in the frequencies for these two simulations indicates large field in the beam pipe and corresponding large coupling of the HOM. It should be noted that the zero values seen correspond to numerically divergent results where the frequencies of the two simulations are equal.

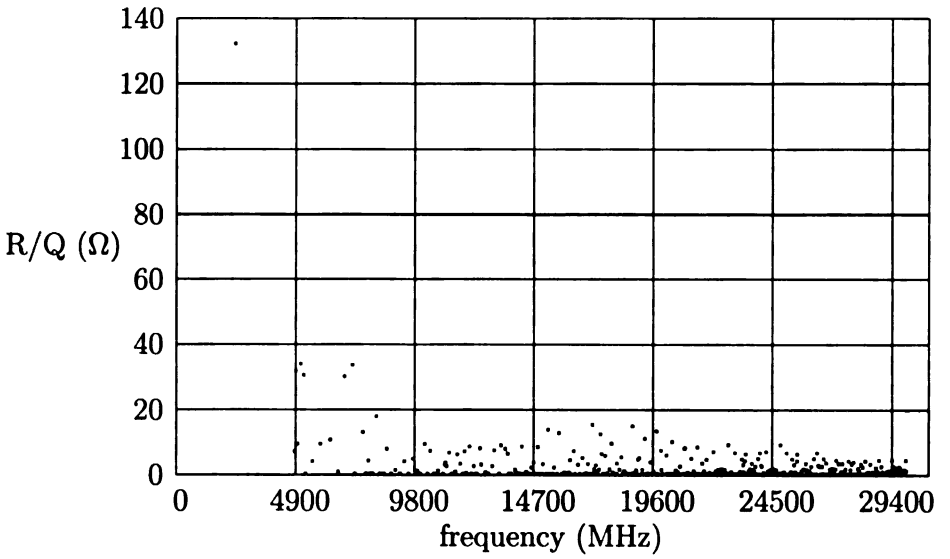


Figure 4.6: The R/Qs for the monopole modes are plotted vs. frequency.

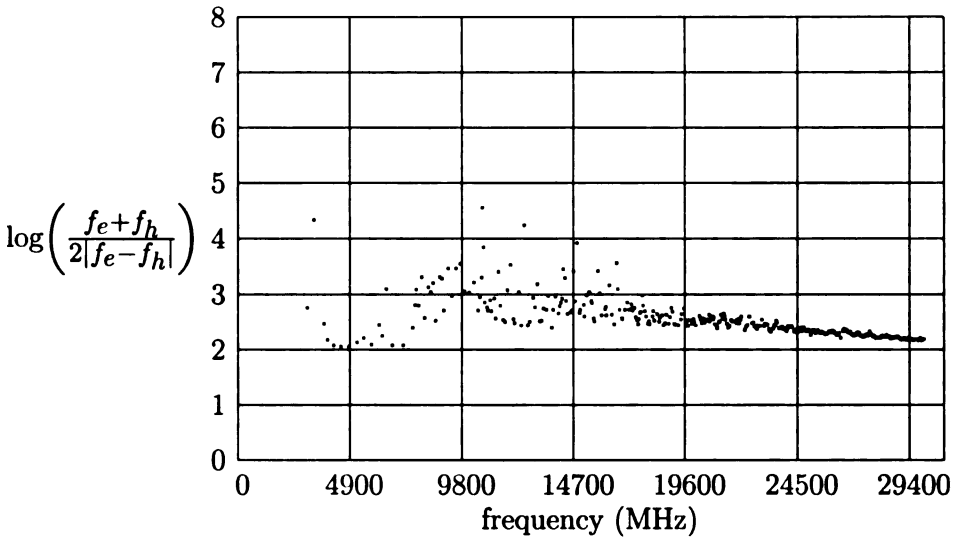


Figure 4.7: Two different simulations were done for each dipole mode: one with electric boundary conditions on the beam pipe and the other with magnetic boundary conditions on the beam pipe. Large differences in the frequencies for these two simulations indicates large field in the beam pipe and corresponding large coupling of the HOM.

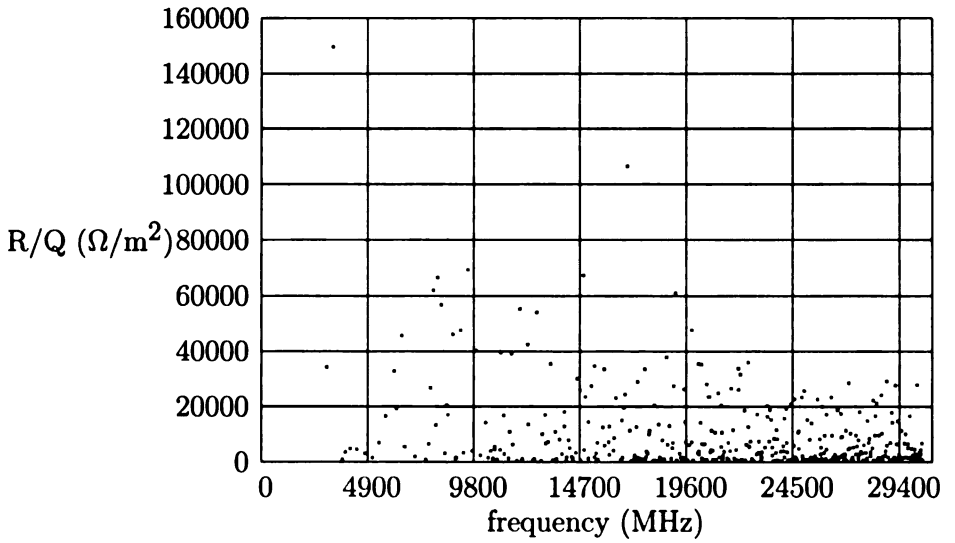


Figure 4.8: The $R/Q$s for the dipole modes of the two-cell cavity as a function of frequency.

# Chapter 5

# Prototyping

## 5.1 Fabrication

Two 2-cell cavity prototypes were fabricated from 250 RRR niobium. They were deep-drawn from 4 mm thick sheets with a manually operated 25 ton hydraulic press. A separate coining die was used after deep drawing to compensate for spring back of the niobium half cells. Interlocking equatorial weld preps (total thickness 2 mm) were machined with an end mill. The flanges were made of NbTi. For vacuum sealing, 3-3/4 inch knife edges were machined into the flanges. The niobium tubes were formed by spinning, using a mandrel made of 7075 T6 aluminum. The flanges were tungsten-inert-gas (TIG) welded to the beam tubes and all remaining cavity welds were done with an electron beam at Sciaky, Inc. in Chicago, Illinois. A photograph of the beam tubes, flanges, and half-cells is shown in Figure 5.1. Small titanium dishes attached to the flanges are present for the purpose of welding a helium vessel around the cavity in the future. An additional 0.015 inches of material was left at the weld preps to allow for electron beam weld shrinkage.

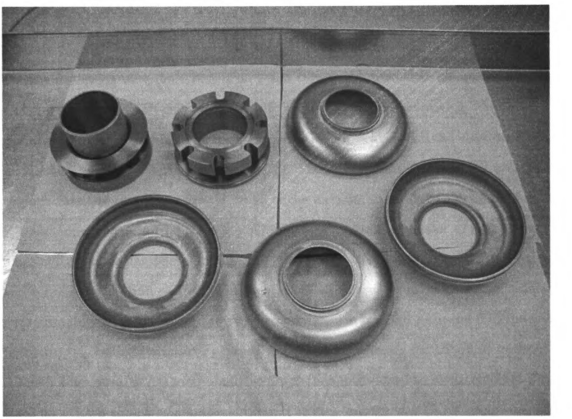

Figure 5.1: Niobium half cells after stamping and machining for weld preps.

### 5.1.1 Electron Beam Welding

This discussion expands upon notes on electron beam welding from Robert Wagner [22]. The weld preps were cleaned just prior to welding by soaking the parts in a 1:1:2 acid BCP for 5-7 minutes. This removed a layer of material approximately 10 $\mu$m thick. After a rinse with distilled water and ultrapure water, the parts were assembled for welding. The welding of a half-cell to a beam tube is shown in Figure 5.2. The parts are held in a rotating fixture. The electron gun (shown on the left in Figure 5.2) can be moved and rotated. For the 2-cell welds, the gun remains stationary and the cavity parts rotate over 360°. Electron beam welding of high RRR niobium requires a better vacuum than is typical for electron beam welds. The pressure used in the Sciaky welder was 50 $\mu$torr. The aluminum fixture never touched the cavity parts

directly to avoid diffusion of foreign material into the hot niobium: small niobium tabs are placed between the part and the fixture (see Figure 5.2).

The iris welds were done first: The beam tubes were welded to the end half-cells and the two middle half-cells were welded together at the iris forming a "dumbbell". As illustrated in Figure 5.2, the iris welds were inside welds (with the electron beam incident on the inside surface of the cavity). This means that the weld did not need to penetrate through the entire thickness of the niobium to produce a good RF joint. It takes approximately 1 hour for the 68" ×68" ×84" vacuum chamber to pump down. The rotating table has chucks for 4 independent assemblies, allowing several iris welds to be done in one pump-down. The welding itself was not time consuming, taking approximately 20 seconds. But, to avoid contamination from air diffusing into the hot niobium, the welded parts were allowed to cool under vacuum for about 40 minutes. A small amount (100-200 torr) of nitrogen was then introduced to aid in cooling. The total cool-down time was about one hour. The gun voltage was 50 kV and, after an initial tack weld to keep parts aligned, a partial weld around each iris was done with 30-35 mA of beam.

The final round of welding was for the equators of the cells. The cavity was assembled vertically on the rotating chuck in the same orientation as shown in Figure 5.2. The beam came from the side and was incident on the outside surface of the cavity. Therefore the weld had to penetrate through the entire thickness of the cavity, which was 2 mm at the weld prep, to ensure a smooth inner surface. The beam current was carefully chosen to ensure that it was large enough for full penetration but low enough to avoid a "blow through". The beam was rastered to slightly defocus it, and avoid weld spatter. The fixture used springs to help maintain contact while shrinkage occurred during the welding. A spot weld of approximately 2.5 cm was done at 4 locations on both the top equator and the bottom equator to keep the parts aligned. After spot welding, a shallow (40 mA) seal weld was done at a rate of 18 inches per minute along the entire circumference of the top equator. The full penetration weld

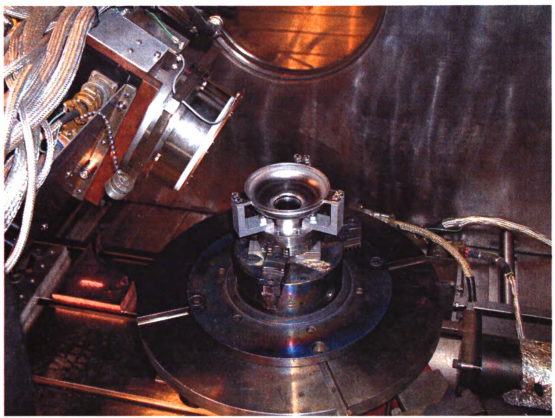

Figure 5.2: Setting up for an iris weld inside the vacuum chamber of the electron beam welder. The electron gun is visible on the upper left. Parts for a single cell $\beta = 1$ cavity are shown; the welding of the 2-cell cavity was done the same way.

was started with a beam current of 52 mA at 12 inches per minute. The current was reduced to 50 mA for the remainder (approximately 90%) of the weld. The top equator was welded first to help avoid misalignment due to weld shrinkage. A seal weld and a full penetration weld were then done in the same manner for the bottom equator.

After cool-down it was noticed that the there was a sector of the top equator weld which did not have full penetration, while the bottom equator had full penetration throughout. This difference was attributed to the heating from the top weld decreasing the beam current necessary for full penetration of the bottom weld. The top weld was redone with 12% more beam current along a $90^{o}$ sector centered on the gap. The second cavity was welded with 52 mA for the top weld and 50 mA for the bottom

weld. The welds in both cells looked fine after cooldown and inspection. A photograph of one of the complete cavities is shown in Figure 5.3.

Figure 5.3: A completed 2-cell cavity.

### 5.1.2 Waveguide Coupling Measurements and Choice of Beam Tube Length

For vertical testing of a cavity, the niobium beam tube is made long enough to ensure that the field levels at the stainless steel connecting flange are negligible. One of the beam tubes of the 2-cell cavity was deliberately made shorter so that the fabricated cavities could be used for additional experiments. One such experiment would be

to test the feasibility of a circular normal-conducting copper waveguide as an input coupler for a superconducting cavity. As illustrated in Figure 5.4, the input coupler would be placed outside of the helium vessel and the beam would pass through the waveguide.

Figure 5.5 is an top-view cartoon. The waveguide is shorted at the top and the electric field of the TE11 waveguide mode couples to the TM010 mode of the cavity. One would expect the coupling strength to increase as the distance separating the cavity and the waveguide decreases. However, there are mechanical constraints on how close the cavity and waveguide may be placed to each other with the waveguide outside the helium vessel. One basic question was whether sufficient coupling could be achieved in such a configuration.

One of the 2-cell cavity beam tubes was to be made short enough to be used to test such a coupler. Bench top RF tests were done with a single-cell copper model to measure the coupling between the cavity and the waveguide. The copper model has the same cell shape as the 2-cell cavity. These measurements were then used to determine the beam tube lengths for the 2-cell cavity. Figure 5.6 shows a diagram of the test setup.

First, with the cavity removed from the waveguide, the RF power from the network analyzer was applied to feedthrough B. Reflections from the feedthrough were reduced to approximately zero by adjusting the length of a small wire antenna attached to the center conductor of the feedthrough. An antenna length was found for which the real part of the input impedance at B is 50 $\Omega$. To match the entire input impedance at B to 50 $\Omega$, the imaginary portion must be eliminated. This was accomplished by sliding the position of sliding short D. The same procedure was used to provide a matched input at feedthrough A by adjusting the position of sliding short C. The position of this short remained fixed throughout the testing to provide a matched connection between the waveguide and the network analyzer. The single-cell copper cavity F and collar G were next attached to the waveguide. RF power from the network analyzer was

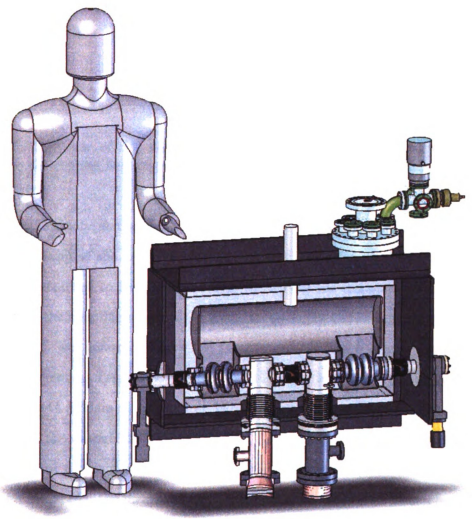

Figure 5.4: The feasibility of a proposed normal-conducting waveguide input coupler may be tested with the 2-cell cavity. The TE11 wave in the copper waveguide would couple to the TM010 mode of the cavity and the beam would pass through the waveguide. The waveguide feed is below the beam line, with a waveguide short above it.

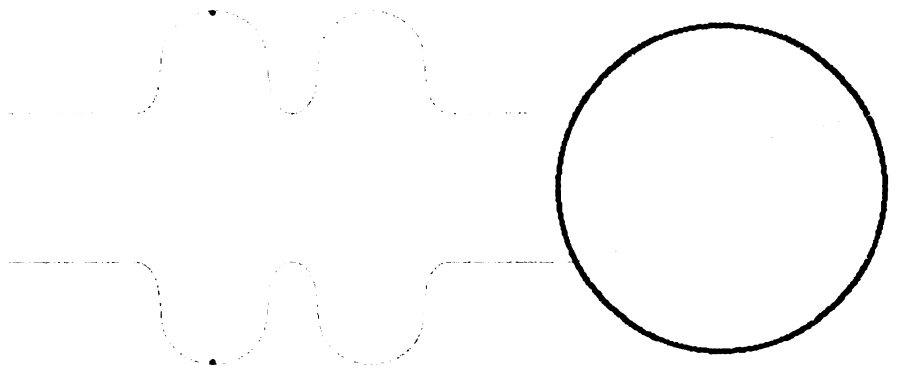

Figure 5.5: Top view of the electric field in the waveguide (shown as a cartoon) coupling to the electric field of the TM010 $\pi$-mode (from SUPERFISH).

supplied to the cavity at the N-type feedthrough E. The input at E is also matched to 50 $\Omega$ to maximize the cavity field level. The RF detection port of the network analyzer was attached to feedthrough A. By measuring the transmission from point E to point A, the coupling strength, or $Q_{\text{ext}}$, between the cavity and the waveguide at the collar G was inferred. There are two parameters which affect this coupling strength: the distance $d$ seperating sliding short D from the beam line and the length of the collar at G. Collars of various lengths were used to vary the separation between the cavity and the waveguide, and thereby vary the $Q_{\text{ext}}$. For each collar length, $Q_{\text{ext}}$ was measured at different $d$. Since a two-cell cavity will have twice as much stored energy as a single cell, the measured $Q_{\text{ext}}$ values were multiplied by two. The results are plotted in Figure 5.7.

Envisioning the transverse electric field of the TE11 waveguide mode coupling to the axial field of the TM010 cavity mode as in Figure 5.5, it is reasonable to anticipate a maximum in the coupling when the short is located approximately one quarter RF wavelength away from the beam line and a minimum in the coupling when the short is located approximately one half RF wavelength away from the beam line. This was in fact measured, as seen in Figure 5.7. The strongest coupling occurs when

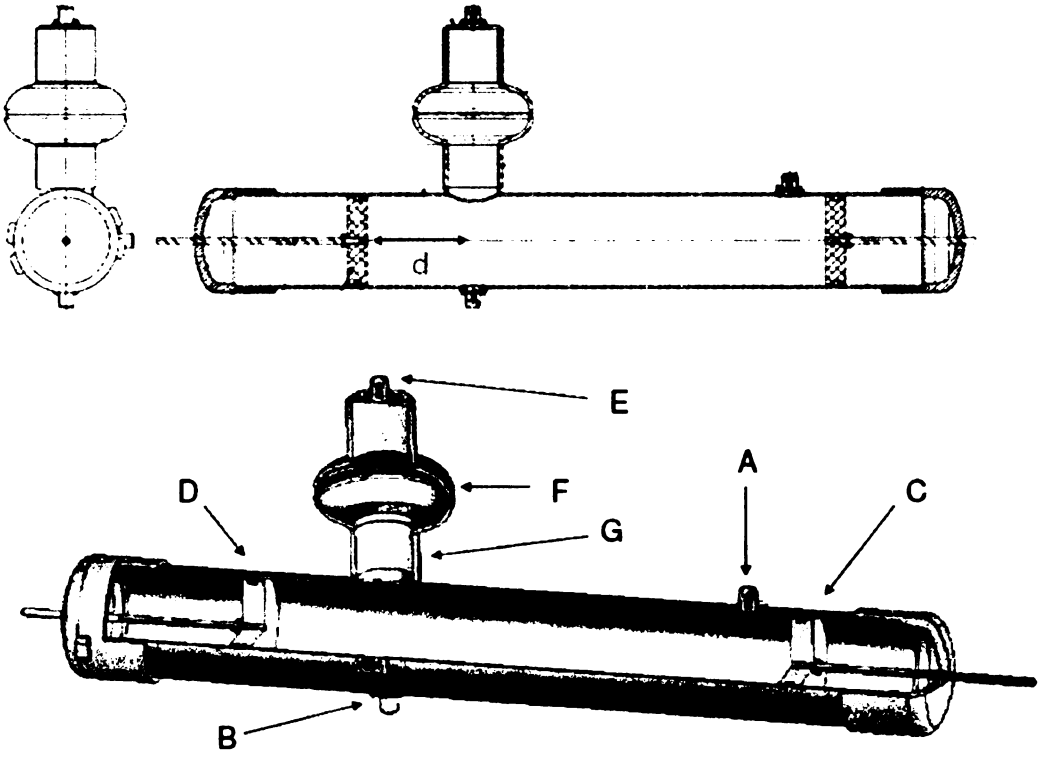


Figure 5.6: A copper waveguide with moveable shorts at either end is used with a network analyzer to measure the coupling strength of the TE11 mode of the guide to the TM01 mode of the cavity as a function of the short to beam line distance $d$: A) N-type coaxial feedthrough B) N-type coaxial feedthrough C) sliding short D) sliding short E) N-type coaxial feedthrough F) copper single cell G) removable collar.

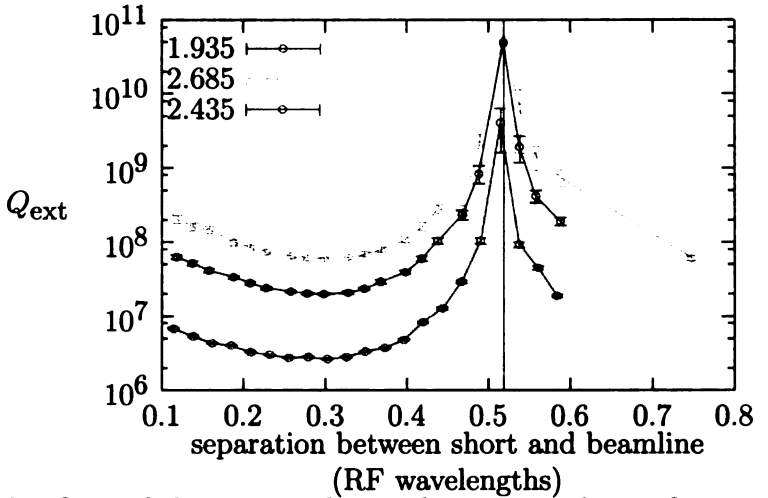


Figure 5.7: The $Q_{\text{ext}}$ of the waveguide coupler measured as a function of the position of the sliding short closest to the cavity. The other short remained fixed. The measurement was repeated for several different distances between the cavity and the waveguide:1.935 in, 2.435 in, and 2.685 in. The $Q_{\text{ext}}$ values shown are for a 2-cell cavity, scaled from measurements on a single-cell cavity.

the $Q_{\text{ext}}$ is lowest. Another consideration which affects the beam tube length is the power dissipated in the copper waveguide. The beam tube must be short enough to establish adequate coupling, however the cavity will be loaded by the copper more if it is closer to the waveguide. The decrease in $Q_0$ due to dissipation in the copper walls is approximately found from SUPERFISH simulations for a two-cell cavity with long beam tubes by considering a long beam tube which is niobium near the cavity and copper past a chosen distance $L$ away. The simulation uses the surface resistance of niobium and the calculated values of the surface magnetic field to determine the power dissipated in each segment of the cavity geometry. If the copper waveguide is to be located a distance $L$ from the cavity, then the additional heating in the copper may be estimated by first finding the dissipated power in one of the beam tubes, starting at the distance $L$ from the cavity and extending to the end of the tube, then multiplying this power by the ratio of the surface resistance of copper to the surface resistance of niobium. The total dissipated power was then found by adding the estimate of the power dissipated in copper to the power dissipated in the remaining segments, which

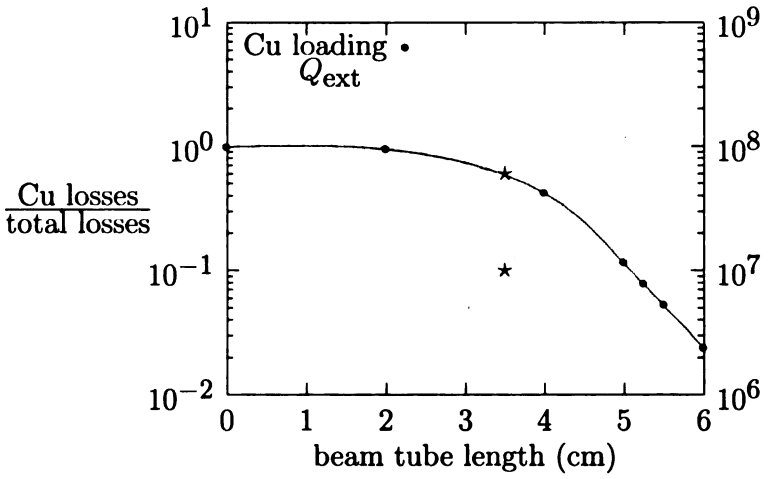


Figure 5.8: The percentage of power that is dissipated in the copper waveguide is compared with the coupling strength of the waveguide. Both quantities have a strong dependence on the length of the gap separating the cavity and the waveguide. The stars indicate the chosen final beam tube length of 3.5 cm.

are taken to still be niobium. The $Q_0$ was then calculated as

$$Q_0 = \frac{\omega U}{P_{Nb} + P_{Cu}} = \frac{\omega U}{P_{Nb}} \left( \frac{P_{Nb}}{P_{Nb} + P_{Cu}} \right) = Q_{Nb} \left( \frac{P_{Nb}}{P_{Nb} + P_{Cu}} \right), \quad (5.1)$$

$$\frac{Q_0}{Q_{Nb}} = 1 - \frac{P_{Cu}}{P_{Nb} + P_{Cu}}. \quad (5.2)$$

The lowest measured $Q_{ext}$ for a given cavity-coupler separation and the fraction of power dissipated in copper are plotted in Figure 5.8. For the calculation of the dissipated power, a niobium surface resistance of 15 n$\Omega$ and a copper surface resistance of 12.861 m$\Omega$ were used. To be conservative, the value for the surface resistance of copper is based on the resistivity at room temperature; the power dissipation in the copper can be expected to decrease in the case of copper at lower temperature. At large tube lengths, the $Q$ loading due to copper is small, but the $Q_{ext}$ is large. At short tube lengths, the $Q$ loading due to copper is large, but the $Q_{ext}$ is small. The exponential dependence of the $Q_{ext}$ on tube length is expected since the evanescent fields of the TM010 mode diminish exponentially in the beam tube. The rate of decay $\frac{2.405}{2.39\text{cm}} = 1.01\ \text{cm}^{-1}$ is roughly consistent with the 6 dB/cm seen in Figure 5.8. The beam tube

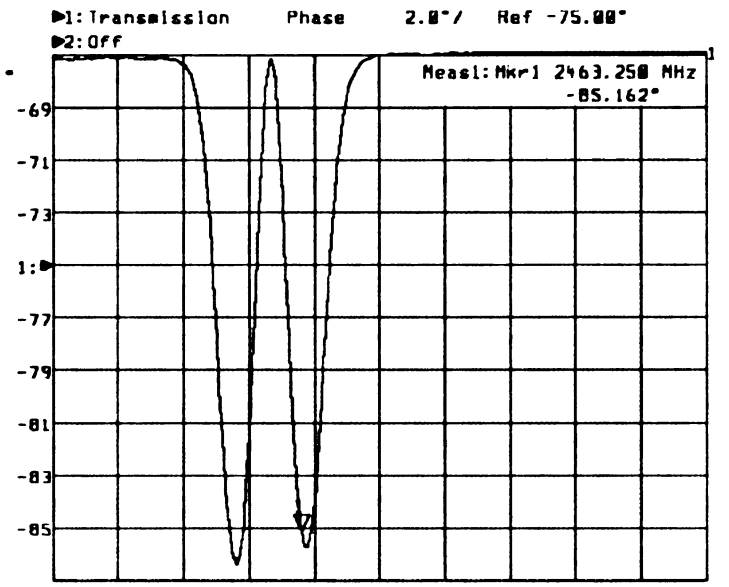


Figure 5.9: A small metal bead was pulled along the axis of the 2-cell cavity with fishing line. The bead causes the resonant frequency to shift by an amount proportional to $|E_z|^2$ and this in turn causes the measured CW phase to decrease.

length used for the 2-cell cavity was chosen to be 3.5 cm long, corresponding to $Q_{\text{ext}} = 10^7$ and $\frac{Q_0}{Q_{\text{Nb}}} = 40\%$. The beam tube which would not be connected to a coupler was chosen to be 6.0 cm long, corresponding to copper losses less than 3% of the total. The measured waveguide coupling is not strong enough for heavily beam-loaded cavities, such as an injection cavity, where $Q_{\text{ext}} \approx 10^5$ is needed. However, cavities operating in energy recovery mode often have $Q_{\text{ext}} \approx 10^7$ to increase the stability of the accelerating mode in the presence of microphonic fluctuations. The 2-cell cavity with a tube length of 3.5 cm may therefore be useful for future investigations of the feasibility of the waveguide coupler.

### 5.1.3 Bead Pulls

After completing the welding of the 2-cell cavities, a bead pull was done to measure the field flatness of the $\pi$-mode. The method is based on Slater's theorem [14]. The cavity is excited with the network analyzer and a transmission measurement is used to identify the resonant frequency of the $\pi$-mode. The phase of the transmitted wave

is then detected and displayed. The phase decreases by $\pi$ when the RF frequency is increased through the cavity resonance. This change is more rapid for higher $Q$ cavities and is approximately linear for frequencies close to the resonant frequency. Phase measurements therefore have the advantage of increased sensitivity: a small change in the resonant frequency will cause a large change in the detected phase. Instead of continuously sweeping through a frequency range, the network analyzer was then set to measure transmission at a fixed frequency, the resonant frequency of the unperturbed cavity. A metallic bead travelling along the beam line will shift the resonant frequency down, resulting in a decrease in the phase measured at the original, unperturbed resonant frequency. Since, for small perturbations, changes in phase are linearly related to changes in frequency, the measured relative changes in phase are equal to the relative changes in the resonant frequency.

A 1 mm long section of a hypodermic needle was threaded onto a fishing line and fed through the cavity along the axis. A small bead is desirable in this case since the perturbation must be small and the cavity itself is rather small. The bead removes a small region of the electric field energy density as it moves along the axis. This perturbation will reduce the frequency of the cavity mode according to Equation (2.88). The measured drop in frequency is therefore proportional to the square of $E_z$ at the location of the bead. Figure 5.9 shows the network analyzer trace of the phase as a function of time. The entire time for the trace was approximately one minute. By taking the square root of the measurement and calculating the deviation of the peak axial fields from the average of the peaks, a field flatness within 3% was calculated for both cavities. No tuning was done to either two-cell cavity since field flatness within 5% is adequate for multicell cavities.

## 5.2 Testing

Figure 5.10 shows a diagram of the setup for vertical testing of the 2-cell cavity. The bottom flange is connected to the short beam tube and has openings for a vacuum line and the input coupler. The top flange is connected to the long beam tube and has a single opening for the pickup coupler. The top and bottom flanges are both made of stainless steel, and the power dissipation in these components would be high during testing if nothing were done to shield the flanges from the cavity fields. A thin niobium disk was therefore made to function as both a gasket for the knife edges of the vacuum seals and to shield the inner surface of the stainless steel flange from the cavity fields. The niobium disk was used on the short beam tube since this endcap has higher fields than the long beam tube end cap. The Nb disk therefore had two holes cut into it for the vacuum line and input antenna. A thin copper disk with a center hole for the pickup antenna was used for the long beam tube flange at top. Copper was used in an attempt to simulate the conditions of possible future tests with a copper waveguide coupler. SUPERFISH simulations predicted a 20% drop in $Q_0$ due to the presence of the copper.

The RF input and pickup couplers used antennae with a fixed length for the vertical testing. The lengths of the antennae needed for the desired external $Q$'s were determined by benchtop measurements after the expected $Q_0$ at high fields was estimated. Recent tests at MSU of a single-cell TTF shape cavity with a TM010 frequency of 2.45 GHz resulted in a measured $Q_0$ of $1.8 \cdot 10^{10}$ at 1.5 K. Using the TTF value for $G$, the corresponding surface resistance was calculated to be

$$R_s = \frac{G}{Q_0} = \frac{270\ \Omega}{1.8 \cdot 10^{10}} = 15\ \text{n}\Omega. \tag{5.3}$$

Since the 2-cell cavities were made from the same stock of niobium and operate at the same frequency as the TTF single cell, 15 n$\Omega$ was used as the estimate of the 2-cell

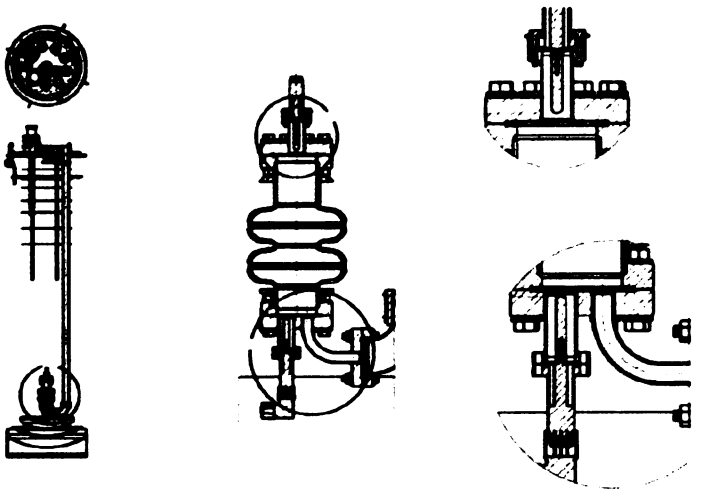

Figure 5.10: The 2-cell cavity is positioned vertically for testing with two fixed-length antennae. The input coupler and vacuum connection are located on the bottom and the pickup probe is located on the top flange. NOTE: The antenna lengths in the picture are not the ones actually used for testing.

cavity surface resistance. The estimated low-field $Q_0$ for the 2-cell cavity is then,

$$Q_0 = \frac{G}{R_s} = \frac{228\ \Omega}{15\ \text{n}\Omega} = 1.5 \cdot 10^{10}, \tag{5.4}$$

including an additional 20% drop due to the copper disk on the top flange, we predict

$$Q_0 = 1.2 \cdot 10^{10} \tag{5.5}$$

for the 2-cell at 1.5 K.

### 5.2.1 Antenna Measurements

The $Q_0$ is expected to drop at high field, however it is not possible to accurately predict by how much. A rough estimate for the high-field $Q_0$ of one third of the low-field $Q_0$ was used to determine the coupling strength of the input and pickup antennae. The goal was to pick an input $Q_{\text{ext}}$ that is close to $Q_0$ at high field. When

these $Q$'s are equal, the cavity impedance is matched to the characteristic impedance of the input line and all of the power available from the amplifier goes to the cavity without reflection. Since the the input antenna length is fixed, a perfect match will not generally exist, but a $Q_{\text{ext}}$ close to $Q_0$ will still minimize reflections and wasted power.

The $Q_0$ of the 2-cell cavity at room temperature was measured with a network analyzer to be 6620. The $Q_{\text{ext}}$ of the input coupler was then measured by using it as a pickup antenna to measure the transmission while the network analyzer was exciting the cavity with a matched input. The desired $Q_{\text{ext}}$ for the input coupler was $4 \cdot 10^9$, corresponding to a coupling coefficient of

$$\beta = \frac{Q_0}{Q_{\text{ext}}} = \frac{6620}{4 \cdot 10^9} = 1.655 \cdot 10^{-6} \tag{5.6}$$

at room temperature. The coupling coefficient, written in terms of the transmission coefficient $|S_{21}| = \frac{P_{\text{ext}}}{P_{\text{f}}}$, is

$$\beta = \frac{P_{\text{ext}}}{P_0} = \frac{|S_{21}|^2}{1 - |S_{21}|^2} : \tag{5.7}$$

$P_{\text{ext}}$ is the power transmitted through the coupler; $P_{\text{f}}$ is the forward power feeding into the cavity from the network analyzer; and $P_0$ is the power dissipated in the copper cavity walls. The desired value of $|S_{21}|$ is therefore,

$$|S_{21}|^2 = \frac{\beta}{1+\beta} \approx \beta = 1.655 \cdot 10^{-6} \tag{5.8}$$

$$= -57.81 \text{ dB}. \tag{5.9}$$

Figure 5.11 shows a plot of the transmission measurements for several antenna lengths. As one would expect, the transmission coefficient and $Q_{\text{ext}}$ increase exponentially as the antenna length increases. An antenna length of 1.61 inches corresponding to $|S_{21}| = -57.81$ dB was extrapolated from the measurements.

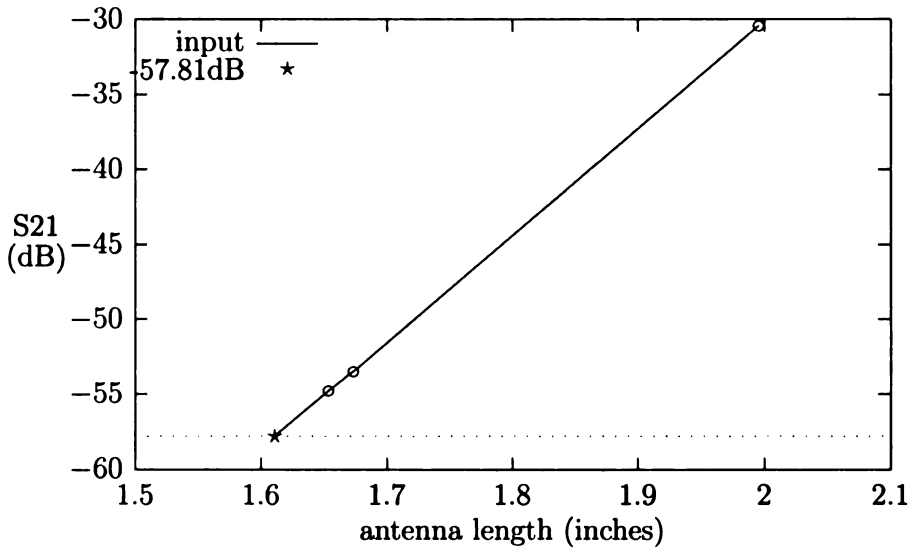


Figure 5.11: The length corresponding to $Q_{\text{ext}} = 4 \cdot 10^9$ (star) is extrapolated from the measured $Q_{\text{ext}}$'s for several different input antenna lengths (circles).

For the vertical test, the pickup antenna's purpose is to sample the field level in the cavity without significantly loading the $Q$. Having the pickup $Q_{\text{ext}} \ggg Q_0$ makes the calculation of $Q_0$ from the measured values simpler. The coupling of the pickup antenna was therefore chosen to be a factor of 100 weaker than the input coupler, resulting in a desired $Q_{\text{ext}}$ of $4 \cdot 10^{11}$. The procedure for determining the antenna length needed for this coupling strength is the same as for the input coupler, where now $|S_{21}| = -77.81$ dB is desired. Figure 5.12 shows the measured values used to interpolate the necessary antenna length. As with the input antenna, the transmission coefficient increases exponentially with antenna length. Note that the $|S_{21}|$ values for the input and pickup antenna do not lie on the same line because the beam tube length and radial offsets are different. The $Q_{\text{ext}}$ values for the fabricated antennae were verified to be in good agreement with the predictions: for example, $Q_{\text{ext}} = 3.3 \cdot 10^{11}$ for the pickup antenna and $Q_{\text{ext}} = 2.7 \cdot 10^9$ for the input coupler.

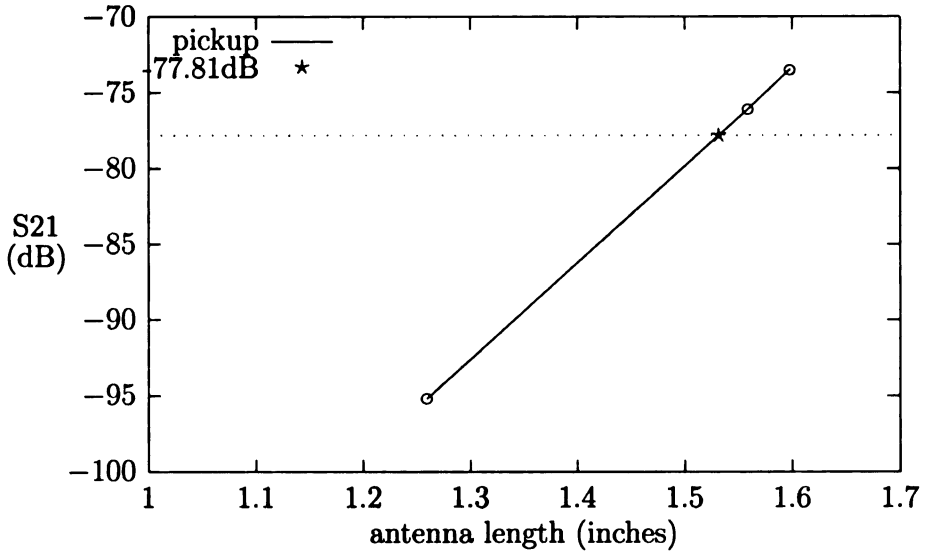


Figure 5.12: The length corresponding to $Q_{\text{ext}} = 4 \cdot 10^{11}$(star) is interpolated from the measured $Q_{\text{ext}}$'s for several different pickup antenna lengths (circles).

### 5.2.2 Cavity Preparation

#### Chemical Etching

The first of the two 2-cell cavities was prepared for testing by first undergoing a chemical polish with buffered chemicals (BCP) which consists of a mixture of hydrofluoric, nitric, and phosphoric acids with a 1:1:2 volume ratio. When this mixture of chemicals is chilled below 18°C, the amount of hydrogen released during the etch is limited. Limiting the diffusion of hydrogen into niobium inhibits the formation of hydride precipitates on the niobium surface at temperatures between approximately 60 K to 150 K. If large amounts of hydride form on the surface, the residual resistance will increase and the $Q_0$ will decrease, a phenomenon known as Q-disease. Hydrofluoric acid is very unforgiving, and potentially deadly, if handled improperly. Additionally, the chemical etching produces corrosive fumes which must be adequately vented. For these reasons, an isolated acid room was constructed, the interior of which is shown in Figure 5.13. It has a sloped floor which would drain any chemicals into a catch basin in the event of a large spill.

Figure 5.13: Preparing to etch a cavity in the acid room.

Teflon flanges are attached to the cavity end flanges, see Figure 5.14, allowing the cavity to be connected to a closed-loop sytem which continuously circulates the acid between the cavity and a chilling tank. The temperature of the acid is measured at the chilling tank to ensure it does not exceed 20°C. The closed loop is contained within a large plexiglass glovebox which provides a protective barrier, contains any fumes, and allows for safe handling of manually operated valves in the loop. Any fumes produced are directed away from the acid room through a "scrubber", which is a tall column filled with neutralizing beads. The neutralized fumes at the top of the scrubber are simply vented outside. The cavity was etched for one hour and 45 minutes with the acid at 13°C, removing approximately 175-195 $\mu$m of material from the surface.

The acid loop was then valved off and valves connecting the cavity to a supply of ultrapure water and a drainage tank in the acid room were opened. The cavity was rinsed with ultrapure water for ten minutes using 55 gallons of water. This dilutes

Figure 5.14: The 2-cell cavity is ready for BCP.

Figure 5.15: The 2-cell cavity underwent high-pressure rinsing with ultrapure water in a class 100 clean room for a minimum of one hour. The high pressure water jets remove foreign particulates from the inner surface to prevent field emission at high RF field.

any residual acid and removes acid residue in the cavity.

### High-Pressure Water Rinsing

The rinsed cavity was then taken to the class 10000 clean room, where the teflon flanges were removed in a stainless steel basin and the cavity was given a final, brief rinse with ultrapure water. The cavity was then moved to the class 100 clean room for high-pressure (1000 to 1100 psi) rinsing (HPR) with ultrapure water. Figure 5.15 shows the arrangement for HPR: the nozzle remains stationary and continuously sprays water in various directions while the cavity moves to enable water to contact every portion of the cavity interior. The cavity is held by an aluminum fixture which moves up and down. A motor attached to the fixture rotates the stand which is bolted to the cavity. This provides simultaneous relative rotation and vertical translation between the cavity and nozzle. The cavity was rinsed in this way for 70 minutes and allowed to dry overnight on a table in the class 100 area.

### Assembly and Leak Checking

The cavity was assembled to the insert inside the class 100 clean room, see Figure 5.16, and pumped down to approximately $1.4 \cdot 10^{-7}$torr. After placing the insert in the small Dewar, pumping, and backfilling the Dewar with He gas, a leak was detected with the residual gas analyzer (RGA). The insert was removed from the Dewar and a leak check revealed a leak at the connection between the vacuum pipe and the elbow. The insert was placed back in the class 10,000 clean room and the copper gasket at this joint was replaced. A leak was then detected at the bottom cavity flange; the vacuum-pipe-to-elbow flange was observed to still have a leak also. Tightening the flanges eliminated the cavity flange leak and reduced the vacuum-pipe-to-elbow leak. The insert was then placed back in the Dewar for testing.

The cavity vacuum was stable enough for testing at temperatures at or above 2.2 K, however testing below the $\lambda$ point of liquid helium was not possible. The absence of viscosity in superfluid helium allowed helium to leak into the cavity, ruining the vacuum. After the initial round of testing, the first cavity was removed from the Dewar. Leak checking revealed that, in addition to the leak at the vacuum-pipe-to-elbow flanges, thermal cycling to cryogenic temperatures and back had opened new leaks in both the top and bottom flanges of the cavity. Inspection of the knife edges on the cavity flanges showed that the surface finish could be improved by polishing. Inspection of the knife edge on the vacuum tube flange revealed a large nick. The vacuum tube flange was cut off and a new one welded on. No leak was detected at room temperature or at 90 K after polishing the cavity flanges. The cavity was reetched, removing approximately 60 $\mu$m of material, followed by 75 minutes of HPR. During the second vertical test, the cavity vacuum was stable down to and below the $\lambda$ point. A second 2-cell cavity had approximately 190 $\mu$m of material removed with BCP, followed by 75 minutes of HPR.

Figure 5.16: Assembly of the 2-cell cavity on the insert in the class 10,000 clean room. The vacuum pumping line and RF feedthroughs are connected to the cavity flanges.

### 5.2.3 Vertical Tests

The two-cell cavities were tested in a vertical helium Dewar which is surrounded by a liquid nitrogen jacket. Multiple baffles located below the top of the insert act as thermal radiation shields. Germanium temperature sensors were placed on the top flange and bottom flange during testing.

#### RF System

A superconducting cavity has a $Q_0$ value on the order of $10^9$ and the frequency is on the order of $10^9$ Hz; the resonance bandwidth is therefore on the order of $(10^9\,\text{Hz})/10^9 = 1\,\text{Hz}$. The fluctuation of the resonant frequency due to small cavity shape changes from external sources of noise is larger than the mode bandwidth. This means that the resonance curve will shift in frequency over time in response to external vibrations. In order to maximize the cavity field, the RF generator must continually adjust its frequency to match that at the peak of the resonance curve. This is accomplished by phase-locking the generator to the cavity. Figure 5.17 shows a block diagram of the components used for the RF measurements during vertical testing. The low-level RF is provided by a signal generator which provides two parameters which the user may adjust during testing: the output power may change in sub-dB increments and the gain of the feedback loop may be adjusted by changing the volts/Hz ratio at the modulation input. Fine tuning of the RF power is useful for measuring the cavity field level at which observed phenomena occur and increasing the loop gain can enable the generator to remained locked to the cavity during processing events, *i.e.* multipacting or field emission. The step attenuator is used to change the forward power level by 1 dB or more. The phase shifter allows fine adjustment of the generator frequency within the bandwidth of the cavity resonace for the purpose of maximizing the cavity field. The function generator produces square pulses in which the frequency (typically on the order of 1 Hz) and time between pulses are both adjustable. The pulses switch the forward power on or off, allowing for the direct observation of the

cavity's transient behavior; this information is ultimately used for determining both the cavity $Q_0$ and $Q_{ext}$. The transmitted power level may be viewed on the spectrum analyzer while the forward and reverse power levels are displayed on an oscilloscope. The numeric values of the forward, reverse, and transmitted powers are displayed by three separate power meters. Separate calibration measurements are done to account for the attenuation in the cables and the effect of the directional coupler and the RF splitters; the calibration coefficients are used to convert from the measured power levels to the actual forward power, reverse power, and transmitted power coupled into and out of the cavity. The generator frequency is measured by a frequency counter. Any electron current intercepted by the pickup antenna is detected with a bias tee and measured with a picoammeter. A bias tee is a device which separates an incoming signal into two branches: one branch contains the AC (or RF) component while the other branch contains the DC component if it is present in the original signal. The low-level RF output of the generator is amplified by approximately 52 dB with a 200 W solid state amplifier. The RF output of the amplifier is sent to the input coupler of the cavity.

### RF Measurement Technique

The cavity signal is mixed with the generator signal and the mixer output is fed into the frequency modulation input of the generator. The mixer output is proportional to the cosine of the phase angle between the two inputs. If the inputs have different frequencies, then the mixer output varies sinusoidally with a frequency equal to the frequency difference of the two inputs. The voltage level at the modulation input of the generator determines the frequency of the generator, which will therefore also vary sinusoidally. As the generator frequency approaches that of the cavity, the frequency of the mixer output reduces until a steady DC voltage is eventually reached: at this point, the generator and cavity have the same frequency and the generator is said to

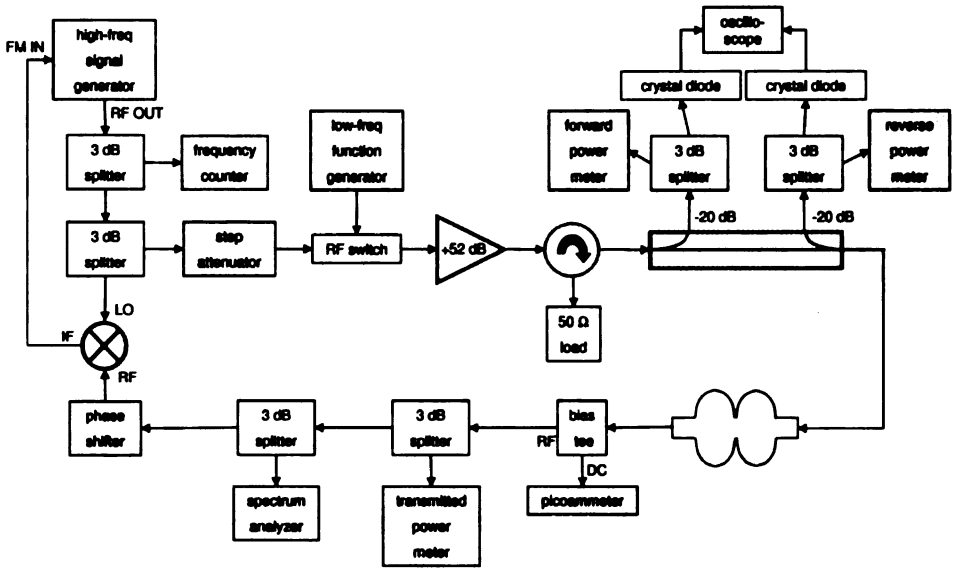


Figure 5.17: The signal generator is phase-locked to the cavity by mixing the transmitted signal from the cavity with the generator signal. The generator (LO) is locked to the cavity (RF) when the frequencies of the two signals are equal. In this case, the mixer output (IF) is a DC voltage, the value of which depends on the phase difference between the cavity and generator.

be locked to the cavity. Once a lock is established, the cavity field may be maximized by a final fine adjustment of the cavity frequency via the phase shifter. The cavity phase changes by approximately $\pi$ through a frequency range on the order of the relatively small resonance bandwidth. Coarse changes in phase, by adjusting the phase shifter, therefore result in fine changes in the generator frequency. The phase shifter is adjusted until the generator frequency is set at the resonace peak, which occurs when the cavity field is maximized. The maximum in the cavity field is observed as a maximum in the transmitted power since the latter is proportional to the square of the cavity field.

At this point with CW RF power applied, the forward power, reverse power, and transmitted power are recorded as well as the cavity frequency, helium bath pressure, and temperature. The coupling coefficient $\beta_1$ for the input coupler can be calculated:

$$\beta_1 = \frac{\sqrt{P_f} \pm \sqrt{P_r}}{\sqrt{P_f} \mp \sqrt{P_r}}. \tag{5.10}$$

In Equation (5.10), the top sign is used when the cavity is overcoupled while the bottom sign is used when the cavity is undercoupled. To determine if the cavity is overcoupled or undercoupled, the forward power is pulsed using the function generator and the traces of the forward power and reverse power as a function of time are displayed with the oscilloscope. At the beginning of the pulse, the reverse power will increase suddenly to a value proportional to the square of the magnitude of the wave principally reflected from the cavity. The energy stored in the cavity increases to a steady state value after which point the pulse ends. Immediately after the pulse ends, the forward power is zero and the undriven cavity emits power through the input coupler, causing the reverse power to rise suddenly. If the emitted power signal immediately following the end of the pulse is greater than the signal of the principally reflected wave, then the cavity is overcoupled. If the emitted signal is less than the principally reflected signal, then the cavity is undercoupled. When the two signals

are equal, the cavity has unity coupling. The power dissipated in the cavity walls is given by

$$P_{\mathrm{d}} = P_{\mathrm{f}} - P_{\mathrm{r}} - P_{\mathrm{t}}. \tag{5.11}$$

The value of $P_{\mathrm{d}}$ calculated from Equation (5.11) can then be used to calculate the coupling coefficient $\beta_2$ of the pickup antenna:

$$\beta_2 = \frac{P_{\mathrm{t}}}{P_{\mathrm{d}}}. \tag{5.12}$$

To extract the values of $Q_0$ and $E_{\mathrm{acc}}$ from these CW power measurements, the $Q_{\mathrm{ext}}$ values for the input coupler and pickup antenna must be measured. This is done by measuring $Q_{\mathrm{L}}$, the loaded $Q$, while the function generator is modulating the forward power. The forward power is zero after the pulse ends and the undriven cavity loses its stored energy at an exponential rate due to three loss mechanisms: dissipating power in the walls, emitting power through the input coupler which is measured as reverse power, and emitting power through the pickup antenna which is measured as transmitted power. The trace obtained with the spectrum analyzer of the exponential decrease in transmitted power is used to measure the rate of decay of the cavity field, from which the value of $Q_{\mathrm{L}}$ is calculated. The time $t$ and signal power level $a$ at two points are recorded and used to calculate $Q_{\mathrm{L}}$:

$$Q_{\mathrm{L}} = -\frac{2\pi f \Delta t}{\Delta \ln(a)} \tag{5.13}$$

where $f$ is the cavity frequency. The results of Equations (5.10), (5.12), and (5.13) can then be used to determine $Q_0$:

$$Q_0 = Q_{\mathrm{L}}(1 + \beta_1 + \beta_2). \tag{5.14}$$

The stored energy may be calculated directly in terms of $P_{\mathrm{d}}$ and the measured fre-

quency:

$$U = \frac{P_{\mathrm{d}}}{2\pi f}. \tag{5.15}$$

SUPERFISH simulation results are used to predict what electric and magnetic fields exist in the cavity for a given stored energy. Finally, the external $Q$'s may be calculated:

$$Q_{\mathrm{ext1}} = \frac{Q_0}{\beta_1} \tag{5.16}$$

$$Q_{\mathrm{ext2}} = \frac{Q_0}{\beta_2}. \tag{5.17}$$

In principle, these values are dependent only on the cavity and coupler geometry, which remains constant throughout the test. In practice, there are slight variations in the calculated values of the external $Q$'s due to a sytematic error in the measurement of the forward and reverse power: the dual directional coupler is not ideal in the sense that the fraction of the forward and reverse signals sent to the power meters has a small dependence on the magnitude and phase of the reverse travelling wave. If there are large reflections because of a large mismatch with the cavity, then the difference between the measured values of $P_{\mathrm{f}}$ and $P_{\mathrm{r}}$ can be on the order of the systematic error, resulting in erroneous values of $P_{\mathrm{d}}$ calculated by Equation (5.11). To reduce the effect of the systematic error on the calculated value of the $Q_{\mathrm{ext}}$'s, the modulated measurements are made at low cavity field. Additionally, the measurements are repeated as the helium bath is cooled by lowering the bath pressure with a roots blower. The calculated values of the $Q_{\mathrm{ext}}$'s remain nearly constant at lower temperatures where the input coupling coefficient is closer to unity. At higher temperatures, there is more variation in the values of the $Q_{\mathrm{ext}}$'s because the cavity $Q_0$ is lower, producing a larger mismatch.

After the modulated measurements are done, a series of CW measurements may be made at various forward power levels and cavity temperatures. Two expressions

may then be used to calculate $Q_0$ using the measured CW power levels and the $Q_{\text{ext}}$ values obtained from the modulated measurements:

$$Q_0 = Q_{\text{ext2}}\left(\frac{P_{\text{t}}}{P_{\text{f}} - P_{\text{r}} - P_{\text{t}}}\right) \tag{5.18}$$

$$Q_0 = \frac{Q_{\text{ext1}}}{2\sqrt{\frac{Q_{\text{ext1}}}{Q_{\text{ext2}}}\frac{P_{\text{f}}}{P_{\text{t}}}} - 1}. \tag{5.19}$$

The field level is determined from the stored energy which is given by

$$U = P_{\text{t}}\left(\frac{Q_{\text{ext2}}}{2\pi f}\right). \tag{5.20}$$

Equation (5.18) is more prone to systematic errors since it relies on calculating the difference between $P_{\text{f}}$ and $P_{\text{r}}$, while Equation (5.19) does not. Additional discussion of this point and derivations of Equation (5.19) and (5.20) can be found in Appendix C.

### First Cavity Test Results

Figure 5.18 shows the CW measurements of $Q_0$ as a function of the accelerating gradient, $E_{\text{acc}}$ at 2.3 K. At $2\,\frac{\text{MV}}{\text{m}}$, the CW measurements were not as stable and a DC current of $-50\,\text{nA}$ was detected by a bias-tee connected to the pickup antenna with no accompanying x-rays. The DC current increased with higher cavity fields. Past $4\,\frac{\text{MV}}{\text{m}}$ the cavity began self-modulating with the DC current reaching $-180\,\text{nA}$ during the transient. At $6\,\frac{\text{MV}}{\text{m}}$ it was possible for the transmitted power to be stable for brief periods of time with no DC current. The DC current and the RF amplitude fluctuations might have been due to soft multipacting barriers. Since the fields were stable for brief periods, it was possible to reach higher fields by pulsing the forward power. After a few minutes of pulsed power, a new stable CW measurement at higher fields was possible. This technique was used to reach the final limiting field of $8.5\,\frac{\text{MV}}{\text{m}}$. Above this limit, the cavity lost phase lock spontaneously.

A vacuum leak prevented testing of the first 2-cell cavity below 2.2 K. The next

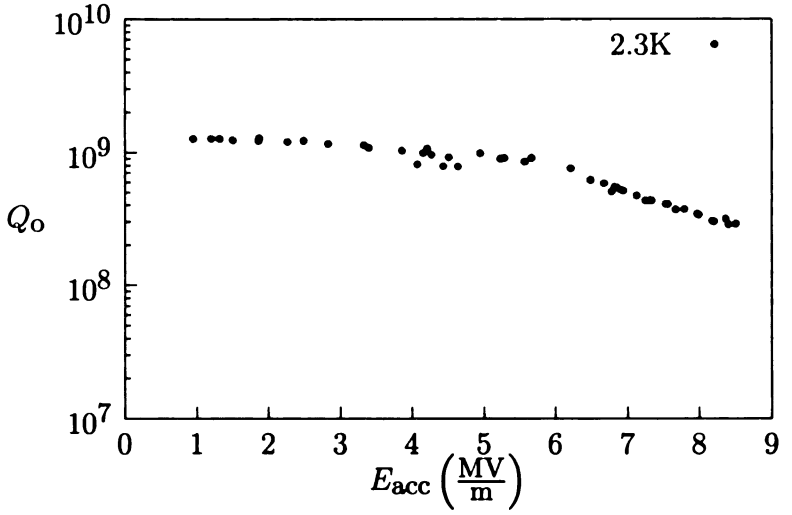


Figure 5.18: Quality factor as a function of gradient for the first test of the first 2-cell cavity at 2.3 K. The maximum $E_{acc}$ was limited: increasing $P_f$ resulted in a spontaneous loss of phase-lock to the cavity.

round of measurements were done after repairing the vacuum leak, as described in the previous section. Figure 5.19 shows the CW measurements of $Q_0$ at various temperatures. At 1.83 K, the cavity fields were stable up to 6 $\frac{MV}{m}$, where the transmitted power would drop suddenly and spontaneously recover. The forward power was then reduced and gradually increased, reproducing the same $Q_0$ values up to 6 $\frac{MV}{m}$. At 6.5 $\frac{MV}{m}$, the cavity pressure rose dramatically, so it was decided to try to reach higher fields in the 0-mode. A limiting field was reached in the 0-mode in which any attempt to increase the forward power would cause the transmitted power to drop by approximately 17 dB. The cavity vacuum was stable again, and upon returning to the $\pi$-mode it was possible to reach a limiting field of 7.4 $\frac{MV}{m}$. Any attempt to increase the forward power beyond this limit would cause the cavity to transition to a new, stable state at 1 $\frac{MV}{m}$ where the $Q_0$ was reduced by about a factor of 20. A comparison of the peak magnetic surface fields reached in the $\pi$-mode and 0-mode before the transition to the low-$Q$ state is shown in Figure 5.20. As can be seen, a higher peak surface magnetic field is reached in the $\pi$-mode. The field and $Q_0$ values for the two modes are similar after the transition.

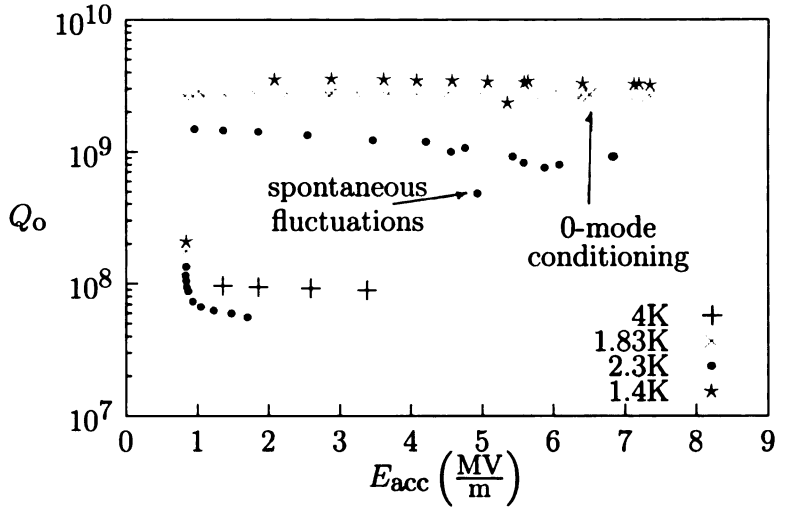


Figure 5.19: During the second round of testing, the first 2-cell cavity experienced a transition at high field to a low-$Q$ state. Reducing $P_f$ in the low-$Q$ state eventually caused a sudden transition back to the high-$Q$ state.

The next set of measurements at 2.3 K (see Figure 5.19) had spontaneous fluctuations in the transmitted power occurring at $5\,\frac{MV}{m}$. At this point, the forward power was switched off and, after it was restored, the transmitted power overshot its previous CW value by approximately 1 dB. After about 1 second the transmitted power returned to its previous, lower value, but oscillating with a variation of about 0.8 dB. The transition to the low-$Q$ state occurred at $6.9\,\frac{MV}{m}$. Increasing the forward power enabled the low-$Q$ state to reach a limiting field of $1.7\,\frac{MV}{m}$, while reducing the forward power resulted in improving the $Q_0$ at the same field level. Reducing the forward power further resulted in a sudden transition back to the high-$Q$ state. A final set of measurements was done at 1.4 K. No instabilities were observed during the measurements at 1.4 K until the low-$Q$ state transition above $7\,\frac{MV}{m}$.

### Second Cavity Test Results

The second 2-cell cavity was tested in hope that the results would facilitate determining the source of the low-$Q$ state. The results are shown in Figure 5.21. During the vertical test at 2 K, self-modulation occurred at $6.6\,\frac{MV}{m}$ with a small amount of

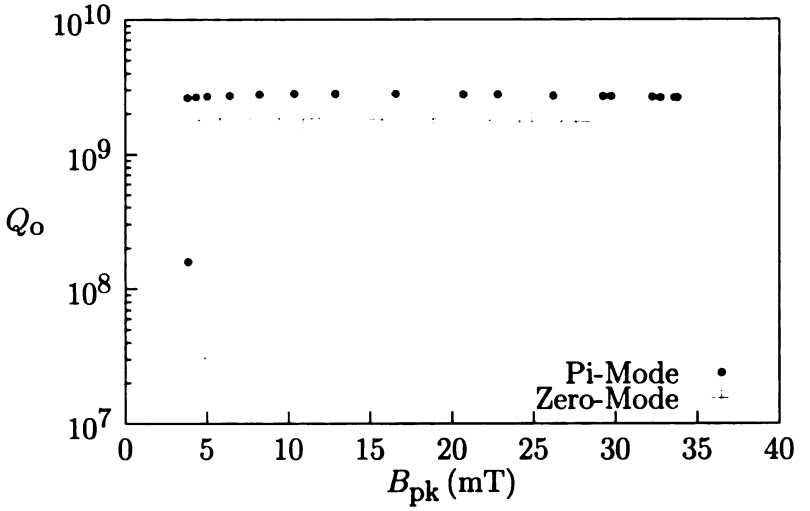


Figure 5.20: The first 2-cell cavity experienced a transition to a low-$Q$ state in both the 0-mode and $\pi$-mode, however the peak magnetic fields reached in these modes is different.

x-rays (0.5-1.5 mR/hour was measured inside the radiation shield). The cavity field was reduced to 1.4 $\frac{\text{MV}}{\text{m}}$ and the forward power was then gradually increased, showing an improved $Q_0$ value at 4 $\frac{\text{MV}}{\text{m}}$. This variation in $Q_0$ values at 4 $\frac{\text{MV}}{\text{m}}$ was also seen in the first cavity test (Figure 5.18), and suggests a possible soft multipacting barrier. The transition to the low-Q state occurred at 8.7 $\frac{\text{MV}}{\text{m}}$. A limiting field of 2 $\frac{\text{MV}}{\text{m}}$ was reached in the low-Q state. Reducing the forward power caused the $Q_0$ to improve while the field level remained constant. As the forward power was further reduced, a sudden transition back to the high-$Q$ state occurred, as we observed for the first cavity.

The field at which the transition occurred was not always reproducible. The following day, an attempt was made to measure more accurately the field level at which the low-$Q$ transition occurred. However, in this case the transition occurred at a lower limit of 8.5 $\frac{\text{MV}}{\text{m}}$. In a subsequant measurement at 1.4 K, the low-$Q$ transition occurred at 8.7 $\frac{\text{MV}}{\text{m}}$.

Measurements on the 0-mode were done at 1.5 K. The comparison with the $\pi$-mode is shown in Figure 5.25. A transition to a low-$Q$ state occurred for both the

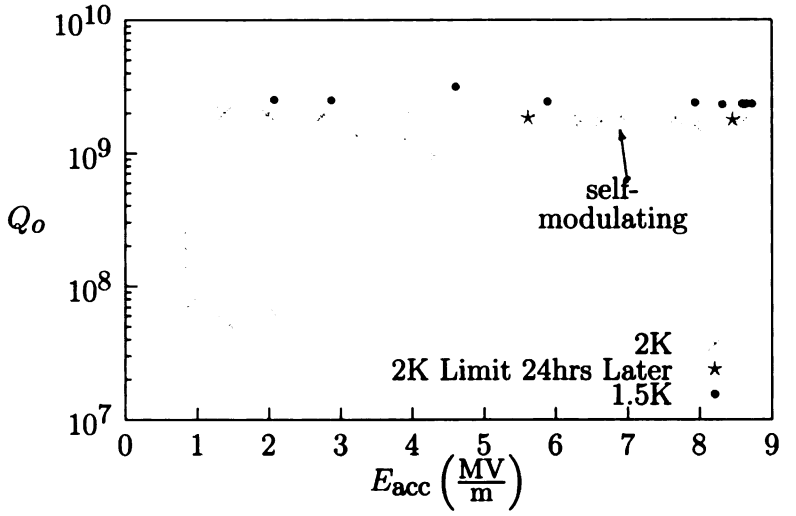


Figure 5.21: The second 2-cell cavity also experienced the sudden transition to a low-$Q$ state at high field.

0-mode and $\pi$-mode. The peak magnetic field reached in the 0-mode was smaller than than for the $\pi$-mode, as was the case for the first cavity.

### Surface Resistance

The low-field $Q$ measurements which were done while pumping the Dewar down to lower pressures and temperatures may be used to calculate the surface resistance of the 2-cell cavities. The surface resistance $R_s$ in terms of $Q_0$ and the geometry factor $G$ is given by

$$R_s = \frac{G}{Q_0}. \tag{5.21}$$

A plot of $R_s$ versus $1/T$, where $T$ is the temperature, for each of the three cavity tests is shown in Figure 5.22. At high temperatures, the surface resistance is seen to follow the BCS form of Equation (1.4). The residual resistance after the low-$Q$ transition appears to increase for both cavities, with the second cavity showing the most dramatic change of the two. The residual resistance for the second cavity is estimated to be in the range of 50 $\Omega$ to 60 $\Omega$.

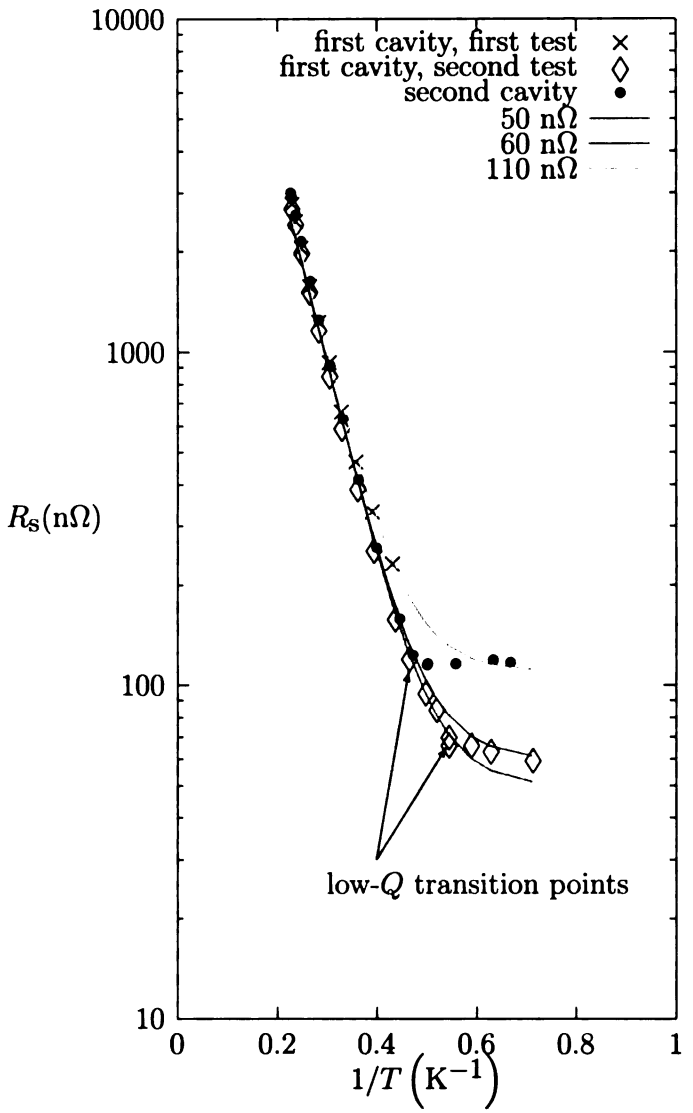


Figure 5.22: The low-field $Q_0$ values measured from the three cavity tests are used to calculate the surface resistance as a function of temperature. Fits to the data are shown where the surface resistance is the sum of a BCS term and a residual term: $R_s = A(2\pi f)^2 \exp\left[-\frac{\Delta(0)}{k_B T}\right] + R_{res}$ where $A = 1.13$, $\Delta(0) = 17.67$, and $f = 2467$ MHz. The BCS contribution is the same for each fit but the residual resistance has values of 50 nΩ, 60 nΩ, and 110 nΩ. The residual resistance of both cavities appears to have increased after experiencing a low-$Q$ transition.

### Frequency Shifts

The helium bath temperature is lowered by reducing the pressure with a roots blower. The pressure differential between the helium bath and the cavity vacuum squeezes the cavity. This squeezing results in small displacements of the cavity surface near the iris. Since the iris is a region of high electric field, the squeezing reduces the resonant frequency of the cavity, by Slater's theorem. The $\pi$-mode frequency was recorded for each $Q$ measurement while pumping down and the change in resonant frequency with pressure may be seen in Figure 5.23. This data, combined with similar results for the second cavity, gives the shift in resonant frequency with pressure to be approximately $-213$ Hz/torr. This value would be useful when fabricating the 2-cell cavity for use in an accelerator, as it is important to ensure that that design frequency can be reached at the design temperature (and the corresponding bath pressure). A small frequency shift with pressure is preferable, since fluctuations in the bath pressure can produce fluctuations in the resonant frequency. The measured shift in frequency with pressure is larger than the value of 10 Hz/mbar (13 Hz/torr) reported for a stiffened 1.3 GHz $\beta = 1$ multi-cell [17]. It is consistent with the values measured for 805 MHz $\beta = 0.47$ single-cell and multi-cell cavities, which ranged from +0.46 kHz/torr to -1.0 kHz/torr, depending on the number of cells, the presence or absence of stiffening rings, and external constaints from a support frame or helium vessel [23].

Lorentz force detuning occurs when the radiation pressure of the cavity field is sufficiently high to deflect the cavity walls enough to change the resonant frequency by a measureable amount. The deflections are small, but the resonance bandwidth of a high-$Q$ superconducting cavity mode can also be very small. When the amount of detuning is greater than the bandwidth, a measureable shift in frequency occurs which is proportional to the square of the field level. Figure 5.24 shows the shift in frequency that occured during testing of the second cavity at a constant bath pressure of 25.8 torr and a bath temperature of 1.99 K. From this data a Lorentz detuning coefficient of $-4.22$ Hz/MV$^2$/m$^2$ is obtained. The measured Lorentz detuning coefficient is larger

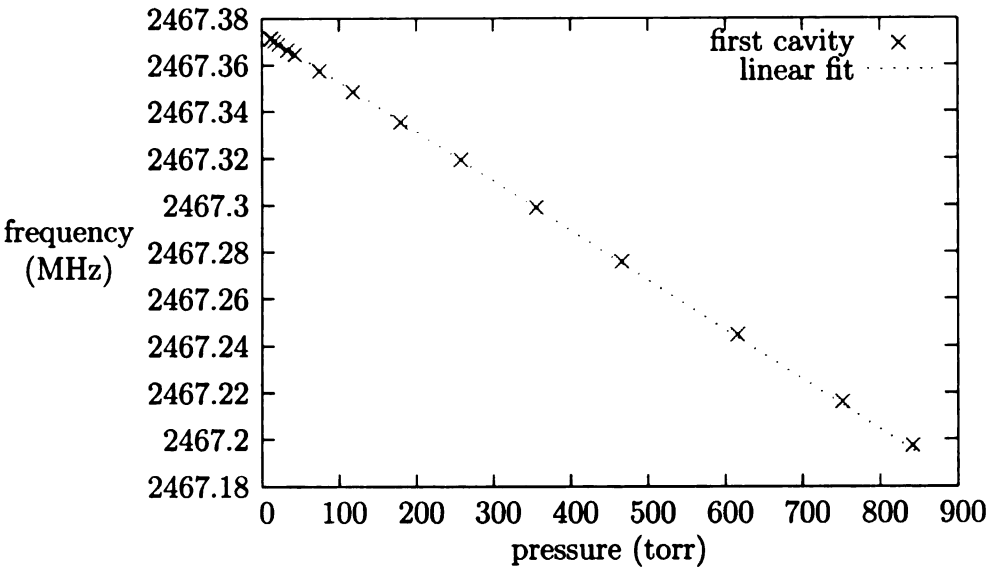


Figure 5.23: The accelerating field of the first cavity is maintained between 0.70 $\frac{\text{MV}}{\text{m}}$ and 1.12 $\frac{\text{MV}}{\text{m}}$ while cooling down. The measured frequencies of the $\pi$-mode show the resonant frequency shift by $-212$ Hz/torr. The same measurements on the second cavity, maintaining $E_{\text{acc}}$ between 0.56 $\frac{\text{MV}}{\text{m}}$ and 1.48 $\frac{\text{MV}}{\text{m}}$, give a value of $-214$ Hz/torr.

than the value of (-)1 Hz/(MV/m)$^2$ reported for a 1.3 GHz $\beta = 1$ multi-cell cavity [17]. It is close to the measured value of -3.5 Hz/(MV/m)$^2$ measured for a $\beta = 0.81$ multi-cell cavity [24]. Note that the latter cavity's $\beta$ value is similar to the 2-cell, but the frequency is lower (805 MHz), stiffening rings were used, and a Ti support frame was attached.

### Discussion

The transition from a high-$Q$ state to a low-$Q$ state at high power levels and the transition from the low-$Q$ state back to the high-$Q$ state when the power is reduced might be explained by a superconducting region of the cavity going normal-conducting at high field. One plausible location for this to occur is the Nb disk on the input flange. The thin outer edge is the only part of the disk in direct contact with liquid He. It is possible that this is not sufficient cooling for the disk to remain superconducting at high field. Prior to testing, simulations were done to predict the $Q_0$ for the case in

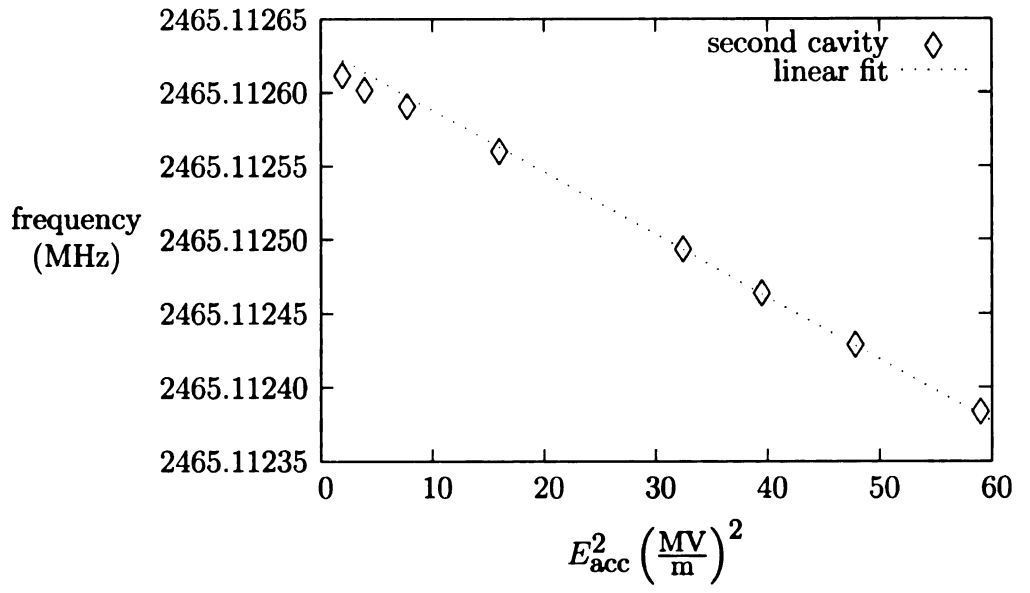


Figure 5.24: The frequency of the $\pi$-mode for the second cavity is measured at different field levels while maintaining a constant bath pressure of 25.8 torr. The shift in the resonant frequency due to radiation pressure of the cavity field is seen to be $-4.22$ Hz/(MV$^2$/m$^2$).

which both the input and pickup flanges used Cu disks and for the case in which only the pickup flange used a Cu disk while the input flange used a Nb disk. Table 5.1 compares the measured ratios of $Q_{low}/Q_{high}$ to the ratio of the $Q_0$'s from the simulations. The measured $Q_0$ ratios are similar to that predicted when the cavity contains two normal-conducting disks for the low-$Q$ state and one normal-conducting disk for the high-$Q$ state. It is also worth noting that the magnetic field at the mechanical joint of the Nb disk and the NbTi flange is 0.9 mT with a peak magnetic field in the $\pi$-mode of 40 mT. This is comparable to the 0.7 mT reached at the Nb-NbTi joint for a quarter-wave cavity tested at MSU [25] and the 1 mT reached in subsequent testing of the same quarter-wave cavity.

Table 5.1: The measured $Q_0$ drop is comparable to that predicted from simulations for the cases of 2 Cu disks and 1 Cu disk

| Cavity | Temp. (K) | $Q_{low}/Q_{high}$ (%) |
|---|---|---|
| $1^{st}$ cavity $\pi$-mode | 1.83 | 6.59 |
| $1^{st}$ cavity $\pi$-mode | 2.3 | 9.52 |
| $1^{st}$ cavity $\pi$-mode | 1.4 | 6.47 |
| $2^{nd}$ cavity $\pi$-mode | 2.0 | 4.38 |
| $2^{nd}$ cavity 0-mode | 1.5 | 6.30 |
| Simulation | 1.5 | 6.04 |

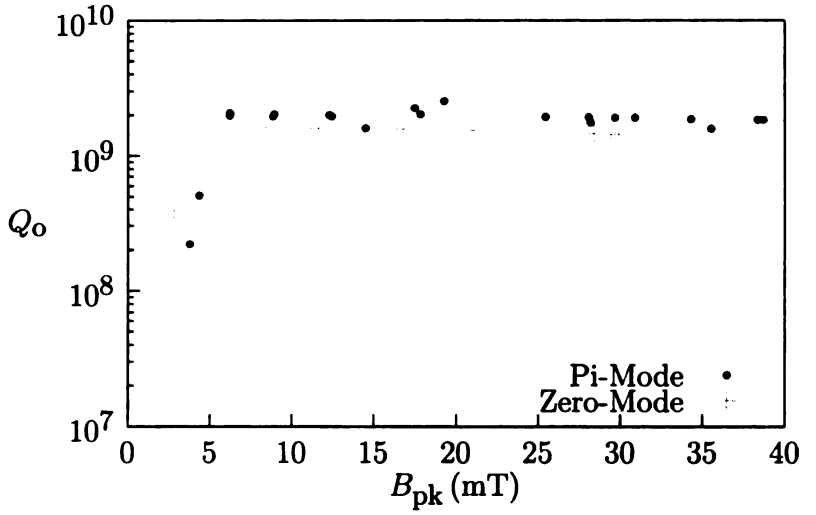


Figure 5.25: The second 2-cell cavity experienced a transition to a low-$Q$ state in both the 0-mode and $\pi$-mode, however the peak magnetic fields reached in these modes is different.

# Chapter 6

# Single-Cell HOM Cavity

## 6.1 Concept

It was seen in Section 1.2.1 that the variation in the field magnitude of individual cells in a multicell elliptical cavity could be understood by modelling each cell as a resonator coupled only to its nearest neighbors. The field magnitude varies sinusoidally from one cell to the next, with different modes having a different phase advance from cell to cell (see Figure 1.5). In this model, the lowest frequency mode has a phase advance of $\frac{\pi}{N}$ where $N$ is the total number of cells in the cavity. This mode has the disadvantage of having the lowest field magnitudes in the end cells. The low fields reduce the coupling of the mode to the beam pipe and to any HOM pickup antennae. This problem worsens for higher cell numbers, further reducing the end cell field strength. Another challenge which develops at higher cell numbers is more tuning being required, since the sensitivity of the $\pi$-mode field pattern to shape imperfections will increase with the square of the number of cells. An attempt to remedy this situation by approximately reproducing the accelerating field pattern of a muticell $\pi$-mode using the TM012 mode of a single-cell cavity is illustrated with the cartoon in Figure 6.1. The simplicity of the single-cell design also has the advantage of reducing the number of electron beam welds or possibly eliminating the welds by

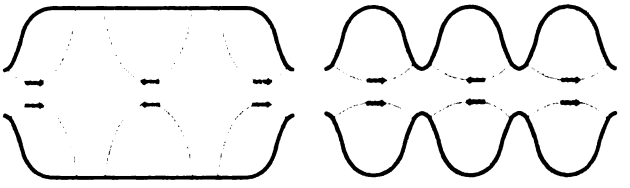

Figure 6.1: A single-cell cavity operating in a higher order TM012 mode produces an accelerating field pattern on axis that superficially resembles that of a 3-cell multicell $\pi$-mode.

hydroforming. The simple shape may also be better suited for depositing thin films of niobium on copper.

The shape of the cavity is essentially that of a large cylindrical waveguide which is shorted at both ends. Many of the characteristics of the HOM cavity may be understood by examining the field patterns and figures of merit for a "pillbox" cavity, which may be solved analytically. However, an important aspect of adding beam pipes to the pillbox deserves mentioning. For an ideal pillbox with no beam pipes using TM01$p$ as the accelerating mode, the length of the pillbox should be close to that of $p$ cells of a multicell cavity that has a $\pi$-mode at the same frequency. The sinusoidal variation of the electric field along the axis would then be approximately equal for the two cavities. Adding beam pipes to the HOM cavity causes two significant changes:

1. The electric field penetrates evanescently into the beam pipe.

2. The peak surface electric field will be located along the edge of the opening.

The iris must be rounded to minimize the peak surface electric field, with a larger radius of curvature required for a larger beam pipe radius. The length of the cavity therefore increases by an amount that is twice this radius of curvature. The final length and field pattern for an HOM cavity with beam pipes operating in the TM01$p$ mode is then closer to that of $p + 1$ cells of a multicell cavity that has a $\pi$-mode at the same frequency.

### 6.1.1 Pillbox Trends

The procedure for designing an HOM cavity shape begins with an initial pillbox shape. The pillbox shape is completely specified in terms of $\frac{l}{a}$, the ratio of the length to the radius. The corners are then rounded to reduce the peak magnetic field. A beam pipe is added and the end shape is optimized by adjusting the parameters of two ellipses connected by a straight section as in elliptical cavity design. Two questions must be initially addressed:

- Which HOM to use, *i.e.* what is the value of $p$ in TM01$p$?
- What should the initial shape of the pillbox be once the value of $p$ is determined, *i.e.* what should the initial value of $\frac{l}{a}$ be?

#### Fields

To answer these questions, the field patterns and figures of merit for the TM01$p$ mode of a pillbox will be solved for as a function of the axial mode number $p$ and the aspect ratio $\frac{l}{a}$. In Section A.2.4, the case of a TM01 waveguide mode travelling in a guide of circular cross-section was considered. The fields for a TM01 wave travelling in the positive $z$ direction with axial wave number $\beta$ was found to be

$$\mathbf{E}^+ = \frac{E_o}{2} J_0(k_c\rho) e^{-j\beta z} \mathbf{n_z} - \frac{E_o}{2} \frac{j\beta}{k_c} J_1(k_c\rho) e^{-j\beta z} \mathbf{n}_\rho \tag{6.1a}$$

$$\mathbf{H}^+ = -\frac{E_o}{2\eta} \frac{jk_o}{k_c} J_1(k_c\rho) e^{-j\beta z} \mathbf{n}_\phi. \tag{6.1b}$$

Cylindrical coordinates $\phi$ (azimuthal), $\rho$ (radial), and $z$ (radial) are used. $E_o$ is the magnitude of the electric field; $J_0$ and $J_1$ are Bessel functions; $\eta$ is the characteristic impedance of free space; $k_c$ is the critical wavenumber; and $k_o$ is the wavenumber for a plane wave in free space. A standing wave may be established by superimposing a wave with the same amplitude but travelling in the opposite direction with axial

wave number $-\beta$,

$$\mathbf{E}^- = \frac{E_o}{2} J_0(k_c\rho) e^{j\beta z}\mathbf{n_z} + \frac{E_o}{2}\frac{j\beta}{k_c} J_1(k_c\rho) e^{j\beta z}\mathbf{n}_\rho \tag{6.2a}$$

$$\mathbf{H}^- = -\frac{E_o}{2\eta}\frac{jk_o}{k_c} J_1(k_c\rho) e^{j\beta z}\mathbf{n}_\phi. \tag{6.2b}$$

The sum of the two travelling waves is

$$\mathbf{E}^+ + \mathbf{E}^- = E_o J_0(k_c\rho)\cos(\beta z)\mathbf{n_z} - \frac{E_o\beta}{k_c} J_1(k_c\rho)\sin(\beta z)\mathbf{n}_\rho, \tag{6.2c}$$

$$\mathbf{H}^+ + \mathbf{H}^- = \frac{-jE_o}{\eta}\frac{k_o}{k_c} J_1(k_c\rho)\cos(\beta z)\mathbf{n}_\phi. \tag{6.2d}$$

This standing wave pattern will remain unaltered if a pillbox of length $l$ is formed by placing shorting plates at locations where the transverse electric field is zero. Everything exterior to the pillbox may now be removed and the field pattern remaining in the pillbox is that of the TM01$p$ mode with $p = \frac{l\beta}{\pi}$.

### Voltage Gain

The voltage gain of a charge travelling at the speed of light along the axis of the pillbox is found by integrating the axial electric field along the axis:

$$V = \left| \int_0^l E_o \cos\left(\frac{p\pi z}{l}\right) \mathrm{e}^{\mathrm{j}\frac{\omega z}{c}}\, dz \right|, \tag{6.3}$$

$$V = \frac{E_o}{2}\left| \int_0^l \left[ \mathrm{e}^{\mathrm{j}\left(k_o + \frac{p\pi}{l}\right)z} + \mathrm{e}^{\mathrm{j}\left(k_o - \frac{p\pi}{l}\right)z} \right] \mathrm{d}z \right|, \tag{6.4}$$

$$V = \frac{E_o l}{2}\left| \mathrm{sinc}\left[\frac{l}{2}\left(k_o + \frac{p\pi}{l}\right)\right] + (-1)^p \mathrm{sinc}\left[\frac{l}{2}\left(k_o - \frac{p\pi}{l}\right)\right] \right|. \tag{6.5}$$

Using the dispersion relation

$$k_o^2 = \left(\frac{2.405}{a}\right)^2 + \left(\frac{p\pi}{l}\right)^2 \tag{6.6}$$

$k_o$ can be eliminated to obtain an expression for the voltage gain in terms of $p$, $l$, and $a$:

$$V = \frac{E_o l}{2}\left|\operatorname{sinc}\left[\sqrt{\left(\frac{2.405}{2}\right)^2\left(\frac{l}{a}\right)^2+\left(\frac{p\pi}{2}\right)^2}+\frac{p\pi}{2}\right]+\right.$$
$$\left.+(-1)^p\operatorname{sinc}\left[\sqrt{\left(\frac{2.405}{2}\right)^2\left(\frac{l}{a}\right)^2+\left(\frac{p\pi}{2}\right)^2}-\frac{p\pi}{2}\right]\right|. \qquad (6.7)$$

where $\operatorname{sinc}(x) = \frac{\sin(x)}{x}$.

### Transit Time Factor

The transit time factor $T$ may be calculated by dividing Equation (6.7) by $\int_0^l |E_z(z)|\mathrm{d}z$:

$$T = \frac{\pi}{4}\left|\operatorname{sinc}\left[\sqrt{\left(\frac{2.405}{2}\right)^2\left(\frac{l}{a}\right)^2+\left(\frac{p\pi}{2}\right)^2}+\frac{p\pi}{2}\right]+\right.$$
$$\left.+(-1)^p\operatorname{sinc}\left[\sqrt{\left(\frac{2.405}{2}\right)^2\left(\frac{l}{a}\right)^2+\left(\frac{p\pi}{2}\right)^2}-\frac{p\pi}{2}\right]\right|. \qquad (6.8)$$

It is a function of the two independent variables $p$ and $\frac{l}{a}$. The transit time factor for a multicell cavity is maximized by setting the midcell length equal to the distance a charge travels in half an RF period. This ensures that the charge experiences forces applied only in the direction of motion. For a charge travelling at the speed of light, this condition may be written as

$$\frac{\omega}{c} = \frac{\pi}{l_{\text{cell}}} \qquad \text{or} \qquad k_o = \beta, \qquad (6.9)$$

Equation (6.9) can never be satisified by the TM01$p$ mode of a single-cell cavity because of the cutoff frequency associated with establishing a standing wave in the

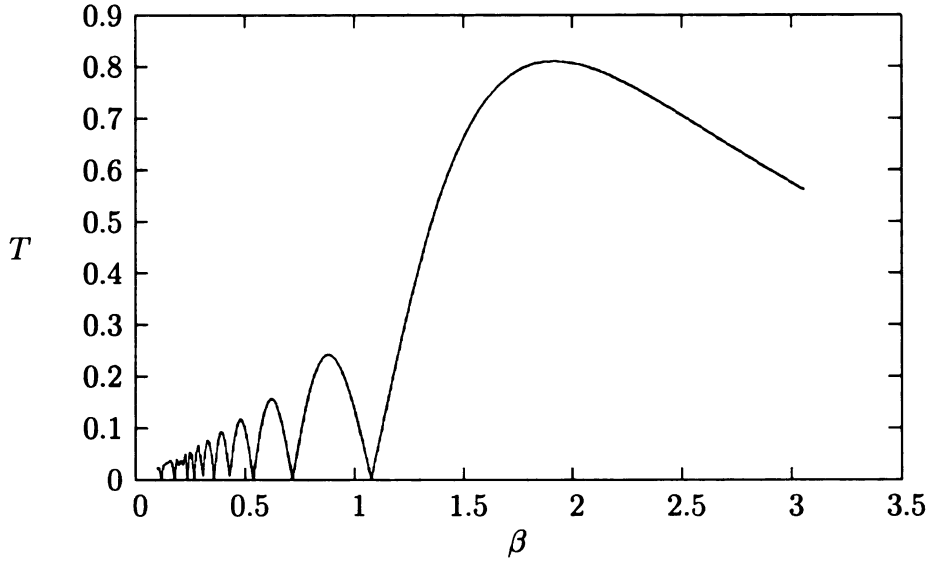


Figure 6.2: The transit time factor $T$ for the TM012 mode of an ideal pillbox with a length to radius ratio of 5 is plotted as a function of particle speed. The maximum $T$ occurs at the physically unattainable $\frac{v}{c} = 1.92$.

radial direction,

$$\left(\frac{\omega}{c}\right)^2 = \left(\frac{2.405}{a}\right)^2 + \left(\frac{p\pi}{l}\right)^2 \qquad \text{or} \qquad k_o^2 = k_c^2 + \beta^2. \tag{6.10}$$

Since $l_{\text{cell}}$ should be set equal to $\frac{l}{p}$, Equation (6.9) is incompatible with Equation (6.10). Agreement with Equation (6.9) improves as the pillbox radius $a$ increases. In the limit $a \rightarrow \infty$, the fields in the pillbox become those of free space and Equation (6.9) is exactly satisfied. Some of the challenges in designing an HOM cavity may be understood from Figure 6.2, which shows $T$ for the TM012 mode as a function of the particle velocity $\frac{v}{c}$.

As anticipated from Equation (6.10), the maximum energy gain occurs for a particle velocity greater than the speed of light. Additionally, for $\frac{v}{c} \approx 1$, $T$ is approximately 0.14 ,which is significantly lower than what may be achieved ($T \approx 0.7$) for multicell elliptical cavities. A low $T$ implies a low voltage gain and figures of merit such as $\frac{R}{Q}$, $\frac{B_{\text{p}}}{E_{\text{acc}}}$, and $\frac{E_{\text{p}}}{E_{\text{acc}}}$ will therefore degrade as a result. For this reason, it is desirable to choose a pillbox shape which has a local maximum in $T$ near the design particle

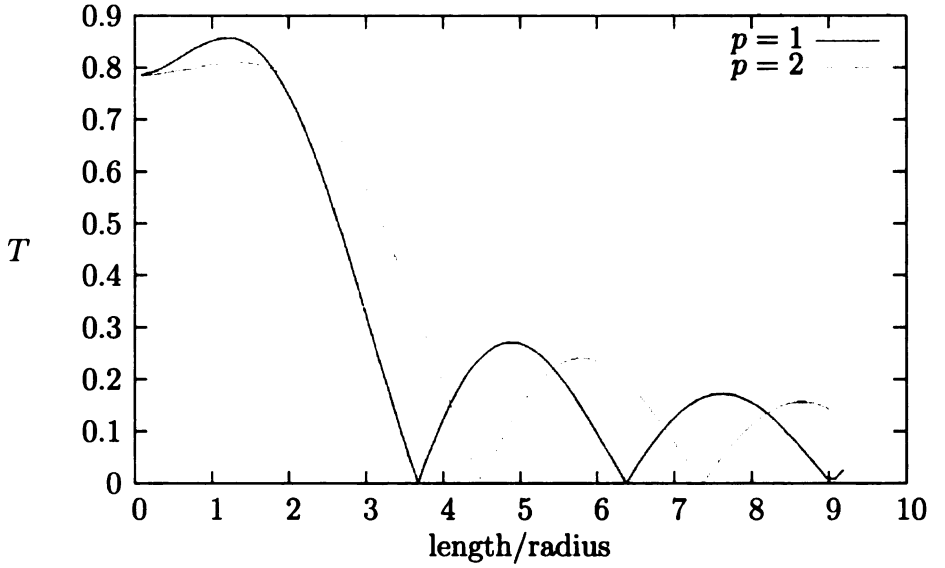


Figure 6.3: The transit time factor $T$ for the TM011 and TM012 modes of an ideal pillbox is plotted as a function of the ratio of length to radius. $T$ is calculated with a constant particle speed of $\frac{v}{c} = 1$.

speed. Figure 6.3 shows that the shape which maximizes $T$ generally depends on the chosen value of $p$.

It is therefore useful to have explicit expressions for both $\frac{B_{\mathrm{p}}}{E_{\mathrm{acc}}}$ and $\frac{R}{Q}$ in terms of $p$ and $\frac{l}{a}$: the goal is then to determine which values of $p$ and $\frac{l}{a}$ produce a sufficiently high $\frac{R}{Q}$ and low $\frac{B_{\mathrm{p}}}{E_{\mathrm{acc}}}$.

### Figures of Merit

The peak magnetic field may be found from Equation (6.2d):

$$B_{\mathrm{p}} = \frac{E_o k_o}{c k_c} J_1(1.84). \tag{6.11}$$

$\frac{B_{\mathrm{p}}}{E_{\mathrm{acc}}}$ as a function of $\frac{l}{a}$ and $p$ is then

$$\frac{B_{\mathrm{p}}}{E_{\mathrm{acc}}} = \frac{E_o l k_o}{c V k_c} J_1(1.84). \tag{6.12}$$

The energy $U$ stored in the mode may be calculated by evaluating the average energy $U_h$ stored in the magnetic field,

$$\begin{aligned} U &= 2U_h = \frac{\mu_o}{2}\int H_\phi^2 d\tau \\ &= \frac{\mu_o}{2}\left(\frac{E_o k_o}{\eta k_c}\right)^2 \int_0^{2\pi}\int_0^l\int_0^a J_1^2(k_c\rho)\cos^2(\beta z)\rho d\phi dz d\rho. \end{aligned} \tag{6.13}$$

This integral may be evaluated using the following property of Bessel functions:

$$\int_0^a \rho J_n^2(k\rho)d\rho = \frac{a^2}{2}\left[J_n^2(ka) - J_{n-1}(ka)J_{n+1}(ka)\right], \tag{6.14}$$

resulting in a final expression

$$U = \frac{\pi}{4} l\epsilon_o a^2 \left(\frac{E_o k_o}{k_c}\right)^2 J_1^2(2.405). \tag{6.15}$$

Equations (6.7) and (6.15) may be used to form an expression for $\frac{R}{Q}$ as a function of $p$ and $\frac{l}{a}$,

$$\begin{aligned} \frac{R}{Q} = \frac{V^2}{\omega U} = \frac{\left(\frac{l}{a}\right)^2}{c\pi k_o l \epsilon_o \left(\frac{k_o}{k_c}\right)^2 J_1^2(2.405)} \Bigg| \operatorname{sinc}\left[\sqrt{\left(\frac{2.405}{2}\right)^2\left(\frac{l}{a}\right)^2 + \left(\frac{p\pi}{2}\right)^2} + \frac{p\pi}{2}\right] + \\ + (-1)^p \operatorname{sinc}\left[\sqrt{\left(\frac{2.405}{2}\right)^2\left(\frac{l}{a}\right)^2 + \left(\frac{p\pi}{2}\right)^2} - \frac{p\pi}{2}\right]\Bigg|^2. \end{aligned} \tag{6.16}$$

### Shunt Impedance

The $\frac{R}{Q}$ of the TM01$p$ mode is generally lower than that of $p+1$ cells of an elliptical multicell cavity, despite having similar electric field patterns. The reduction of the TM01$p$ $\frac{R}{Q}$ is due primarily to transit time effects. It may be expected then that TM01$p$ modes with low $p$ values and correspondingly shorter lengths would possess larger $\frac{R}{Q}$s. This trend can be seen in Figure 6.4. Low values of $p$ are clearly preferable since a large $\frac{R}{Q}$ is desirable.

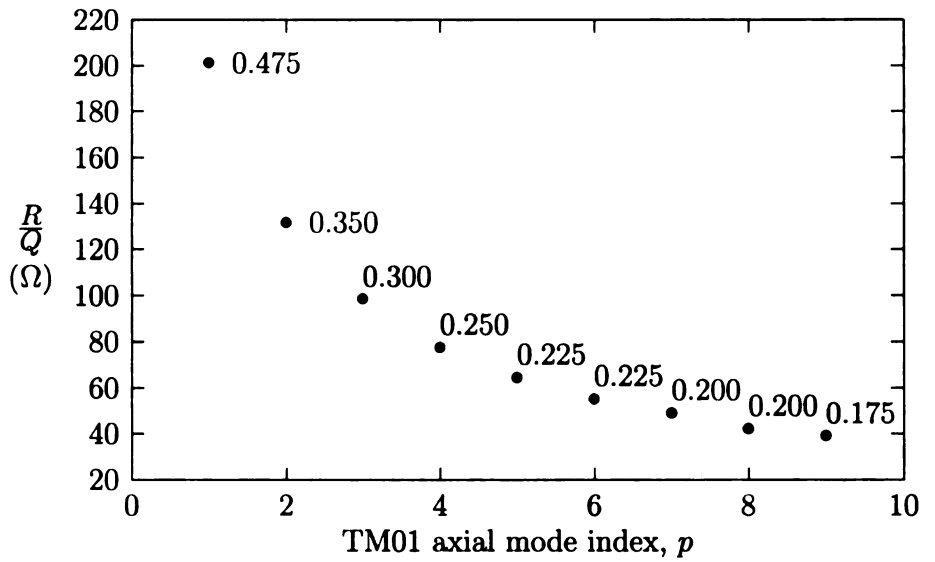


Figure 6.4: The $\frac{R}{Q}$ is seen to decrease with the mode index $p$. The values of $\frac{a}{l}$ which maximizes $\frac{R}{Q}$ are used and printed next to the data point.

### Geometry Factor

Also, Equation (6.15) may be combined with an explicit expression for $\int |H|^2 \mathrm{d}a$ to determine the geometry factor $G$:

$$G = \frac{\omega U}{\frac{1}{2}\int |H|^2 \mathrm{d}a}. \tag{6.17}$$

Using Equation (6.2d),

$$\begin{aligned}
\int |H|^2 \mathrm{d}a &= \int_0^{2\pi}\int_0^{l}\left[\frac{E_0 J_1(2.405)k_0}{\eta k_c}\cos\left(\frac{p\pi z}{l}\right)\right]^2 a\mathrm{d}\phi\mathrm{d}z \\
&\quad +2\int_0^{2\pi}\int_0^{a}\left[\frac{E_0 k_0}{\eta k_c}\right]^2 J_1^2(k_c\rho)\rho\mathrm{d}\phi\mathrm{d}\rho \qquad (6.18)\\
&= \pi l a\left[\frac{E_0 J_1(2.405)k_0}{\eta k_c}\right]^2 + 2\pi a^2\left[\frac{E_0 J_1(2.405)k_0}{\eta k_c}\right]^2. \qquad (6.19)
\end{aligned}$$

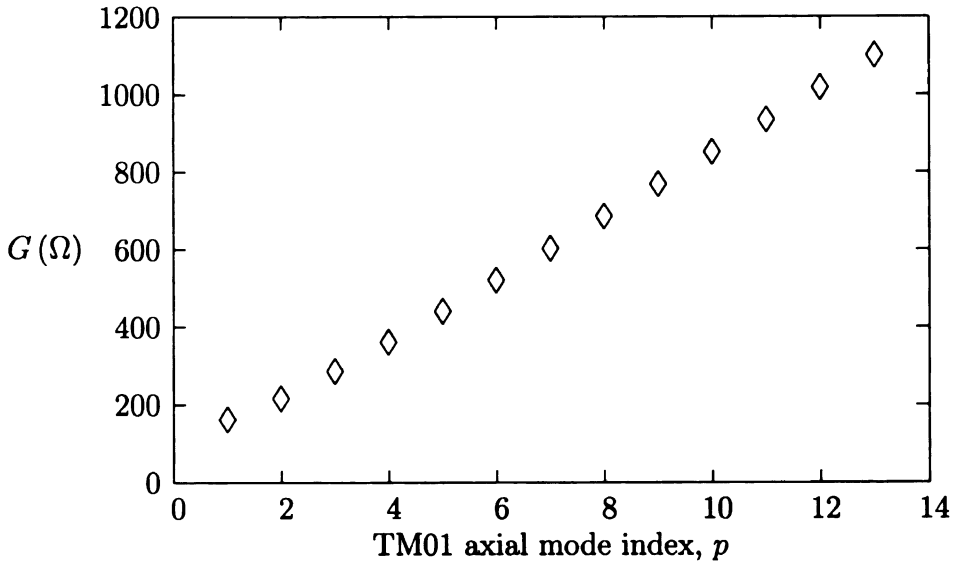


Figure 6.5: The values of $G$ for an ideal pillbox with a length to radius ratio of 5 increase as the axial mode number increases.

Substituting Equations (6.19), (6.15),and (6.10) into Equation (6.17) results in

$$G = \frac{\frac{\eta}{2}\sqrt{\left[2.405\left(\frac{l}{a}\right)\right]^2 + (p\pi)^2}}{2 + \frac{l}{a}}. \tag{6.20}$$

Thus the geometry factor depends on the mode index $p$ and the length to radius ratio. Values of $G$ as a function of $p$ are shown in Figure 6.5 for a fixed $l/a$ ratio.

### Peak Magnetic Field

The ultimate theoretical limit to the gradient of a superconducting cavity is determined by the value of $\frac{B_{\mathrm{p}}}{E_{\mathrm{acc}}}$. For this reason, it is useful to examine how this figure of merit depends on the choice of the mode index and initial pillbox shape. Equation (6.12) determines the value of $\frac{B_{\mathrm{p}}}{E_{\mathrm{acc}}}$ for a given mode in a pillbox as a function of the aspect ratio $\frac{l}{a}$. The equation is evaluated at discrete values of $\frac{l}{a}$ separated by a numerical difference of 0.025. The cell shape which minimizes $\frac{B_{\mathrm{p}}}{E_{\mathrm{acc}}}$ is then recorded for each value of the mode index $p$. The results for the first nine HOMs are shown in Figure 6.6. Low values of $p$ are clearly necessary if the HOM cavity is to have a

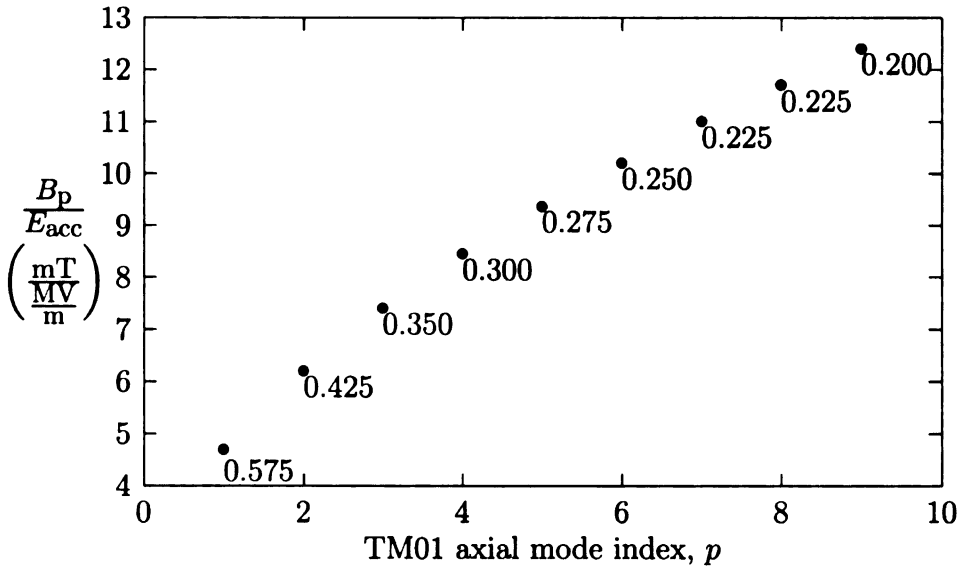


Figure 6.6: The lowest value of $\frac{B_p}{E_{acc}}$ for a TM01$p$ mode is seen to increase with the mode index $p$. The value of $\frac{a}{l}$ which minimizes $\frac{B_p}{E_{acc}}$ is printed next to the data point.

reasonable value of $\frac{B_p}{E_{acc}}$. When comparing the single-cell HOM cavity to a multicell elliptical cavity, the value of $p$ corresponds roughly to the number of cells in a comparable multicell cavity. It should be noted that while $\frac{B_p}{E_{acc}}$ generally increases with $p$ for the HOM cavity, a similar trend of increasing $\frac{B_p}{E_{acc}}$ with larger cell numbers does not occur for multicell cavities. The reason is that frequency $f$ of the accelerating mode of a multicell cavity is determined by adjusting the cell radius and the axial wave number $\beta$ is determined by the cell length. Independent control of these two parameters enables multicell cavities to be designed such that an accelerated charge only experiences forces in the direction of its motion:

$$\frac{\omega}{v} = \frac{\pi}{l_{cell}} \tag{6.21}$$

where $v$ is the particle velocity. As described earlier, independent control over the values of the HOM cavity frequency and $\beta$ is not possible since Equation (6.10) must be satisfied. Equation (6.21) can never be satisfied for the HOM cavity, so the particle

will experience forces in the direction opposite to its motion; the voltage gain, and therefore $E_{\rm acc}$, will be lower; and both $\frac{B_{\rm p}}{E_{\rm acc}}$ and $\frac{E_{\rm p}}{E_{\rm acc}}$ will increase. This effect is worse for higher $p$ since the particle will become less synchronised with the accelerating field as it travels further through the HOM cavity.

### Parasitic Modes

The cartoon in Figure 3.2 illustrates the general situation for multicell cavities in which entire HOM passbands may be below the cutoff frequency for the beam pipe. These parasitic modes would have high $Q$'s if their stored energies were not properly removed with a coupler. This situation would also occur when forming a single-cell HOM cavity with the exception that there are no longer passbands. However, using TM01$p$ ($p > 0$) as the accelerating mode guarantees the existence of lower order modes (LOM) which will also be parasitic. The number of LOMs below TM01$p$ in frequency increases for larger values of $p$. Figure 6.7 shows that the number of parasitic modes increases linearly with the value of the mode index. For a given value of $p$, the cavity

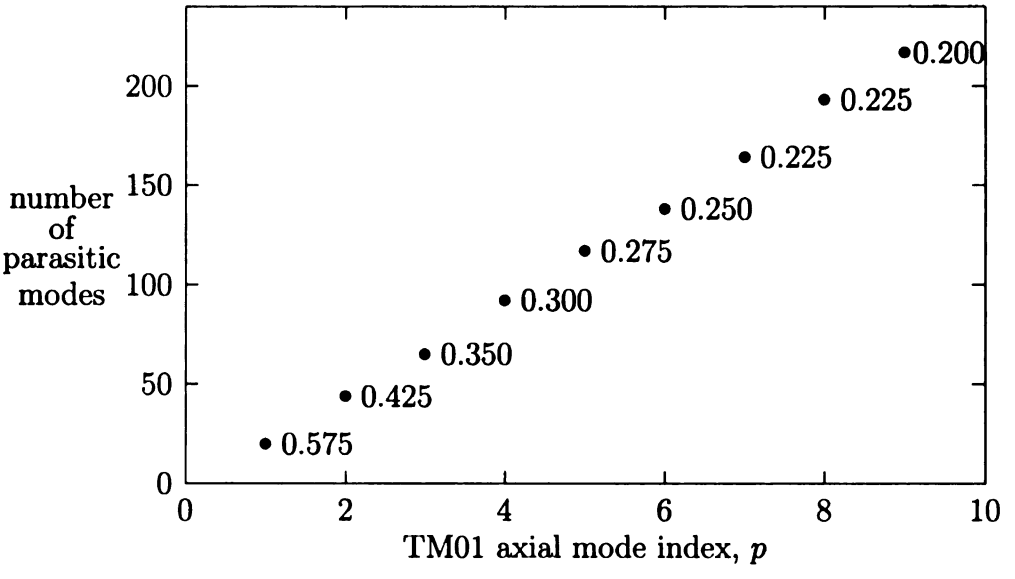


Figure 6.7: The number of parasitic modes is seen to increase with the mode index $p$. The values of $\frac{a}{l}$ which minimize $\frac{B_{\rm p}}{E_{\rm acc}}$ are used and printed next to the data point.

shape which minimizes $\frac{B_p}{E_{acc}}$ was used and the size of the pillbox was determined by setting the frequency of the TM01$p$ mode to 703 MHz. The cutoff frequencies for the waveguide modes were determined by choosing the radius of a hypothetical beam pipe to be 12 cm. A pillbox TM$mnp$ (TE$mnp$) mode is considered parasitic if its frequency is below the cutoff frequency of the TM$m$1 (TE$m$1) beam pipe mode. Since there are an infinite number of field patterns to count, only pillbox modes with $m \leq 2$ and $n \leq 2$ were considered.

The parasitic modes must be sufficiently damped to avoid beam instabilities and excessive cryogenic heat loads. The challenge of damping a large number of parasitic modes increases considerably if a large value of $p$ is chosen for the accelerating mode of the cavity. Low values of $p$ are therefore desirable.

## 6.2 Cavity Design

The analytical results for an ideal pillbox indicate that a single-cell HOM cavity will have higher peak magnetic fields, a lower $\frac{R}{Q}$, and more parasitic modes than a multicell elliptical cavity. A multicell cavity designed for a high-current linac cannot therefore be simply replaced with a single-cell HOM cavity. The high peak magnetic field of the single cell would reduce $E_{acc}$ too much to compete.

However, the single-cell HOM cavity may be suitable for use where high gradients are not necessary, such as in a high-current storage ring. For such an application, the cavity would only need to provide a voltage gain on the order of 1 MV. Since the length of the HOM cavity would be longer than a TM010 single-cell cavity, the required accelerating gradient would be reduced. So, while the ratios $\frac{E_p}{E_{acc}}$ and $\frac{B_p}{E_{acc}}$ are high, the peak fields in the HOM cavity can be small. This can be facilitated by choosing a relatively low value of $p$ for the accelerating mode, which has the additional advantage of limiting the number of parasitic modes to a reasonable level. The $\frac{R}{Q}$ is low, however this does not necessarily imply that the power dissipated by

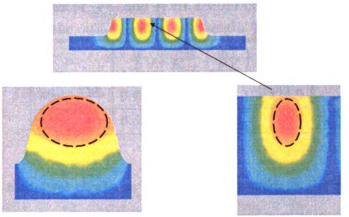

Figure 6.8: The relative magnitudes of the magnetic field for the TM010 and TM013 are shown, as predicted by Analyst, with red corresponding to the largest values and blue corresponding to the lowest.

the accelerating mode will be excessive. This is due to the fact that the geometry factor for a TM01$p$ mode is typically higher than for a multicell cavity. The dynamic power dissipation for the accelerating mode is

$$P = \frac{V^2}{R} = \frac{V^2}{\left(\frac{R}{Q}\right)Q} = \frac{V^2 R_s}{\left(\frac{R}{Q}\right)G}.$$

It is the product $\left(\frac{R}{Q}\right)G$ which therefore determines the dynamic losses. The higher $G$ values for a TM01$p$ mode may be understood by comparing the magnetic field pattern to that of the TM010 mode in a multicell cavity, as shown in Figure 6.8. The high magnetic field region of a multicell cavity is distributed along a significant fraction of the surface, whereas the high magnetic field regions of the TM013 mode are more in the volume of the cavity, with less contact with the surface. Therefore the ratio of stored energy to dissipated power is higher for the TM013 mode. This property of the TM01$p$ modes also explains why $G$ for an ideal pillbox increases with $p$, as can be seen in Figure 6.5.

Table 6.1: The best values of $\frac{B_p}{E_{acc}}$ and $\frac{R}{Q}$ for TM012 occur at different pillbox cavity shapes, measured with the ratio of radius over length $\frac{a}{l}$.

| | $\frac{a}{l}$ | $\frac{B_p}{E_{acc}}\left(\frac{mT}{\frac{MV}{m}}\right)$ | $\frac{R}{Q}(\Omega)$ |
|---|---|---|---|
| Min. $\frac{B_{pk}}{E_{acc}}$ | 0.425 | 6.21 | 114.0 |
| Max. $\frac{R}{Q}$ | 0.350 | 6.68 | 131.8 |

The TM012 mode was chosen as the accelerating mode of the HOM cavity. The iris radius is set equal to that of BNL's "Ampere Class" cavity which is designed for $\geq$100 mA of electron beam current. The "Ampere Class" iris radius is 8.5 cm with an accelerating mode frequency of 703 MHz.

### 6.2.1 Rounding the Corners

The next step is to choose an initial pillbox shape for the TM012 cavity, but it is not entirely apparent which value of $\frac{a}{l}$ to start with. The pillbox shape which minimizes $\frac{B_p}{E_{acc}}$ for the TM012 mode has $\frac{a}{l} = 0.425$ (Figure 6.6), while the pillbox shape which maximizes $\frac{R}{Q}$ has $\frac{a}{l} = 0.350$ (Figure 6.4). The values of these figures of merit are listed in Table 6.1. A further complication is that both figures of merit will change as the corners of the pillbox are rounded. The pillbox shape with $\frac{a}{l} = 0.425$ minimizes $\frac{B_p}{E_{acc}}$. The corners of this pillbox were rounded by adding circular arcs, and the radius of curvature was varied. The values of $\frac{B_p}{E_{acc}}$, $\frac{R}{Q}$, and $G$ for each case are listed in Table 6.2.

The reduction in $\frac{B_p}{E_{acc}}$ which occurs as a function of the radius of curvature may be seen in Figure 6.9. It is seen that the pillbox shape with $\frac{a}{l} = 0.425$ and a radius of curvature at the corners of 10.5 cm has a $\frac{B_p}{E_{acc}}$ which is lower and a $\frac{R}{Q}$ which is higher than any case listed in Table 6.1. Figure 6.10 shows the increase in $\left(\frac{R}{Q}\right)G$ as a function of radius of curvature.

The pillbox shape with $\frac{a}{l} = 0.350$ maximizes $\frac{R}{Q}$. The corners of this pillbox were rounded by adding circular arcs, and the radius of curvature was varied. The values

Table 6.2: Rounding the corners of a pillbox$\left(\frac{a}{l} = 0.425\right)$ decreases the minimum $\frac{B_p}{E_{acc}}$, increases the maximum $\frac{R}{Q}$, and increases $G$ for the TM012 mode. The values are from SUPERFISH simulations. It is worth noting that the results for zero radius of curvature are consistent with the analytically-calculated values in Table 6.1.

| radius of curvature(cm) | $\frac{B_p}{E_{acc}}\left(\frac{\text{mT}}{\frac{\text{MV}}{\text{m}}}\right)$ | $\frac{R}{Q}(\Omega)$ | $G(\Omega)$ |
|---|---|---|---|
| 0 | 6.22 | 113.6 | 365.8 |
| 1.0 | 6.21 | 113.9 | 372.1 |
| 2.0 | 6.18 | 114.8 | 378.9 |
| 3.0 | 6.17 | 116.2 | 385.9 |
| 4.0 | 6.13 | 118.1 | 392.8 |
| 5.0 | 6.12 | 120.3 | 399.7 |
| 6.0 | 6.10 | 122.8 | 406.2 |
| 7.0 | 6.08 | 125.5 | 412.6 |
| 8.0 | 6.07 | 128.3 | 418.7 |
| 9.0 | 6.06 | 130.9 | 424.8 |
| 10.0 | 6.051 | 133.4 | 430.7 |
| 10.5 | 6.049 | 134.5 | 433.6 |
| 11.0 | 6.05 | 135.5 | 436.5 |
| 12.0 | 6.06 | 137.1 | 442.2 |
| 14.0 | 6.14 | 138.0 | 453.7 |
| 16.0 | 6.31 | 135.2 | 465.2 |

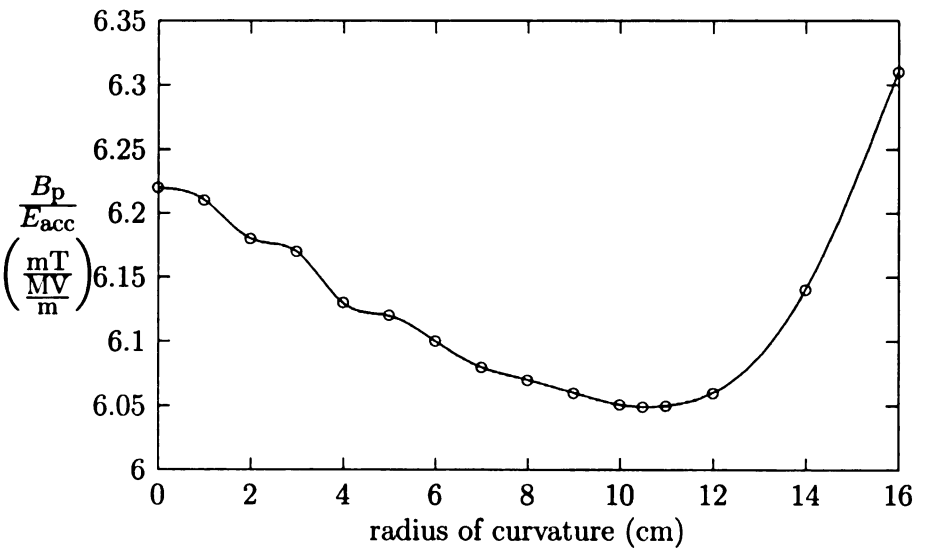


Figure 6.9: The minimum value of $\frac{B_p}{E_{acc}}$ for the TM012 mode of a pillbox $\left(\frac{a}{l} = 0.425\right)$ is seen to occur at a radius of curvature of 10.5 cm.

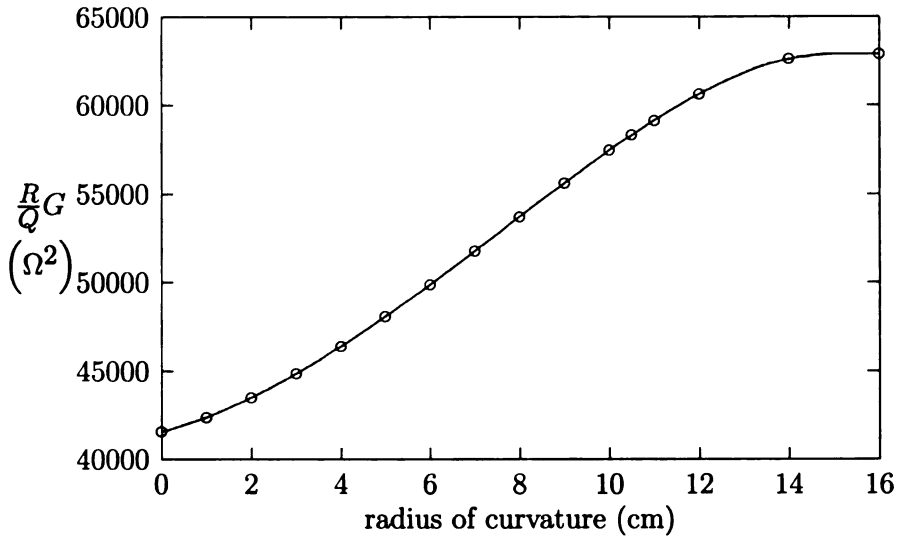


Figure 6.10: $\left(\frac{R}{Q}\right) G$ for the TM012 mode increases with larger radii of curvature at the pillbox $\left(\frac{a}{l} = 0.425\right)$ corners.

of $\frac{B_p}{E_{acc}}, \frac{R}{Q}$, and $G$ for each case are listed in Table 6.3.

Trends similar to the $\frac{a}{l} = 0.425$ case are seen in Figures 6.11 and 6.12, however $\frac{B_p}{E_{acc}}$ does not improve substantially and is still higher than the $6.049 \frac{\text{mT}}{\frac{\text{MV}}{\text{m}}}$ achieved with $\frac{a}{l} = 0.425$. For this reason, the TM012 cavity was chosen to have an initial pillbox shape with $\frac{a}{l} = 0.425$.

### 6.2.2 Adding the Beam Tubes

The ends of the TM012 cavity were next modelled as two ellipses connected by a straight section. The geometrical parameters were varied and the cavity figures of merit were optimized using the same SUPERFISH interface program described in Section 3.2. A plot of the cavity shape with the electric field lines of the TM012 mode is shown in Figure 6.13. Adding beam pipes reduces the accelerating gradient and results in a $\frac{B_p}{E_{acc}}$ which is larger than is shown in Table 6.2 for a radius of curvature of 10.5 cm. It was possible to limit the increase in $\frac{B_p}{E_{acc}}$ by increasing the length of the vertical semi-axis to approximately 19 cm while keeping the horizontal semi-axis

Table 6.3: Rounding the corners of the pillbox $\left(\frac{a}{l} = 0.350\right)$ decreases the minimum $\frac{B_p}{E_{acc}}$, increases the maximum $\frac{R}{Q}$, and increases $G$ for the TM012 mode. The values are from SUPERFISH simulations. It is worth noting that the results for zero radius of curvature are consistent with the analytically calculated values in Table 6.1.

| radius of curvature (cm) | $\frac{B_p}{E_{acc}}\left(\frac{\text{mT}}{\frac{\text{MV}}{\text{m}}}\right)$ | $\frac{R}{Q}(\Omega)$ | $G(\Omega)$ |
|---|---|---|---|
| 0 | 6.68 | 131.7 | 361.0 |
| 1.0 | 6.68 | 131.8 | 367.1 |
| 2.0 | 6.67 | 132.3 | 373.7 |
| 4.0 | 6.66 | 133.9 | 387.1 |
| 8.0 | 6.68 | 135.4 | 413.4 |
| 9.0 | 6.69 | 134.5 | 420.0 |
| 10.0 | 6.74 | 132.7 | 426.8 |

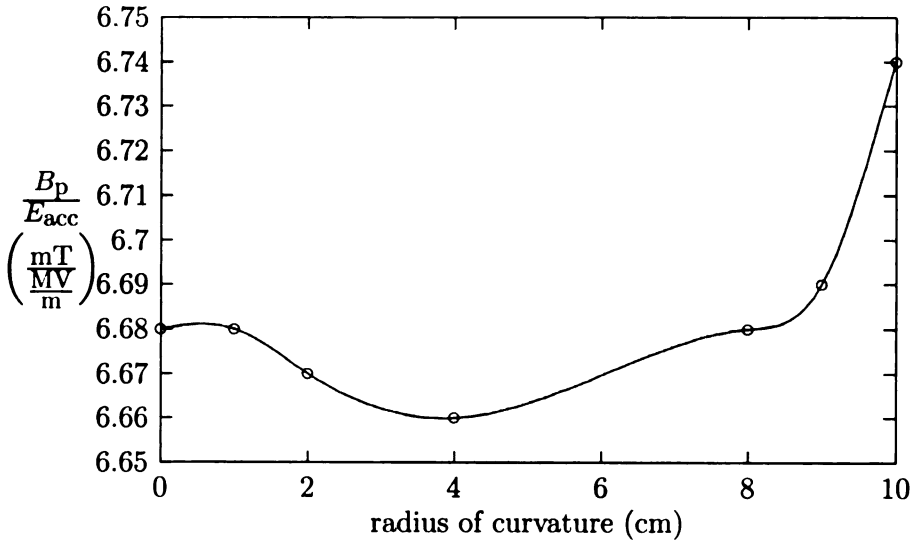


Figure 6.11: The minimum value of $\frac{B_p}{E_{acc}}$ for a pillbox with $\frac{a}{l} = 0.350$ is still much higher than the 6.049 $\frac{\text{mT}}{\frac{\text{MV}}{\text{m}}}$ achieved with $\frac{a}{l} = 0.425$.

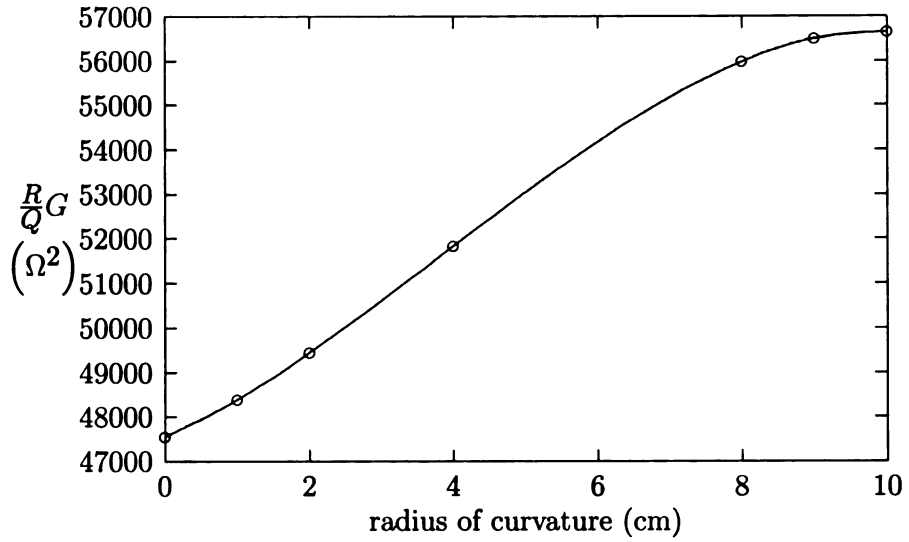


Figure 6.12: $\left(\frac{R}{Q}\right) G$ for the TM012 mode increases with larger radii of curvature at the pillbox $\left(\frac{a}{l} = 0.350\right)$ corners.

length at approximately 10 cm, as shown in Table 6.4. The large $\frac{B_p}{E_{acc}}$ and $\frac{E_p}{E_{acc}}$ values seen in Table 6.4 prevent the TM012 cavity from achieving high accelerating gradients. It therefore would not be suitable for linacs. However, in applications where electron bunches are repeatedly fed back to the same small number of cavities, such as in an electron storage ring, a modest accelerating gradient may be acceptable. Also, the large iris and correspondingly low $k_{||}$ would enable the use of large beam currents.

The magnitude of the axial component of the electric field $E_z$ is plotted in Figure 6.14. There are 2 zeroes of $E_z$ along the axis, therefore the mode is TM012. However, adding beam pipes allows the electric field to leak out and of the cavity, where it decreases exponentially. As a result, the variation of $E_z$ more closely resembles that of 3 cells in a $\pi$-mode structure. The total length of the TM012 cavity from iris to iris is 61.6 cm, which is close to the length of 3 cells in a $\pi$-mode structure with $\frac{3c\pi}{\omega} = 64\,\text{cm}$. Multicell elliptical cavities are normally tuned to have a flat $\pi$-mode: the field magnitude on axis is the same for each cell to within a few percent. In comparison, the TM012 cavity has very unflat fields. This field unflatness is a

Table 6.4: The geometrical parameters and figures of merit for the TM012 cavity are listed, corresponding to a frequency of 703 MHz. The parameters describe the end cell shape as illustrated in Figure 1.2. Note that the definition of $l$ in the table is the axial distance from the beginning of the equatorial ellipse to the end of the iris ellipse. The distance from the middle of the cavity to the beginning of the equatorial ellipse is $l_{\text{straight}}$.

| | | |
|---|---|---|
| $A$ | cm | 9.956 |
| $B$ | cm | 18.916 |
| $h$ | cm | 14.098 |
| $a$ | cm | 2.947 |
| $b$ | cm | 2.947 |
| $z$ | cm | 11.464 |
| $l_{\text{straight}}$ | cm | 13.392 |
| $l$ | cm | 17.415 |
| $d$ | cm | 2.654 |
| $\alpha$ | degrees | 6.0 |
| $r_{\text{iris}}$ | cm | 8.517 |
| $R_{\text{equator}}$ | cm | 33.014 |

| | | |
|---|---|---|
| $\frac{R}{Q}$ | $\Omega$ | 55.0 |
| $\frac{E_{\text{p}}}{E_{\text{acc}}}$ | | 3.06 |
| $\frac{B_{\text{p}}}{E_{\text{acc}}}$ | $\frac{\text{mT}}{\frac{\text{MV}}{\text{m}}}$ | 8.40 |
| $G$ | $\Omega$ | 476 |
| $k_{\parallel}$ | $\frac{\text{V}}{\text{pC}}$ | 0.49 |
| $T$ | | 0.63 |

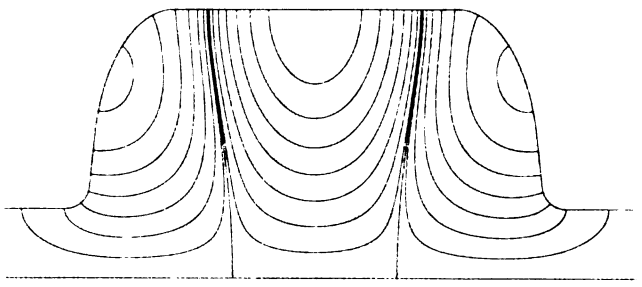

Figure 6.13: The electric field lines for the TM012 mode as predicted from SUPERFISH.

manifestation of the fact that the frequency and cell length of a HOM cavity cannot be varied independently as is possible with multicell ellitical cavities. The distance separating the two zeroes of $E_z$ is greater than $\frac{c\pi}{\omega} = 21.3\,\text{cm}$ and a particle would experience a force opposing its motion, reducing the net voltage gain. For larger $p$, this would be true between all zeroes in $E_z$ in the interior of the cavity. To minimize the reduction of the overall voltage gain by these detuned peaks in $E_z$, the magnitude of the peaks would be smaller in a final optimised shape of a general TM01$p$ mode. Adding beam pipes to the HOM cavity causes $E_z$ to fringe out, resulting in peaks whose length is greater than those in the interior. The ratios $\frac{B_p}{E_{acc}}$ and $\frac{E_p}{E_{acc}}$ depend strongly on the shape of the ends of the TM012 cavity since, as was noted before, the peak fields occur there. It is understandable then that a shape which produces low $\frac{B_p}{E_{acc}}$ and high $\frac{R}{Q}$ is one in which the field intensity is highest in the ends: this is where the proper shape can simultaneously reduce the peak fields and vary the length of the $E_z$ peaks. Figure 6.15 shows the magnitude of the electric and magnetic field that are present on the inner surface of the cavity. The initial point is located at the middle of the cavity on the equator. The path then moves along the inner surface of the cavity and toward the beam pipe.

### 6.2.3 Loss Factor

The total longitudinal loss factor was numerically calculated with the program ABCI [26]. In the ABCI simulation, a charge bunch with a Gaussian profile is sent through the cavity on axis, maintaining a constant velocity $c$. The value of $\sigma$ in the Gaussian profile is 1 cm and the total length of the bunch is 5 $\sigma$. Figure 6.16 shows a picture of the cavity, the charge bunch, and the electric field lines of the wake at six different times. Maxwell's equations are numerically solved and the sum of the forces acting back on the charge bunch gives the loss factor.

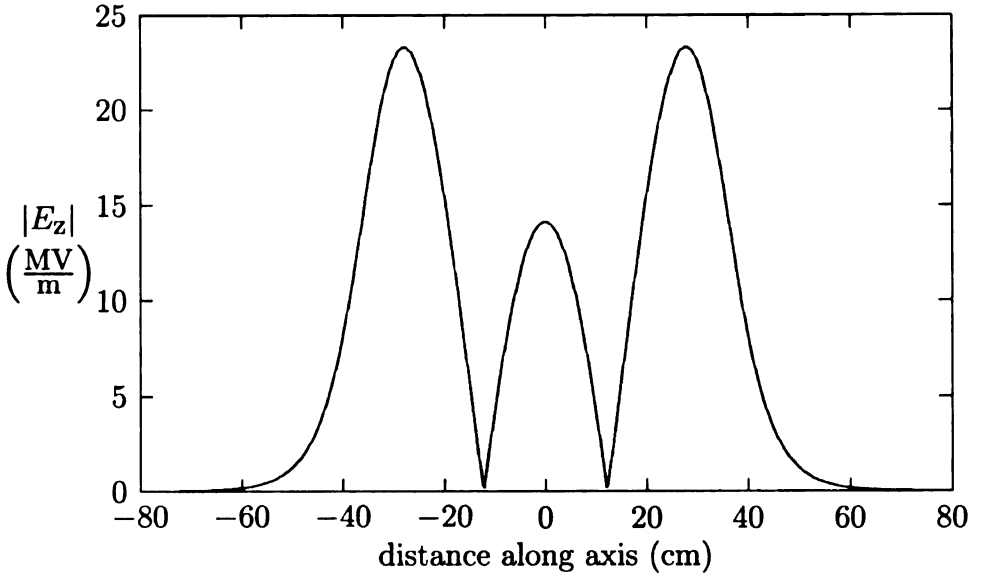


Figure 6.14: A SUPERFISH calculation of the axial electric field magnitude along the beam axis, normalized for an accelerating gradient of $10\frac{MV}{m}$.

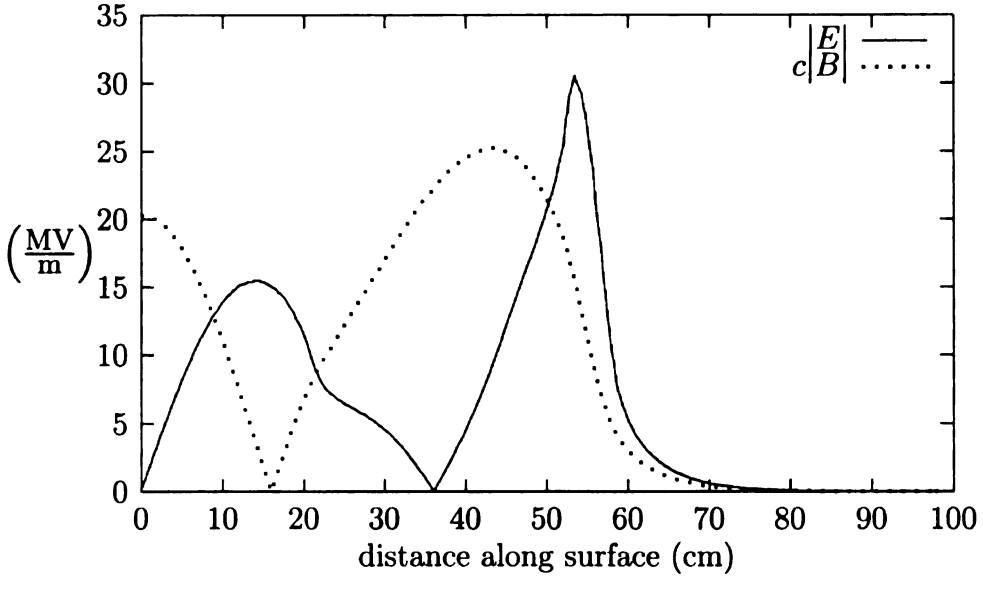


Figure 6.15: The magnitudes of the electric and magnetic fields are plotted as a function of the distance travelled along the surface. The origin is located at the middle of the cavity on the equator, and the path moves along the surface and toward the beam pipe. The values are calculated from SUPERFISH and normalized to an accelerating gradient of $10\frac{MV}{m}$.

Figure 6.16: A charge bunch, which has a Gaussian distribution with $\sigma = 1$ cm, enters the TM012 cavity from the left in the upper left frame and proceeds through the cavity, exiting in the lower right frame. ABCI was used to numerically calculate the wake and the associated longitudinal loss factor.

### 6.2.4 Comparison with SOLEIL Cavity

An example to illustrate the conditions under which the TM012 cavity may be useful is provided by the 353 MHz single-cell niobium-coated copper cavity at SOLEIL [27] which was designed for an average beam current of 500 mA. The TM012 cavity was rescaled to operate at 353 MHz and ABCI was then used to calculate the loss factor for the case of a $\sigma$ =5 mm bunch. The figures of merit for both cavities, as well as peak field levels, assuming both cavities provide the same voltage gain of 2 MV, are shown in Table 6.5. A drawing comparing the two cavity shapes with the correct relative scale is shown in Figure 6.17. The TM012 cavity is huge in comparison. The larger size of the TM012 cavity does not however indicate larger dynamic losses. The geometry factor of the SOLEIL cavity must be 291 $\Omega$ for the product $\left(\frac{R}{Q}\right)G$ to be equal to that of the TM012 cavity. Since elliptical cells typically have values for $G$ between 225 $\Omega$ and 280 $\Omega$, less power is expected to be dissipated in the TM012 cavity accelerating mode. Using the TM012 mode as the accelerating mode allows the size of the cavity to increase without increasing, or actually reducing, the dynamic losses of the accelerating mode. Also, the peak field levels in the TM012 cavity are lower

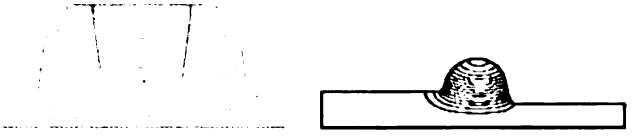

Figure 6.17: The scale of the TM012 cavity drawing on the left is such that the TM012 mode would have the same frequency (353 MHz) as the TM010 mode of the SOLEIL cavity shown on the right.

despite have large values of $\frac{B_\mathrm{p}}{E_\mathrm{acc}}$ and $\frac{E_\mathrm{p}}{E_\mathrm{acc}}$. Because of the additional length of the cavity, the required accelerating gradient is lower and results in lower peak fields.

Table 6.5: The figures of merit for the TM012 cavity and the SOLEIL cavity are compared for the case that the accelerating modes of both cavities have the same frequency (353 MHz) and both are normalized to provide the same voltage gain.

| | SOLEIL | TM012 |
|---|---|---|
| $\frac{E_\mathrm{p}}{E_\mathrm{acc}}$ | 2 | 3.06 |
| $\frac{B_\mathrm{p}}{E_\mathrm{acc}}$ | 4.5 $\frac{\mathrm{mT}}{\frac{\mathrm{MV}}{\mathrm{m}}}$ | 8.40 $\frac{\mathrm{mT}}{\frac{\mathrm{MV}}{\mathrm{m}}}$ |
| $k_\parallel$ | 0.38 $\frac{\mathrm{V}}{\mathrm{pC}}$ | 0.37 $\frac{\mathrm{V}}{\mathrm{pC}}$ |
| $\frac{R}{Q}$ | 90 Ω | 55 Ω |
| $G$ | | 476 Ω |
| Cavity length | 42.5 cm | 122.7 cm |
| Beam pipe radius | 13.0 cm | 17.0 cm |
| Voltage | 2.0 MV | 2.0 MV |
| $E_\mathrm{p}$ | 9.42 $\frac{\mathrm{MV}}{\mathrm{m}}$ | 4.99 $\frac{\mathrm{mT}}{\frac{\mathrm{MV}}{\mathrm{m}}}$ |
| $B_\mathrm{p}$ | 21.2 mT | 13.69 mT |

# Chapter 7

# Conclusion

## 7.1 Summary

Smaller, higher-frequency cavities for accelerating 100's of mA of beam current for an ERL are envisioned with every RF bucket filled. This has the advantages of reducing the bunch charge and simplifying HOM damping by ensuring that all dangerous HOMs are above cutoff. Two elliptical cavity designs for this purpose are presented which provide low peak fields and high cell-to-cell coupling. The beam pipe radius is large enough for any HOM with a frequency at or above twice the accelerating mode frequency to propagate out of the cavity. A single-cell cavity operating in the TM012 mode can provide useful voltage gain and a low loss factor, but the issue of adequate lower-order parasitic mode damping must still be addressed.

Two copies of a 2-cell cavity design for high average beam currents have been fabricated and tested, achieving a maximum accelerating gradient of $8.74\,\frac{\mathrm{MV}}{\mathrm{m}}$. This limiting field might be explained by a superconducting region of the cavity going normal-conducting at high fields. One possible area for the superconducting to normal-conducting transition to have occurred is a Nb disk which was used to shield the stainless steel input flange during vertical testing. It seems as if some soft multipacting barriers were encountered at lower fields such as $4\,\frac{\mathrm{MV}}{\mathrm{m}}$, but it was possible

to work through them and achieve gradients suitable for accelerating 100's of mA of beam current.

## 7.2 Implications

To increase the maximum electron beam current in a storage ring, the cavity iris must be opened to prevent beam breakup and to limit the increase in induced HOM power. Increasing the iris of a single-cell elliptical cavity results in a smaller value of $\frac{R}{Q}$ and ultimately leads to larger dynamic losses. By using a single-cell HOM cavity, a mechanism exist for upgrading a storage ring to higher beam currents without paying more for cryogenics. The iris of the HOM cavity can be much larger than that of an elliptical cell operating in the TM010 mode without increasing the dynamic losses. Additionally, the HOM cavity can also supply the same voltage gain with lower peak fields by operating at a lower accelerating gradient.

The small wall angle of the 2-cell cavity was adequate for draining the chemicals from etching and the ultrapure water from the high pressure rinse. The accelerating gradient achieved in both 2-cell cavities met the design criteria, providing in excess of $5.45\,\frac{\mathrm{MV}}{\mathrm{m}}$, without being limited by field emission or quenching. Any multipacting barriers encountered below $8.74\,\frac{\mathrm{MV}}{\mathrm{m}}$ were soft and processed through.

Benchtop measurements on the 2-cell cavity showed that the $Q_{\mathrm{ext}}$'s possible when coupling to a normal-conducting waveguide which intersects the beam line are $\approx 10^7 - 10^8$. Since this is the same range of values currently used for cavities operating with energy recovery, the large diameter iris of the 6-cell cavity may be of interest to researchers wishing to study the feasibility of using such a coupling scheme.

## 7.3 Possible Future Work

The number of projects which could benefit from the results of this dissertation is only limited by the imagination of the researcher. Some possibilities worthy of exploring include:

### 6-cell Cavity

1. Fabricate and test a prototype cavity.
2. Tuner design and microphonics experiments with a prototype cavity.
3. Experimentally determine the frequencies of the vibrational modes of the cavity-tuner combination and study methods of suppressing microphonics.
4. High-field tests of the cavity with a normal conducting waveguide coupler which intercepts the beam line.
5. HOM coupler or ferrite loaded beam pipe design and construction.
6. Cryomodule design with tuners, power couplers, and HOM couplers/loads.

### 2-Cell Cavity

1. Vertical tests with normal conducting beam pipe extensions.
2. Cold cavity tests with high beam currents.
3. Input coupler design for 50 kW or greater.

### HOM Cavity

1. Design of a coaxial beam tube with ferrite loads or HOM couplers for extracting lower order parasitic modes.
2. Calculate the longitudinal loss factor taking into account the coaxial beam tube.

3. Fabricate and test a prototype cavity.

4. Design an input coupler and tuner for the HOM cavity.

5. Fabricate and test the input coupler, HOM dampers, and tuner.

# Appendix A

# Waveguide Modes

In this appendix, the differential equations will be derived for the modes of propagation in a waveguide of uniform cross-section, starting with Maxwell's equations. The waveguide is assumed to have perfectly conducting walls with the inside under vacuum. The particular case of a waveguide of circular cross-section will be considered. The cutoff frequencies and field distributions for the lowest circular waveguide mode of each type (the TE11 mode and the TM01 mode) will be derived.

The derivations presented in the following section synthesize key elements of the texts by Collin [12], Pozar [13], and Slater [14].

## A.1 Maxwell's Equations

The electric field **E** and magnetic field **B** satisfy Maxwell's equations:

$$\nabla \times \mathbf{E} = -\frac{\partial \mathbf{B}}{\partial t} - \mathbf{M} \tag{A.1a}$$

$$\nabla \times \mathbf{H} = \frac{\partial \mathbf{D}}{\partial t} + \mathbf{J} \tag{A.1b}$$

$$\nabla \cdot \mathbf{D} = \rho \tag{A.1c}$$

$$\nabla \cdot \mathbf{B} = 0. \tag{A.1d}$$

For all cases of interest, the fields will vary harmonically with time, so phasor notation will be used for the electric and magnetic field components, i.e. the amplitude and phase of oscillation of a field component is represented by a single complex number. To obtain the value of any component as a function of time it will be necessary to take the real part of the product of the phasor and $e^{j\omega t}$. For any two components, $A$ and $B$, the relation $\mathrm{Re}\left[\frac{AB^*}{2}\right] = \langle AB \rangle$ holds, where $\langle\ \rangle$ denotes averaging over a period. Differentiation (integration) is performed by multiplying (dividing) the phasor by $j\omega$. In this notation Maxwell's equations become

$$\nabla \times \mathbf{E} = -j\omega\mathbf{B} - \mathbf{M} \tag{A.2a}$$

$$\nabla \times \mathbf{H} = j\omega\mathbf{D} + \mathbf{J} \tag{A.2b}$$

$$\nabla \cdot \mathbf{D} = \rho \tag{A.2c}$$

$$\nabla \cdot \mathbf{B} = 0. \tag{A.2d}$$

The region of interest is the vacuum inside of a waveguide so $\mathbf{J}$, $\mathbf{M}$, and $\rho$ are all zero. Additionally, $\mathbf{D} = \epsilon_o\mathbf{E}$ and $\mathbf{B} = \mu_o\mathbf{H}$, where $\epsilon_o = 8.854 \times 10^{-12}$ F/m and $\mu_o = 4\pi \times 10^{-7}$ H/m. In this case, Maxwell's equations reduce to

$$\nabla \times \mathbf{E} = -j\omega\mu_o\mathbf{H} \tag{A.3a}$$

$$\nabla \times \mathbf{H} = j\omega\epsilon_o\mathbf{E} \tag{A.3b}$$

$$\nabla \cdot \mathbf{E} = 0 \tag{A.3c}$$

$$\nabla \cdot \mathbf{B} = 0. \tag{A.3d}$$

Equations (A.3a) and (A.3b) can be decoupled by taking the curl of both sides of Equation (A.3a) and substituting Equations (A.3b) and (A.3c):

$$\nabla \times (\nabla \times \mathbf{E}) = -\mathrm{j}\omega\mu_o \nabla \times \mathbf{H} \tag{A.4}$$

$$\nabla \times (\nabla \times \mathbf{E}) = \nabla(\nabla \cdot \mathbf{E}) - \nabla^2 \mathbf{E} \tag{A.5}$$

$$-\nabla^2 \mathbf{E} = -\mathrm{j}\omega\mu_o(\mathrm{j}\omega\epsilon_o \mathbf{E}) \tag{A.6}$$

$$\nabla^2 \mathbf{E} + \omega^2 \mu_o \epsilon_o \mathbf{E} = 0 \tag{A.7}$$

Taking the curl of Equation (A.3b) gives a differential equation for $\mathbf{H}$ of the same form:

$$\nabla^2 \mathbf{H} + \omega^2 \mu_o \epsilon_o \mathbf{H} = 0. \tag{A.8}$$

Substituting $k_o \equiv \omega\sqrt{\mu_o \epsilon_o}$ into Equations (A.7) and (A.8) gives

$$\nabla^2 \mathbf{E} + k_o^2 \mathbf{E} = 0 \tag{A.9a}$$

$$\nabla^2 \mathbf{H} + k_o^2 \mathbf{H} = 0. \tag{A.9b}$$

If the shape of the metal boundary is not a function of $z$, a solution for any component of $\mathbf{E}$ or $\mathbf{H}$ can assume the form $\mathrm{e}^{-\mathrm{j}\beta z} f(x, y)$. For this case it is convenient to separate $\mathbf{E}$ and $\mathbf{H}$ into transverse and axial components.

$$\mathbf{E} = \mathbf{E}_t + \mathbf{E}_z$$

$$\mathbf{E} = \mathbf{e}(x, y)\mathrm{e}^{-\mathrm{j}\beta z} + \mathbf{e}_z(x, y)\mathrm{e}^{-\mathrm{j}\beta z}$$

$$\mathbf{H} = \mathbf{H}_t + \mathbf{H}_z$$

$$\mathbf{H} = \mathbf{h}(x, y)\mathrm{e}^{-\mathrm{j}\beta z} + \mathbf{h}_z(x, y)\mathrm{e}^{-\mathrm{j}\beta z}$$

Maxwell's equations can be similarly simplified by writing the del operator in terms of transverse and axial components,

$$\nabla = \nabla_t + \nabla_z = \nabla_t - \mathrm{j}\beta\mathbf{n}_z \tag{A.10}$$

since $\mathbf{n}_z\frac{\partial}{\partial z} = -\mathrm{j}\beta\mathbf{n}_z$. Using this notation, each of Maxwell's equations can now be reduced to a form more amenable to solving and classifying waveguide modes.

**Faraday's Law**

The left-hand side of Equation (A.3a) can be written as

$$\nabla \times \mathbf{E} = (\nabla_t - \mathrm{j}\beta\mathbf{n}_z) \times (\mathbf{e} + \mathbf{e}_z)\,\mathrm{e}^{-\mathrm{j}\beta z} \tag{A.11}$$

and the right-hand side may be written as

$$-\mathrm{j}\omega\mu_o\mathbf{H} = -\mathrm{j}\omega\mu_o(\mathbf{h} + \mathbf{h}_z)\,\mathrm{e}^{\mathrm{j}\beta z}. \tag{A.12}$$

Hence, Equation (A.3a) becomes

$$\nabla_t \times \mathbf{e} - \mathrm{j}\beta\mathbf{n}_z \times \mathbf{e} + \nabla_t \times \mathbf{e}_z - \mathrm{j}\beta\mathbf{n}_z \times \mathbf{e}_z = -\mathrm{j}\omega\mu_o\mathbf{h} - \mathrm{j}\omega\mu_o\mathbf{h}_z \tag{A.13}$$

$$\nabla_t \times \mathbf{e} - \mathrm{j}\beta\mathbf{n}_z \times \mathbf{e} + \nabla_t \times \mathbf{e}_z = -\mathrm{j}\omega\mu_o\mathbf{h} - \mathrm{j}\omega\mu_o\mathbf{h}_z. \tag{A.14}$$

Equating the axial and transverse components of Equation (A.14) gives the two vector equations,

$$\nabla_t \times \mathbf{e} = -\mathrm{j}\omega\mu_o\mathbf{h}_z \tag{A.15a}$$

$$\nabla_t \times \mathbf{e}_z - \mathrm{j}\beta\mathbf{n}_z \times \mathbf{e} = -\mathrm{j}\omega\mu_o\mathbf{h}. \tag{A.15b}$$

The first term on the left of Equation (A.15b) may be rewritten as

$$\nabla_t \times \mathbf{e}_z = \frac{\partial e_z}{\partial y}\mathbf{n}_x - \frac{\partial e_z}{\partial x}\mathbf{n}_y = -\mathbf{n}_z \times \nabla_t e_z. \tag{A.16}$$

Substituting the above relation into Equation (A.15b) gives

$$\mathbf{n}_z \times \nabla_t e_z + \mathrm{j}\beta \mathbf{n}_z \times \mathbf{e} = \mathrm{j}\omega\mu_o \mathbf{h}. \tag{A.17}$$

Equations (A.15a) and (A.17) will be used in the following sections to solve for the field patterns of waveguide modes.

### Ampere/Maxwell Relation

In a similar way, Equation (A.3b) may be separated into two vector equations for the axial and transverse components:

$$\nabla_t \times \mathbf{h} = \mathrm{j}\omega\epsilon_o \mathbf{e}_z \tag{A.18}$$

$$\mathbf{n}_z \times \nabla_t h_z + \mathrm{j}\beta \mathbf{n}_z \times \mathbf{h} = -\mathrm{j}\omega\epsilon_o \mathbf{e}. \tag{A.19}$$

### Divergence of B

The left-hand side of Equation (A.3d) can be expressed in terms of axial and transverse components of **H**:

$$\nabla \cdot \mathbf{B} = \nabla \cdot (\mu_o \mathbf{H}) \tag{A.20}$$

$$\nabla \cdot (\mu_o \mathbf{H}) = (\nabla_t - \mathrm{j}\beta \mathbf{n}_z) \cdot (\mathbf{h} + \mathbf{h}_z)\, \mu_o\, \mathrm{e}^{-\mathrm{j}\beta z} \tag{A.21}$$

Hence, Equation (A.3d) can be written as

$$(\nabla_t \cdot \mathbf{h} - \mathrm{j}\beta h_z)\,\mu_o\,\mathrm{e}^{-\mathrm{j}\beta z} = 0 \tag{A.22}$$

$$\text{or as} \quad \nabla_t \cdot \mathbf{h} = \mathrm{j}\beta h_z. \tag{A.23}$$

**Coulomb's Law**

Expressing Equation (A.3c) in terms of components, we obtain a similar expression in terms of electric field components:

$$\nabla_t \cdot \mathbf{e} = \mathrm{j}\beta e_z \tag{A.24}$$

## A.2 Circular Waveguide Modes

### A.2.1 Transverse Electric Modes

Transverse electric (TE) modes are by definition modes in which there is never any component of the electric field in the axial direction, i.e. $e_z = 0$. Under this condition, the above component forms of Maxwell's equations reduce to

$$\nabla_t \times \mathbf{e} = -\mathrm{j}\omega\mu_o \mathbf{h}_z \tag{A.25a}$$

$$\beta \mathbf{n}_z \times \mathbf{e} = \omega\mu_o \mathbf{h} \tag{A.25b}$$

$$\nabla_t \times \mathbf{h} = 0 \tag{A.25c}$$

$$\mathbf{n}_z \times \nabla_t h_z + \mathrm{j}\beta \mathbf{n}_z \times \mathbf{h} = -\mathrm{j}\omega\epsilon_o \mathbf{e} \tag{A.25d}$$

$$\nabla_t \cdot \mathbf{h} = \mathrm{j}\beta h_z \tag{A.25e}$$

$$\nabla_t \cdot \mathbf{e} = 0 \tag{A.25f}$$

Equation (A.9b) may be written explicitly in terms of axial and transverse components. We write

$$\nabla^2 = \nabla_t^2 - \beta^2 \tag{A.26}$$

$$k_c^2 = k_o^2 - \beta^2 \tag{A.27}$$

so that Equation (A.9b) gives

$$\nabla_t^2 h_z + k_c^2 h_z = 0 \tag{A.28}$$

$$\nabla_t^2 \mathbf{h} + k_c^2 \mathbf{h} = 0. \tag{A.29}$$

The Pythagorean relation between the critical wavenumber $k_c$, the free space wavenumber $k_o$, and the axial wavenumber $\beta$ in Equation (A.27) provides a simple physical interpretation of a waveguide mode. Below a critical frequency, $\omega_c = ck_c$, a mode may only be excited evanescently. The mode can only store energy during one half of an RF cycle before delivering it back to the RF source, similar to the behavior of a lumped capacitor or inductor in low frequency circuits. At $\omega_c$, a standing wave is established in the radial direction. The wave is a superposition of a wave travelling away from the axis and a reflected wave travelling toward the axis. The type of mode and the shape of the waveguide cross section will determine the value of $k_c$ when Equation (A.28) is solved. For frequencies above $\omega_c$, a wave travelling in the axial direction is established with the wavenumber $\beta$. The field pattern can therefore be viewed as the superposition of two travelling waves which propagate in equal but opposite directions slightly off axis and continually reflect off of the walls of the waveguide. The two waves travel with the free-space wavenumber $\mathbf{k_0}$ which has $k_c$ as a transverse component and $\beta$ as an axial component.

The first step in solving for the resulting field pattern is to solve Equation (A.28) for $h_z$. Because $\mathbf{E}$ and $\mathbf{H}$ must not only be solutions of the Helmholz equation but

also must satisfy Maxwell's equations, it can be shown that all of the remaining field components can be determined from $h_z$. Since there is no electric current and no axial displacement current ($e_z = 0$) in the interior of the waveguide, $\nabla_t \times \mathbf{h}$ must then be zero by Equation (A.18). If the transverse curl of a transverse field, **h**, is zero it is possible to write **h** as the gradient of a scalar. Additionally, this scalar must involve $\mathbf{h}_z$ since $\nabla \cdot (\mu_o \mathbf{H})$ must always be zero.

$$\nabla_t \times (\nabla_t \times \mathbf{h}) = \nabla_t (\nabla_t \cdot \mathbf{h}) - \nabla_t^2 \mathbf{h} = 0 \tag{A.30}$$

Substituting Equation (A.25e) and replacing $\nabla_t^2 \mathbf{h}$ with $-k_c^2 \mathbf{h}$ shows that **h** is proportional to the gradient of $h_z$:

$$\mathbf{h} = -\frac{\mathrm{j}\beta}{k_c^2} \nabla_t h_z \tag{A.31}$$

The transverse electric field, **e**, may now be found using Equation (A.25b).

$$\mathbf{n}_z \times (\beta \mathbf{n}_z \times \mathbf{e}) = \mathbf{n}_z \times (\omega \mu_o \mathbf{h}) \tag{A.32}$$

$$-\beta \mathbf{e} = \omega \mu_o \mathbf{n}_z \tag{A.33}$$

$$\mathbf{e} = -\frac{\omega \mu_o}{\beta} \mathbf{n}_z \times \mathbf{h} \tag{A.34}$$

The combination of constants appearing in Equation (A.34) can be conveniently rewritten,

$$\frac{\omega \mu_o}{\beta} = \frac{k_o \mu_o}{\beta \sqrt{\mu_o \epsilon_o}} = \frac{k_o}{\beta} \sqrt{\frac{\mu_o}{\epsilon_o}} = \frac{k_o}{\beta} \eta \tag{A.35}$$

$$Z = \frac{k_o}{\beta} \eta \tag{A.36}$$

$$\mathbf{e} = -Z \mathbf{n}_z \times \mathbf{h} \tag{A.37}$$

where $\eta = \sqrt{\frac{\mu_o}{\epsilon_o}} = 376\,\Omega$ is the intrinsic impedance of free space. It is the ratio of the

magnitudes of the electric and magnetic fields which are perpendicular to each other and therefore responsible, by Poynting's theorem, for the energy flux carried by a plane wave. Since $\beta \leq k_o$ from Equation (A.27), it follows that the wave impedance, $Z$, of a waveguide mode is greater than $\eta$. Additionally, the phase velocity, $\frac{\omega}{\beta}$, of the waveguide mode is always greater than the speed of light, $\frac{\omega}{k_o}$.

The procedure for solving for a particular TE mode of a waveguide is generally:

1. Find $h_z$ and $k_c$ as a solution of $\nabla_t^2 h_z + k_c^2 h_z = 0$ using appropriate boundary conditions for the given waveguide cross section.

2. The free-space wavenumber, mode wavenumber, and wave impedance are calculated using the following relations:

$$\begin{aligned} k_o &= \frac{\omega}{c} \\ \beta &= \sqrt{k_o^2 - k_c^2} \\ Z &= \frac{k_o}{\beta}\eta = \frac{k_o}{\beta}\sqrt{\frac{\mu_o}{\epsilon_o}} \end{aligned}$$

   where $\omega$ is the angular frequency of the mode and $c$ is the speed of light.

3. The transverse magnetic field, $\mathbf{h}$, is then found using the relation $\mathbf{h} = -\frac{\mathrm{j}\beta}{k_c^2}\nabla_t h_z$.

4. The transverse electric field, $\mathbf{e}$, is then found from the relation, $\mathbf{e} = -Z\mathbf{n}_z \times \mathbf{h}$.

5. The mode field pattern can then be expressed as,

$$\begin{aligned} \mathbf{H} &= \pm\mathbf{h}\,\mathrm{e}^{\mp \mathrm{j}\beta z} + \mathbf{h}_z\,\mathrm{e}^{\mp \mathrm{j}\beta z} \\ \mathbf{E} &= \mathbf{e}\,\mathrm{e}^{\mp \mathrm{j}\beta z} \end{aligned}$$

   where a plus sign is used in the exponents if the wave is travelling in the direction of $-z$.

### A.2.2 TE11 Mode

The TE11 mode for a waveguide with a circular cross section will be used to demonstrate the procedure described above; The final results will be useful in later sections. First, the eigenvalue equation $\nabla_t^2 h_z + k_c^2 hz = 0$ must be solved. Cylindrical coordinates will be used since the waveguide has a circular cross section:

$$\frac{\partial^2 h_z}{\partial \rho^2} + \frac{1}{\rho}\frac{\partial h_z}{\partial \rho} + \frac{1}{\rho^2}\frac{\partial^2 h_z}{\partial \phi^2} + k_c^2 h_z = 0 \tag{A.38}$$

This equation may be solved using the technique of separation of variables assuming a solution of the form $h_z = R(\rho) F(\phi)$. Substituting this solution into Equation (A.38) and dividing by $h_z$ results in

$$\frac{1}{R}\frac{d^2 R}{d\rho^2} + \frac{1}{\rho R}\frac{dR}{d\rho} + \frac{1}{\rho^2 F}\frac{d^2 F}{d\phi^2} + k_c^2 = 0 \tag{A.39}$$

This equation may be separated into a part which only depends on $\rho$ and a part which only depends on $\phi$:

$$\frac{\rho^2}{R}\frac{d^2 R}{d\rho^2} + \frac{\rho}{R}\frac{dR}{d\rho} + \rho^2 k_c^2 = -\frac{1}{F}\frac{d^2 F}{d\phi^2} \tag{A.40}$$

The only way this equation can be true for any arbitrary values of $\rho$ and $\phi$ is if both sides are equal to the same constant $\nu^2$. The two ordinary differential equations which result are

$$\frac{d^2 R}{d\rho^2} + \frac{1}{\rho}\frac{dR}{d\rho} + \left(k_c^2 - \frac{\nu^2}{\rho^2}\right) R = 0 \tag{A.41}$$

$$\frac{d^2 F}{d\phi^2} + \nu^2 F = 0. \tag{A.42}$$

The general solution of Equation (A.42) is periodic and has the form

$$F(\phi) = A\cos(\nu\phi) + B\sin(\nu\phi). \tag{A.43}$$

To insure that $F$ remains single-valued for values of $\phi$ larger than $2\pi$, $\nu$ must be an integer, $n$. Equation (A.41) is a form of Bessel's equation. A solution which remains finite for all values of $\rho$ is Bessel's function of the first kind $J_n(k_c\rho)$ of order $n$. The general solution then has the form

$$h_z = [A\cos(n\phi) + B\sin(n\phi)]J_n(k_c\rho). \tag{A.44}$$

The condition that must be satisfied at $\rho = a$, the metal boundary, is that the tangential component of the electric field is zero. According to Equations (A.31) and (A.37), this implies that $\frac{\partial h_z}{\partial \rho} = 0$ at $\rho = a$. The only allowed values of $k_c a$ are therefore the roots of $\frac{dJ_n}{d\rho} = 0$. The general solution for a mode is specified completely by two integers, $n$ and $m$. Modes for which $n = 0$ are called monopole; $n = 1$ are dipole; $n = 2$ are quadrupole, etc. The value of $m$ determines which zero of $\frac{dJ_n}{d\rho}$ is used and therefore also determines the value of $k_c$. The lowest frequency TE mode is a dipole ($n = 1$) and corresponds to the first zero ($m = 1$) of $\frac{dJ_n}{d\rho}$. The zero occurs approximately at $k_c a = 1.841$, therefore $k_c = \frac{1.841}{a}$. The solution for $h_z$ in the TE11 mode is then,

$$h_z = [A\cos(\phi) + B\sin(\phi)]\, J_1\left(1.841\frac{\rho}{a}\right). \tag{A.45}$$

Next, $\mathbf{h}$ is determined by evaluating $\mathbf{h} = -\frac{\mathrm{j}\beta}{k_c^2}\nabla_t h_z$ with Equation (A.45) substituted in,

$$\mathbf{h} = -\frac{\mathrm{j}\beta}{k_c^2}\left(\frac{\partial h_z}{\partial \rho}\mathbf{n}_\rho + \frac{1}{\rho}\frac{\partial h_z}{\partial \phi}\mathbf{n}_\phi\right) \tag{A.46}$$

$$\mathbf{h} = -\frac{\mathrm{j}\beta}{k_c^2\rho}[B\cos(\phi) - A\sin(\phi)]\, J_1(k_c\rho)\,\mathbf{n}_\phi - \frac{\mathrm{j}\beta}{k_c}[A\cos(\phi) + B\sin(\phi)]\, J_1'(k_c\rho)\,\mathbf{n}_\rho \tag{A.47}$$

where $J_1'(\rho) = \frac{dJ_1(\rho)}{d\rho}$. Finally, $\mathbf{e}$ is determined by evaluating Equation (A.37):

$$\mathbf{e} = \frac{\mathrm{j}\eta k_o}{k_c}\left[A\cos(\phi) + B\sin(\phi)\right] J_1'\left(k_c\rho\right)\mathbf{n}_\phi - \frac{\mathrm{j}\eta k_o}{k_c^2\rho}\left[B\cos(\phi) - A\sin(\phi)\right] J_1\left(k_c\rho\right)\mathbf{n}_\rho \tag{A.48}$$

where $Z = \frac{k_o}{\beta}\eta$ has been used.

### A.2.3 Transverse Magnetic Modes

Transverse magnetic (TM) modes are by definition modes in which there is never any component of the magnetic field in the axial direction, i.e. $h_z = 0$. The derivation of TM mode field patterns is essentially identical to the previous case for TE modes with **E** and **H** interchanged. The final procedure for solving for TM modes is

1. Find $e_z$ and $k_c$ as a solution of $\nabla_t^2 e_z + k_c^2 e_z = 0$ using appropriate boundary conditions for the given waveguide cross section.

2. The free-space wavenumber, mode wavenumber, and mode impedance are calculated using the following relations:

$$\begin{aligned} k_o &= \frac{\omega}{c} \\ \beta &= \sqrt{k_o^2 - k_c^2} \\ Z &= \frac{\beta}{k_o}\eta = \frac{\beta}{k_o}\sqrt{\frac{\mu_o}{\epsilon_o}} \end{aligned}$$

   where $\omega$ is the angular frequency of the mode and $c$ is the speed of light.

3. The transverse electric field, $\mathbf{e}$, is then found using the relation $\mathbf{e} = -\frac{j\beta}{k_c^2}\nabla_t e_z$.

4. The transverse magnetic field, $\mathbf{h}$, is then found from the relation, $\mathbf{h} = \frac{1}{Z}\mathbf{n}_z \times \mathbf{e}$.

5. The mode field pattern can then be expressed as

$$\begin{aligned} \mathbf{E} &= \mathbf{e}\, e^{\mp j\beta z} + \pm \mathbf{e}_z\, e^{\mp j\beta z} \\ \mathbf{H} &= \pm \mathbf{h}\, e^{\mp j\beta z} \end{aligned}$$

where a plus sign is used in the exponents if the wave is travelling in the direction of $-z$.

### A.2.4 TM01 Mode

The TM01 mode for a waveguide with a circular cross section will be used to demonstrate the procedure described above. The final results will be useful in later sections for describing cavity modes. First, the eigenvalue equation $\nabla_t^2 e_z + k_c^2 ez = 0$ must be solved. The general solution has the form

$$e_z = [A\cos(n\phi) + B\sin(n\phi)]J_n(k_c\rho)\,. \tag{A.49}$$

The condition that must be satisfied at $\rho = a$, the metal boundary, is that $e_z = 0$. The only allowed values of $k_c a$ are therefore the zeros of $J_n$. The general solution for a mode is specified completely by two integers, $n$ and $m$. The value of $m$ determines which zero of $J_n$ is used and therefore also determines the value of $k_c$. The lowest frequency TM mode is a monopole ($n = 0$) and corresponds to the first zero ($m = 1$) of $J_0$. The zero occurs approximately at $k_c a = 2.405$, therefore $k_c = \frac{2.405}{a}$. The solution for $e_z$ in the TM01 mode is then

$$e_z = J_0\left(2.405\frac{\rho}{a}\right). \tag{A.50}$$

Next, $\mathbf{e}$ is determined by evaluating $\mathbf{e} = -\frac{\mathrm{j}\beta}{k_c^2}\nabla_t e_z$ with Equation (A.50) substituted in,

$$\mathbf{e} = e_\rho \mathbf{n}_\rho = -\frac{\mathrm{j}\beta}{k_c^2}\frac{de_z}{d\rho}\mathbf{n}_\rho = -\frac{\mathrm{j}\beta}{k_c^2}k_c J_1(k_c\rho)\,\mathbf{n}_\rho = -\frac{\mathrm{j}\beta}{k_c}J_1(k_c\rho)\,\mathbf{n}_\rho \tag{A.51}$$

where the relation $\frac{dJ_0(\rho)}{d\rho} = J_1(\rho)$ has been used. Finally, $\mathbf{h}$ is determined by evaluating $\mathbf{h} = \frac{1}{Z}\mathbf{n}_z \times \mathbf{e}$ with Equation (A.51) substituted in,

$$\mathbf{h} = h_\phi \mathbf{n}_\phi = -\frac{\mathrm{j}\,k_o}{\eta k_c}J_1(k_c\rho)\,\mathbf{n}_\phi \tag{A.52}$$

where $Z = \frac{\beta}{k_o}Z_o$ has been used.

# Appendix B

# General Expansion of Electromagnetic Fields in a Cavity

In this appendix, the electromagnetic field inside a cavity will be expressed in terms of an orthonormal set of modes. The time evolution of the field in the cavity will then be expressed in terms of scalar differential equations describing the time evolution of the field amplitude of each mode. The differential equations will allow for the possibility of electromagnetic energy being transferred into the mode or out of the mode due to a beam travelling through the cavity, power being supplied or lost through coupling ports, or power dissipation in the walls of the cavity. The derivations in this appendix follow closely the analysis originally done by Slater [14].

## B.1 The Complete Orthogonal Set

In order to characterize the electromagnetic performance of a cavity and to describe a cavity's interaction with a beam of charged particles passing through it, it is convenient to write any electric or magnetic field which exists in the cavity as a sum over a complete set of modes. This complete set of modes will satisfy boundary conditions appropriate for a cavity with no dissipative losses. While this physical situation never

occurs in reality, it is a good approximation for a cavity with low losses, and loss-free boundary conditions are easier for numerical calculation of the modes.

### B.1.1 The Solenoidal Fields

For the closed cavities of interest, any vector field is determined uniquely once the values of its divergence and curl are known at all points. The vector field may therefore be written as the sum of two parts: a solenoidal function with zero divergence and an irrotational function with zero curl. In principle then, a single complete set of solenoidal functions and another complete set of irrotational functions is all that is needed to completely describe either the electric or the magnetic field in a cavity. In practice however, it is convenient to establish two sets of solenoidal functions, $\mathbf{E_a}$ and $\mathbf{H_a}$. The reason for this is due to the electric field and magnetic field in a cavity satisfying different boundary conditions; On a perfect conducting surface, there is no tangential component of the electric field, while for the magnetic field there is no component normal to the surface. A complete set of functions which have no tangential component along the cavity surface could, for example, be used to express the magnetic field at all points *inside* of the cavity. While none of the vector functions in the set satisfy the correct boundary conditions for the magnetic field pattern of interest, an infinite series of these functions may still duplicate the magnetic field pattern arbitrarily close to the surface: The resulting infinite series would duplicate the magnetic field pattern inside of the cavity and would differ only in that the value of its tangential component would discontinuously drop to zero at the surface. To avoid this complexity, two sets of solenoidal functions satisfying two different boundary conditions are used. In this case, the electric and magnetic field pattern of an actual cavity mode may be represented primarily by one mode of each set with small corrections to account for small energy losses. The $\mathbf{E_a}$'s and the $\mathbf{H_a}$'s each form a set which may be used to describe any vector field, however the convergence will be much better if the $\mathbf{E_a}$'s are used to describe the electric field

and the $\mathbf{H_a}$'s are used to describe a magnetic field. Since, according to Maxwell's equations, the curl of the electric field is proportional to the value of the magnetic field and vise versa, the $\mathbf{E_a}$'s and $\mathbf{H_a}$'s will be defined such that the curl of one field is proportional to the value of the other. We will assume that the solenoidal fields satisfy the relations

$$\nabla \times \mathbf{E_a} = k_a \mathbf{H_a} \tag{B.1}$$

$$\nabla \times \mathbf{H_a} = k_a \mathbf{E_a} \tag{B.2}$$

The boundary conditions satisfied by the solenoidal functions will depend on the system of interest but the bounding surface will generally satisfy two types of conditions which are easily implemented in numerical models. Part of the surface, denoted by $S$, will have $\mathbf{n} \times \mathbf{E_a} = 0$ at all points on $S$ while the remaining portion of the surface, denoted by $S'$, will have $\mathbf{n} \times \mathbf{H_a} = 0$ at all points on $S'$. The unit vector normal to the surface is $\mathbf{n}$. The significant feature for both boundary conditions is that all components of $\mathbf{E_a} \times \mathbf{H_a}$ must be tangential to the surface since either $\mathbf{H_a}$ or $\mathbf{E_a}$ is normal to the surface. When the $\mathbf{E_a}$ and $\mathbf{H_a}$ correspond to the electric and magnetic fields of a cavity mode, this means that no energy is transferred through the bounding surface. In addition, it may be shown that $\mathbf{E_a}$ may have normal components only on $S$ and $\mathbf{H_a}$ may have normal components only on $S'$. For example, $\mathbf{H_a}$ must be normal to the surface $S'$ so integrating over a small region of $S'$ gives

$$\int_{S'} (\nabla \times \mathbf{H_a}) \cdot \mathbf{da} = \oint_{S'} \mathbf{H_a} \cdot \mathbf{ds} = 0. \tag{B.3}$$

But since the area of integration can be made arbitrarily small, $\mathbf{E_a}$ must then be tangential to $S'$ from Equation (B.2):

$$0 = \int_{S'} (\nabla \times \mathbf{H_a}) \cdot \mathbf{da} = k_a \int_{S'} \mathbf{E_a} \cdot \mathbf{da}. \tag{B.4}$$

Using the same argument for $S$ shows that $\mathbf{H_a}$ must be tangential to $S$ since $\mathbf{E_a}$ is normal to $S$.

The differential equation that the solenoidal functions satisfy may be found by taking the curl of Equations (B.1) and (B.2). Starting with Equation (B.1) we obtain

$$\nabla \times (\nabla \times \mathbf{E_a}) = \nabla (\nabla \cdot \mathbf{E_a}) - \nabla^2 \mathbf{E_a} \tag{B.5}$$

$$\nabla \times (\nabla \times \mathbf{E_a}) = \nabla \times (k_a \mathbf{H_a}) = k_a^2 \mathbf{E_a}. \tag{B.6}$$

This gives

$$\nabla^2 \mathbf{E_a} + k_a^2 \mathbf{E_a} = 0. \tag{B.7}$$

The same operations on Equation (B.2) results in

$$\nabla^2 \mathbf{H_a} + k_a^2 \mathbf{H_a} = 0. \tag{B.8}$$

Equations (B.7) and (B.8) have the same form as Equations (A.9a) and (A.9b). The orthogonality of the solenoidal functions may be proven by first forming

$$\nabla \cdot [\mathbf{E_b} \times (\nabla \times \mathbf{E_a})] = (\nabla \times \mathbf{E_a}) \cdot (\nabla \times \mathbf{E_b}) - \mathbf{E_b} \cdot [\nabla \times (\nabla \times \mathbf{E_a})] \tag{B.9}$$

$$\nabla \cdot [\mathbf{E_a} \times (\nabla \times \mathbf{E_b})] = (\nabla \times \mathbf{E_b}) \cdot (\nabla \times \mathbf{E_a}) - \mathbf{E_a} \cdot [\nabla \times (\nabla \times \mathbf{E_b})]. \tag{B.10}$$

Equation (B.10) is then subtracted from Equation (B.9); The right-hand side may be simplified:

$$\mathbf{E_a} \cdot [\nabla \times (\nabla \times \mathbf{E_b})] - \mathbf{E_b} \cdot [\nabla \times (\nabla \times \mathbf{E_a})] = (\mathbf{E_a} \cdot \mathbf{E_b}) \left(k_b^2 - k_a^2\right). \tag{B.11}$$

and the Divergence Theorem is used to evaluate the left-hand side,

$$\int \nabla \cdot [\mathbf{E_b} \times (\nabla \times \mathbf{E_a})] d\tau = k_a \oint (\mathbf{E_b} \times \mathbf{H_a}) \cdot d\mathbf{a} = 0 \tag{B.12}$$

and

$$\int \nabla \cdot [\mathbf{E_a} \times (\nabla \times \mathbf{E_b})] d\tau = k_b \oint (\mathbf{E_a} \times \mathbf{H_b}) \cdot d\mathbf{a} = 0, \tag{B.13}$$

so that

$$\left(k_a^2 - k_b^2\right) \int (\mathbf{E_a} \cdot \mathbf{E_b})\, d\tau = 0. \tag{B.14}$$

If $a = b$ then $k_a = k_b$ and $\int (\mathbf{E_a} \cdot \mathbf{E_b})\, d\tau$ may have a nonzero value. If $a \neq b$ then $k_a \neq k_b$ and $\int (\mathbf{E_a} \cdot \mathbf{E_b})\, d\tau$ must be zero and the modes are orthogonal. This argument only works if the functions are nondegenerate, however it can be shown that the orthogonality still holds in the case of degeneracies once the degenerate functions are combined in appropriate linear combinations. Since the case of degeneracies is not of particular interest here, the derivation will not be done and it will be assumed for the remainder of the text that the proper linear combinations have been made such that all solenoidal functions are mutually orthogonal.

For complicated geometries, the $\mathbf{E_a}$'s and $\mathbf{H_a}$'s are found numerically using programs such as SUPERFISH [18] or Analyst [20]. The numerical solution is generally given in terms of properly dimensioned electric and magnetic vector fields for the cavity modes. The electric field $\widetilde{\mathbf{E_a}}$ and the magnetic field $\widetilde{\mathbf{H_a}}$ can be integrated over the volume of the cavity to obtain the total energy $U_a$ stored in the cavity mode:

$$\frac{\epsilon}{2} \int \widetilde{E_a^2} d\tau = \frac{\mu}{2} \int \widetilde{H_a^2} d\tau = U_a. \tag{B.15}$$

Since we wish to normalize the $\mathbf{E_a}$'s so that $\int E_a^2 d\tau = 1$ then the relation between the $\widetilde{\mathbf{E_a}}$'s, which are found from simulations and have units of $\frac{\mathrm{V}}{\mathrm{m}}$, and the $\mathbf{E_a}$'s must be

$$\mathbf{E_a} = \sqrt{\frac{\epsilon}{2U_a}} \widetilde{\mathbf{E_a}}. \tag{B.16}$$

The units of $\mathbf{E_a}$ must then be $\mathrm{m}^{-\frac{3}{2}}$. Additionally, $\int E_a^2 d\tau = 1$ implies that $\int H_a^2 d\tau = 1$

since

$$\begin{aligned}
\nabla \cdot [\mathbf{E_a} \times (\nabla \times \mathbf{E_a})] &= \mathbf{E_a} \cdot [\nabla \times (\nabla \times \mathbf{E_a})] - (\nabla \times \mathbf{E_a}) \cdot (\nabla \times \mathbf{E_a}) \\
&= k_a^2 \left(E_a^2 - H_a^2\right) \qquad \text{(B.17)} \\
k_a^2 \int \left(E_a^2 - H_a^2\right) \mathrm{d}\tau &= \int \nabla \cdot [\mathbf{E_a} \times (\nabla \times \mathbf{E_a})] \mathrm{d}\tau \\
&= k_a \oint (\mathbf{E_a} \times \mathbf{H_a}) \cdot \mathrm{da} = 0 \qquad \text{(B.18)} \\
\Rightarrow \int H_a^2 \mathrm{d}\tau &= \int E_a^2 \mathrm{d}\tau. \qquad \text{(B.19)}
\end{aligned}$$

The relation between the $\mathbf{H_a}$'s and the $\widetilde{\mathbf{H_a}}$'s, which have units of $\frac{\mathrm{A}}{\mathrm{m}}$, must then be

$$\mathbf{H_a} = \sqrt{\frac{\mu}{2U_a}} \widetilde{\mathbf{H_a}}, \qquad \text{(B.20)}$$

and the units of $\mathbf{H_a}$ are $\mathrm{m}^{-\frac{3}{2}}$.

### B.1.2 The Irrotational Fields

Since $\nabla \times \mathbf{F_a} = 0$, $\mathbf{F_a}$ is equal to the gradient of a scalar function,

$$\kappa_a \mathbf{F_a} = \nabla \psi_a. \qquad \text{(B.21)}$$

Also, assume that $\psi_a$ satisfies the differential equation

$$\begin{aligned}
\nabla^2 \psi_a + \kappa_a^2 \psi_a &= 0, \qquad \text{(B.22)} \\
\Rightarrow 0 &= \nabla \left(\nabla^2 \psi_a\right) + \kappa_a^2 \nabla \psi_a = \nabla_a^2 \mathbf{F_a} + \kappa_a^2 \mathbf{F_a}. \qquad \text{(B.23)}
\end{aligned}$$

Both $\mathbf{F_a}$ and $\psi_a$ satisfy the same differential equation, where $\kappa_a \neq k_a$ in general. The boundary conditions satisfied are $\psi_a = 0$ and $\nabla \times \mathbf{F_a} = 0$ at all points on the bounding surface. The orthogonality of the $\psi_a$'s and $\mathbf{F_a}$'s may be proven. First, note

that

$$\nabla \cdot (\psi_{\mathrm{a}} \nabla \psi_{\mathrm{b}}) = \psi_{\mathrm{a}} \nabla^2 \psi_{\mathrm{b}} + (\nabla \psi_{\mathrm{a}}) \cdot (\nabla \psi_{\mathrm{b}}) = -\kappa_b^2 \psi_{\mathrm{a}} \psi_{\mathrm{b}} + (\nabla \psi_{\mathrm{a}}) \cdot (\nabla \psi_{\mathrm{b}}) \quad \text{(B.24)}$$

and

$$\nabla \cdot (\psi_{\mathrm{b}} \nabla \psi_{\mathrm{a}}) = \psi_{\mathrm{b}} \nabla^2 \psi_{\mathrm{a}} + (\nabla \psi_{\mathrm{b}}) \cdot (\nabla \psi_{\mathrm{a}}) = -\kappa_a^2 \psi_{\mathrm{b}} \psi_{\mathrm{a}} + (\nabla \psi_{\mathrm{b}}) \cdot (\nabla \psi_{\mathrm{a}}) . \quad \text{(B.25)}$$

Subtracting Equation (B.25) from (B.24) and integrating over the entire volume results in

$$\int [\nabla \cdot (\psi_{\mathrm{a}} \nabla \psi_{\mathrm{b}}) - \nabla \cdot (\psi_{\mathrm{b}} \nabla \psi_{\mathrm{a}})] \mathrm{d}\tau = \int \psi_{\mathrm{a}} \psi_{\mathrm{b}} \left( \kappa_a^2 - \kappa_b^2 \right) \mathrm{d}\tau. \quad \text{(B.26)}$$

The left side may be converted to an integration over the surface,

$$\oint (\psi_{\mathrm{a}} \nabla \psi_{\mathrm{b}} - \psi_{\mathrm{b}} \nabla \psi_{\mathrm{a}}) \cdot d\mathbf{a} = \left( \kappa_a^2 - \kappa_b^2 \right) \int \psi_{\mathrm{a}} \psi_{\mathrm{b}} \mathrm{d}\tau. \quad \text{(B.27)}$$

The surface integral is zero since the values of both $\psi_{\mathrm{a}}$ and $\psi_{\mathrm{b}}$ are zero for all points on the surface. Hence

$$\left( \kappa_{\mathrm{a}}^2 - \kappa_{\mathrm{b}}^2 \right) \int \psi_{\mathrm{a}} \psi_{\mathrm{b}} \mathrm{d}\tau = 0. \quad \text{(B.28)}$$

If $\kappa_{\mathrm{a}} \neq \kappa_{\mathrm{b}}$, then $\int \psi_{\mathrm{a}} \psi_{\mathrm{b}} \mathrm{d}\tau = 0$ and the functions are orthogonal. Otherwise, $\kappa_{\mathrm{a}} = \kappa_{\mathrm{b}}$ and $\int \psi_{\mathrm{a}} \psi_{\mathrm{b}} \mathrm{d}\tau$ is finite. The $\psi_{\mathrm{a}}$'s are normalized by setting $\int \psi_{\mathrm{a}}^2 \mathrm{d}\tau = 1$.

The orthonormality of the $\psi_{\mathrm{a}}$'s implies that the $\mathbf{F}_{\mathrm{a}}$'s are also orthonormal. To see this, first note that

$$\int \nabla \cdot (\psi_{\mathrm{a}} \nabla \psi_{\mathrm{b}}) \, \mathrm{d}\tau = \oint \psi_{\mathrm{a}} \, (\nabla \psi_{\mathrm{b}}) \cdot \mathrm{d}\mathbf{a} = 0. \quad \text{(B.29)}$$

But the volume integral on the left may also be written as

$$\int (\nabla\psi_{\mathrm{a}}) \cdot (\nabla\psi_{\mathrm{b}})\, \mathrm{d}\tau + \int \psi_{\mathrm{a}} \nabla^2 \psi_{\mathrm{b}} \mathrm{d}\tau. \tag{B.30}$$

Substituting Equations (B.21) and (B.22) results in

$$\kappa_a \kappa_b \int \mathbf{F_a} \cdot \mathbf{F_b} \mathrm{d}\tau - \kappa_b^2 \int \psi_{\mathrm{a}} \psi_{\mathrm{b}} \mathrm{d}\tau = 0. \tag{B.31}$$

This relation shows that the $\mathbf{F_a}$'s must form an orthonormal set if the $\psi_{\mathrm{a}}$'s are orthonormal. Lastly, it can be shown that the $\mathbf{F_a}$'s are orthogonal to the solenoidal functions. The proof below uses one of the $\mathbf{E_a}$'s as an example.

$$\int \nabla \cdot (\psi_{\mathrm{a}} \mathbf{E}_{\mathrm{b}})\, \mathrm{d}\tau = \oint \psi_{\mathrm{a}} \mathbf{E}_{\mathrm{b}} \cdot \mathrm{d}\mathbf{a} = 0 \tag{B.32}$$

$$\begin{aligned} \int \nabla \cdot (\psi_{\mathrm{a}} \mathbf{E}_{\mathrm{b}})\, \mathrm{d}\tau &= \int (\nabla\psi_{\mathrm{a}}) \cdot \mathbf{E}_{\mathrm{b}} \mathrm{d}\tau + \int \psi_{\mathrm{a}} (\nabla \cdot \mathbf{E}_{\mathrm{b}})\, \mathrm{d}\tau \\ &= \kappa_a \int \mathbf{F_a} \cdot \mathbf{E_b} \mathrm{d}\tau \end{aligned} \tag{B.33}$$

$$\Rightarrow \int \mathbf{F_a} \cdot \mathbf{E_b} \mathrm{d}\tau = 0 \qquad \text{for all values of } a \text{ and } b. \tag{B.34}$$

In summary, any vector field inside of the bounded volume may now be represented by an appropriate linear combination of either the $\mathbf{E_a}$'s and $\mathbf{F_a}$'s or the $\mathbf{H_a}$'s and $\mathbf{F_a}$'s.

## B.2 Time Evolution of the Expansion Coefficients

The electric field, magnetic field, current density, and charge density in a cavity may now be written as linear combinations of the solenoidal and irrotational functions:

$$\mathbf{E} = \sum_a (e_a \mathbf{E_a} + f_a \mathbf{F_a}) \tag{B.35}$$

$$\mathbf{H} = \sum_a h_a \mathbf{H_a} \tag{B.36}$$

$$\mathbf{J} = \sum_a (j_a \mathbf{E_a} + g_a \mathbf{F_a}) \tag{B.37}$$

$$\rho = \sum_a r_a \psi_a. \tag{B.38}$$

If the only systems of interest are cavities in which no energy ever enters or leaves, then the time evolution of the expansion coefficients could be determined by simply substituting Equations (B.35) through (B.38) directly into Maxwell's equations. However, we would also like to describe systems in which energy does cross over the cavity boundary. For example, all metallic cavities have small conduction losses, therefore there must be a small tangential electric field on the surface where current is flowing. Power must be supplied to the cavity to compensate for these losses, so an input port must be provided. In both of these examples, there is now a region of the cavity where a component of $\mathbf{E} \times \mathbf{H}$ is normal to the boundary. The solenoidal and irrotational functions still form a complete set and can represent any field *within the original boundary* even for the case that power flows across the boundary. For example, if the wall losses are small then the electric field for the $a^{th}$ cavity mode would consist primarily of $\mathbf{E_a}$ plus relatively minor contributions from the other $\mathbf{E_a}$'s. The other $\mathbf{E_a}$'s allow the value of $\mathbf{E}$ to be finite right up to the bounding surface with arbitrarily small precision. However, all of the $\mathbf{E_a}$'s have zero tangential component on the bounding surface $S$. So while the value of $\mathbf{E}$ is correct at all points within the cavity, the tangential component must drop instantaneously to zero at the boundary $S$, therefore derivatives of the limiting function for $\mathbf{E}$ will not be correct at the cavity

surface. Stated more mathematically, the convergence of $\mathbf{E}$ is nonuniform for the case of wall losses. The nonuniform convergence implies that while $\mathbf{E}$ may be represented by a linear combination of the $\mathbf{E_a}$'s, the derivative of $\mathbf{E}$ may not generally be represented by the *same* linear combination of the derivatives of the $\mathbf{E_a}$'s. To handle the more general situation where power is able to flow into and out of the cavity, the curls and divergences which appear in Maxwell's equations must be expanded directly.

The coefficients in the expansion of $\nabla \times \mathbf{E}$ are found by calculating the values of $\int (\nabla \times \mathbf{E}) \cdot \mathbf{H_a} d\tau$ for every $a$. To calculate these integrals first note that

$$\begin{aligned} \nabla \cdot [\mathbf{E} \times (\nabla \times \mathbf{E_a})] &= (\nabla \times \mathbf{E_a}) \cdot (\nabla \times \mathbf{E}) - \mathbf{E} \cdot [\nabla \times (\nabla \times \mathbf{E_a})] \\ &= k_a \mathbf{H_a} \cdot (\nabla \times \mathbf{E}) - k_a^2 \mathbf{E} \cdot \mathbf{E_a}, \end{aligned} \tag{B.39}$$

so that

$$\int [\nabla \cdot [\mathbf{E} \times (\nabla \times \mathbf{E_a})] d\tau = \int k_a \mathbf{H_a} \cdot (\nabla \times \mathbf{E}) \, d\tau - k_a^2 \int \mathbf{E} \cdot \mathbf{E_a} d\tau. \tag{B.40}$$

The volume integral on the left may be converted to a surface integral:

$$\int [\nabla \cdot [\mathbf{E} \times (\nabla \times \mathbf{E_a})] d\tau = \oint [\mathbf{E} \times (\nabla \times \mathbf{E_a})] \cdot d\mathbf{a} = k_a \oint (\mathbf{E} \times \mathbf{H_a}) \cdot \mathrm{d}\mathbf{a}. \tag{B.41}$$

Substituting the right side of this relation and $e_a = \int \mathbf{E} \cdot \mathbf{E_a} d\tau$ into Equation (B.40) results in

$$\int (\nabla \times \mathbf{E}) \cdot \mathbf{H_a} d\tau = k_a e_a + \oint (\mathbf{E} \times \mathbf{H_a}) \cdot \mathrm{d}\mathbf{a}, \tag{B.42}$$

The left-hand side of the above equation is the $a^{\text{th}}$ coefficient of $\nabla \times \mathbf{E}$, so

$$\nabla \times \mathbf{E} = \sum_a \mathbf{H_a} [k_a e_a + \oint (\mathbf{E} \times \mathbf{H_a}) \cdot \mathrm{d}\mathbf{a}]. \tag{B.43}$$

The second term on the right side of Equation (B.43) is zero when $\mathbf{E}$ has no component tangential to the surface $S$. The expansion for $\nabla \times \mathbf{E}$ is then what is obtained if the

curl of both sides of Equation (B.35) is taken. A similar derivation for the expansion coefficients of $\nabla \times \mathbf{H}$ results in

$$\nabla \times \mathbf{H} = \sum_{a} \mathbf{E_a}[k_a h_a - \oint (\mathbf{E_a} \times \mathbf{H}) \cdot \mathrm{da}]. \tag{B.44}$$

The coefficients in the expansion of $\nabla \cdot \mathbf{E}$ are found by calculating the values of $\int (\nabla \cdot \mathbf{E}) \psi_a \mathrm{d}\tau$ for every $a$. We can write

$$\nabla \cdot (\psi_a \mathbf{E}) = \psi_a (\nabla \cdot \mathbf{E}) + \mathbf{E} \cdot (\nabla \psi_a) = \psi_a (\nabla \cdot \mathbf{E}) + \kappa_a \mathbf{E} \cdot \mathbf{F_a} \tag{B.45}$$

so that

$$\int \nabla \cdot (\psi_a \mathbf{E}) \, \mathrm{d}\tau = \oint \psi_a \mathbf{E} \cdot d\mathbf{a} = 0 \tag{B.46}$$

and hence

$$\int (\nabla \cdot \mathbf{E}) \psi_a d\tau = -\kappa_a \int \mathbf{E} \cdot \mathbf{F_a} \mathrm{d}\tau = -\kappa_a f_a. \tag{B.47}$$

**Gauss's Law**

Substituting Equations (B.47) and (B.38) into $\nabla \cdot \mathbf{E} = \frac{\rho}{\epsilon}$ gives

$$\sum_{a} -\kappa_a f_a \psi_a = \frac{1}{\epsilon} \sum_{a} r_a \psi_a. \tag{B.48}$$

Orthogonality implies that

$$-\kappa_a f_a = \frac{r_a}{\epsilon}. \tag{B.49}$$

The equation of continuity of charge may be used to eliminate $r_a$ from Equation (B.49). We can write

$$\nabla \cdot \mathbf{J} + \frac{\partial \rho}{\partial t} = 0. \tag{B.50}$$

Expanding this equation gives

$$\sum_{\mathbf{a}} -\kappa_{\mathbf{a}} g_{\mathbf{a}} \psi_{\mathbf{a}} + \sum_{\mathbf{a}} \psi_{\mathbf{a}} \frac{dr_{\mathbf{a}}}{dt} = 0. \tag{B.51}$$

Again using orthogonality, we infer that

$$\kappa_{\mathbf{a}} g_{\mathbf{a}} = \frac{dr_{\mathbf{a}}}{dt}. \tag{B.52}$$

Taking the derivative of Equation (B.49) and substituting the relation above gives

$$g_{\mathbf{a}} = -\epsilon \frac{df_{\mathbf{a}}}{dt}. \tag{B.53}$$

### Ampere/Maxwell Relation

Substituting Equations (B.44), (B.37), and (B.35) into $\nabla \times \mathbf{H} = \mathbf{J} + \epsilon \frac{\partial \mathbf{E}}{\partial t}$ gives

$$\sum_{\mathbf{a}} \mathbf{E}_{\mathbf{a}} [k_{\mathbf{a}} h_{\mathbf{a}} - \oint (\mathbf{E}_{\mathbf{a}} \times \mathbf{H}) \cdot d\mathbf{a}] = \sum_{\mathbf{a}} \mathbf{E}_{\mathbf{a}} \left( j_{\mathbf{a}} + \epsilon \frac{de_{\mathbf{a}}}{dt} \right) + \mathbf{F}_{\mathbf{a}} \left( g_{\mathbf{a}} + \epsilon \frac{f_{\mathbf{a}}}{dt} \right). \tag{B.54}$$

Equating coefficients of $\mathbf{F}_{\mathbf{a}}$ simply reproduces Equation (B.53) while equating coefficients of $\mathbf{E}_{\mathbf{a}}$ results in

$$k_{\mathbf{a}} h_{\mathbf{a}} = j_{\mathbf{a}} + \oint (\mathbf{E}_{\mathbf{a}} \times \mathbf{H}) \cdot \mathbf{da} + \epsilon \frac{de_{\mathbf{a}}}{dt}. \tag{B.55}$$

The first two terms on the right side of Equation (B.55) show that the magnetic field of the $a^{\text{th}}$ mode will be excited whenever the volume current or surface current overlap with the electric field of the $a^{\text{th}}$ mode.

### Faraday's Law

Substituting Equations (B.43) and (B.36) into $\nabla \times \mathbf{E} = -\mu \frac{\partial \mathbf{H}}{\partial t}$ gives

$$\sum_{\mathbf{a}} \mathbf{H_a} \left[ k_{\mathbf{a}} e_{\mathbf{a}} + \oint (\mathbf{E} \times \mathbf{H_a}) \cdot \mathbf{da} \right] = \sum_{a} -\mathbf{H_a} \mu \frac{dh_{\mathbf{a}}}{dt}. \tag{B.56}$$

Hence

$$k_{\mathbf{a}} e_{\mathbf{a}} = - \oint (\mathbf{E} \times \mathbf{H_a}) \cdot \mathbf{da} - \mu \frac{dh_{\mathbf{a}}}{dt}. \tag{B.57}$$

### Decoupled Equations for Time-Dependent Coefficients

A single differential equation describing the $h_{\mathbf{a}}$'s may now be found by differentiating Equation (B.57) and substituting the result into Equation (B.55),

$$\frac{de_{\mathbf{a}}}{dt} = -\frac{1}{k_{\mathbf{a}}} \frac{d}{dt} \oint (\mathbf{E} \times \mathbf{H_a}) \cdot \mathbf{da} - \frac{\mu}{k_{\mathbf{a}}} \frac{d^2 h_{\mathbf{a}}}{dt^2}, \tag{B.58}$$

$$k_{\mathbf{a}} h_{\mathbf{a}} = j_{\mathbf{a}} + \oint (\mathbf{E_a} \times \mathbf{H}) \cdot \mathbf{da} - \frac{\epsilon}{k_{\mathbf{a}}} \frac{d}{dt} \left[ \oint (\mathbf{E} \times \mathbf{H_a}) \cdot \mathbf{da} \right] - \frac{\epsilon \mu}{k_{\mathbf{a}}} \frac{d^2 h_{\mathbf{a}}}{dt^2}, \tag{B.59}$$

$$\Rightarrow \frac{d^2 h_{\mathbf{a}}}{dt^2} + \omega_a^2 h_{\mathbf{a}} = \frac{\omega_a^2}{k_{\mathbf{a}}} \left[ j_{\mathbf{a}} + \oint (\mathbf{E_a} \times \mathbf{H}) \cdot \mathbf{da} \right] - \frac{1}{\mu} \frac{d}{dt} \left[ \oint (\mathbf{E} \times \mathbf{H_a}) \cdot \mathbf{da} \right] \tag{B.60}$$

where $\omega_a^2 = \frac{k_{\mathbf{a}}^2}{\epsilon \mu}$. Total time derivatives have been used since the expansion coefficients and the surface integrals do not depend on the spatial coordinates. The same procedure results in a similar expression for the $e_{\mathbf{a}}$'s:

$$\frac{d^2 e_{\mathbf{a}}}{dt^2} + \omega_a^2 e_{\mathbf{a}} = -\frac{1}{\epsilon} \frac{d}{dt} \left[ j_{\mathbf{a}} + \oint (\mathbf{E_a} \times \mathbf{H}) \cdot \mathbf{da} \right] - \frac{\omega_a^2}{k_{\mathbf{a}}} \left[ \oint (\mathbf{E} \times \mathbf{H_a}) \cdot \mathbf{da} \right]. \tag{B.61}$$

# Appendix C

# Analysis of CW RF Measurements

This section describes how measured values from the cavity tests are used to calculate the $Q_0$ of the cavity and is reproduced, almost verbatim, from notes by Walter Hartung [28]. Other derivations and discussions of formulae for analysis of RF measurements can be found in the literature [29, 30].

In a CW measurement, we are able to measure the following quantities:

$P_f =$ forward power,

$P_r =$ reverse power,

$P_t =$ transmitted power,

$f =$ frequency.

Additional information is needed to calculate the stored energy, field, and $Q_0$ of the cavity. We can obtain additional information by doing a "field level calibration" at low power. This is done with modulated measurements to supplement the CW measurements. With modulated measurements, the following quantities may be calculated:

$Q_{ext,1} =$ strength of the input coupler,

$Q_{ext,2} =$ strength of the pickup coupler.

A numerical calculation of the field pattern (using SUPERFISH, Analyst, etc.) for the mode of interest is also needed to find out the relationship between the stored energy and the field. The field is proportional to the square root of the stored energy $U$:

$$E_{\mathrm{acc}} \propto \sqrt{U}. \tag{C.1}$$

The peak surface fields, $B_{\mathrm{p}}$ and $E_{\mathrm{p}}$, are proportional to the square root of $U$ also. With the output of the numerical calculation, any field of interest may be found from $U$.

If $Q_{\mathrm{ext},1}$ and $Q_{\mathrm{ext},2}$ are obtained from a low-power modulated field calibration, the CW measurements are overdetermined. So there is more than one way to calculate the stored energy, field, and $Q_0$. In principle, different methods should give the same result. In practice, the answers may be different due to systematic errors.

## C.1 Direct Method

We calculate the dissipated power $P_{\mathrm{d}}$ by subtraction,

$$P_{\mathrm{d}} = P_{\mathrm{f}} - P_{\mathrm{r}} - P_{\mathrm{t}}. \tag{C.2}$$

The stored energy is related to the transmitted power via the coupling strength of the pickup,

$$Q_{\mathrm{ext},2} \equiv \frac{\omega U}{P_{\mathrm{t}}}. \tag{C.3}$$

So, knowing $Q_{\mathrm{ext},2}$ and $\omega = 2\pi f$, $U$ may be calculated,

$$U = P_{\mathrm{t}} \left( \frac{Q_{\mathrm{ext},2}}{\omega} \right). \tag{C.4}$$

Having $P_{\mathrm{d}}$ and $U$, $Q_0$ may be calculated directly via

$$Q_0 = \frac{\omega U}{P_{\mathrm{d}}}. \tag{C.5}$$

In terms of measured quantities, the intrinsic $Q$ is

$$Q_0 = Q_{\mathrm{ext},2}\left(\frac{P_{\mathrm{t}}}{P_{\mathrm{f}} - P_{\mathrm{r}} - P_{\mathrm{t}}}\right). \tag{C.6}$$

The field may be calculated from Equation (C.1), with the appropriate conversion factor. Advantages of the direct method include:

1. direct, easy to understand
2. knowledge of $Q_{\mathrm{ext},1}$ is unnecessary.

Disadvantages of the direct method include:

1. makes use of $P_{\mathrm{r}}$, which may have systematic error associated with it
2. relies on the difference between $P_{\mathrm{f}}$ and $P_{\mathrm{r}}$, which may be a small number when not close to unity coupling.

## C.2 Indirect Method Using $\frac{P_{\mathrm{t}}}{P_{\mathrm{f}}}$

An expression for $Q_0$ which does not involve $P_{\mathrm{r}}$ is desired. We begin with Equation (C.2), re-writing it in terms of scattering parameters,

$$|S_{11}| = \sqrt{\frac{P_{\mathrm{r}}}{P_{\mathrm{f}}}} \tag{C.7}$$

$$|S_{21}| = \sqrt{\frac{P_{\mathrm{t}}}{P_{\mathrm{f}}}}. \tag{C.8}$$

Equation (C.2) becomes

$$\frac{P_{\mathrm{d}}}{P_{\mathrm{f}}} = 1 - |S_{21}|^2 - |S_{11}|^2 \tag{C.9}$$

The input coupling coefficient $\beta_1$ depends on the reflection coefficient,

$$\beta_1 = \frac{\sqrt{P_f} \pm \sqrt{P_r}}{\sqrt{P_f} \mp \sqrt{P_r}} \tag{C.10}$$

$$\therefore \quad \beta_1 = \frac{1 \pm |S_{11}|}{1 \mp |S_{11}|}. \tag{C.11}$$

In the above equations, the upper sign applies when overcoupled and the lower sign applies when undercoupled. Solving for $|S_{11}|^2$ results in

$$|S_{11}|^2 = \left(\frac{1-\beta_1}{1+\beta_1}\right)^2. \tag{C.12}$$

Substituting this expression into Equation (C.9) and simplifying gives

$$\frac{P_d}{P_f} = \frac{4\beta_1}{(1+\beta_1)^2} - |S_{21}|^2 \tag{C.13}$$

It is not possible to measure $P_d$ directly, so it must be eliminated. It may be expressed in terms of $\beta_2$ and $|S_{21}|$,

$$\beta_2 = \frac{P_t}{P_d} \tag{C.14}$$

$$\therefore \quad \frac{P_d}{P_t} = \frac{1}{\beta_2} \tag{C.15}$$

$$\therefore \quad \frac{P_d}{P_f} = \frac{|S_{21}|^2}{\beta_2}. \tag{C.16}$$

Substituting this into Equation (C.13) results in

$$\frac{|S_{21}|^2}{\beta_2} = \frac{4\beta_1}{(1+\beta_1)^2} - |S_{21}|^2. \tag{C.17}$$

Define

$$|R_{21}| = |S_{21}|\sqrt{\frac{\beta_1}{\beta_2}} = |S_{21}|\sqrt{\frac{Q_{ext,2}}{Q_{ext,1}}}, \tag{C.18}$$

so that Equation (C.17) becomes,

$$|R_{21}|^2 = \frac{4\beta_1^2}{(1+\beta_1)^2} - \beta_2|R_{21}|^2, \tag{C.19}$$

so that

$$|R_{21}|\sqrt{1+\beta_2} = \frac{2\beta_1}{1+\beta_1}. \tag{C.20}$$

If $\beta_2 \ll 1$ (*i.e.* weakly-coupled pickup antenna), then

$$|R_{21}| \approx \frac{2\beta_1}{1+\beta_1}. \tag{C.21}$$

Solving for $\beta_1$, we obtain

$$\beta_1 \approx \frac{1}{\frac{2}{|R_{21}|} - 1}. \tag{C.22}$$

But $\beta_1 = \frac{Q_0}{Q_{\text{ext},1}}$, so Equation (C.22) reads

$$Q_0 \approx \frac{Q_{\text{ext},1}}{\frac{2}{|R_{21}|} - 1}. \tag{C.23}$$

Substituting Equations (C.18) and (C.8) into the last expression results in an explicit expression for $Q_0$,

$$Q_0 \approx \frac{Q_{\text{ext},1}}{2\sqrt{\frac{Q_{\text{ext},1}}{Q_{\text{ext},2}} \cdot \frac{P_\text{f}}{P_\text{t}}} - 1}. \tag{C.24}$$

Advantages of the indirect method include

1. does not use $P_\text{r}$, so systematic errors in $P_\text{r}$ measurement are avoided

2. does not rely on calculation of $P_\text{f} - P_\text{r}$, which may be problematic to use when not close to unity coupling.

Disadvantages of the indirect method include

1. derivation of formula is more complicated and its application may be less intu-

itive

2. must use both $Q_{\text{ext},1}$ and $Q_{\text{ext},2}$

3. assumes a weak pickup antenna

4. the formula may not work well when the cavity is strongly overcoupled.

## C.3 Graphical Assessment of Systematic Errors

The direct method gives

$$Q_0^{\text{direct}} = \frac{P_t Q_{\text{ext},2}}{P_f - P_r - P_t} = \frac{|S_{21}|^2 Q_{\text{ext},2}}{1 - |S_{11}|^2 - |S_{21}|^2}. \tag{C.25}$$

The indirect method gives,

$$Q_0^{\text{indirect}} \approx \frac{Q_{\text{ext},1}}{\frac{2}{|R_{21}|} - 1}. \tag{C.26}$$

Both methods should, in principle, give the same answer, therefore we should have,

$$Q_0^{\text{direct}} = Q_0^{\text{indirect}}, \tag{C.27}$$

which leads to,

$$\frac{Q_{\text{ext},2}|S_{21}|^2}{1 - |S_{21}|^2 - |S_{11}|^2} \approx \frac{Q_{\text{ext},1}}{\frac{2}{|R_{21}|} - 1} \quad \text{or} \quad \frac{|R_{21}|^2}{1 - |S_{21}|^2 - |S_{11}|^2} \approx \frac{1}{\frac{2}{|R_{21}|} - 1}. \tag{C.28}$$

Weak coupling was assumed for the pickup, so $1 - |S_{11}|^2 \gg |S_{21}|^2$ and to a good approximation,

$$\frac{|R_{21}|^2}{1 - |S_{11}|^2} \approx \frac{1}{\frac{2}{|R_{21}|} - 1}, \tag{C.29}$$

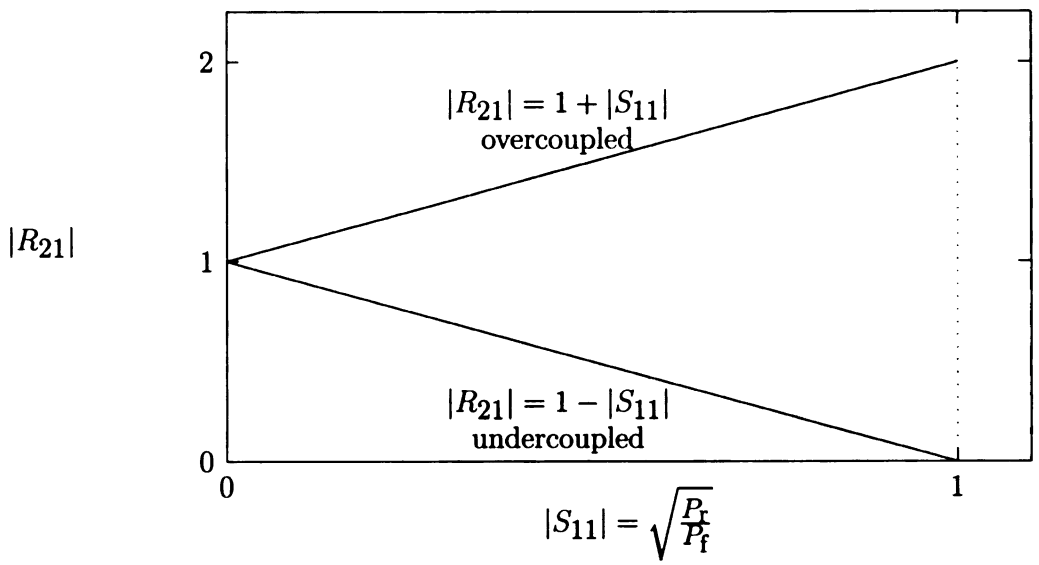


Figure C.1: Measured values of $Q_{ext,1}$ and $Q_{ext,2}$ may be checked for consistency by inspecting how closely the calculated value of $|R_{21}|$ lies on the "Duality Triangle".

therefore it follows,

$$1 - |S_{11}|^2 + |R_{21}|^2 - 2|R_{21}| \approx 0, \tag{C.30}$$

$$(1 - |R_{21}|)^2 \approx |S_{11}|^2, \tag{C.31}$$

$$1 - |R_{21}| \approx \pm|S_{11}|, \tag{C.32}$$

$$|R_{21}| \approx 1 \mp |S_{11}|. \tag{C.33}$$

Since $0 \leq |S_{11}| \leq 1$, Equation (C.33) tells us that the values of $|S_{11}|$ and $|R_{21}|$ should be on one of the two equal sides of an isosceles triangle. One might call this the "duality triangle" (see Figure C.1). When doing CW measurements, the values of $|S_{11}|$ and $|R_{21}|$ can be calculated. The proximity of these values to the duality triangle then indicates whether the values of $Q_{ext,1}$, $Q_{ext,2}$, $P_f$, $P_r$, and $P_t$ are all consistent.

# Bibliography


[1] Charles D. Bowman. Accelerator-driven systems for nuclear waste transmutation. *Annual Review of Nuclear and Particle Science*, 48:505–556, 1998.

[2] A. Bienenstock H. Winick. Synchrotron radiation research. *Annual Review of Nuclear and Particle Science*, 28:33–113, 1978.

[3] A.M. Sessler W.B. Colson. Free electron lasers. *Annual Review of Nuclear and Particle Science*, 35:25–54, 1985.

[4] K. Floettmann. The european xfel project. In *The 12th International Workshop on RF Superconductivity*, Ithaca, New York, July 2005.

[5] R.L. Kustom. An overview of the spallation neutron source project. In *The XX International Linac Conference:Monterey, CA*, number SLAC-R-561, pages 321–325, Stanford, California, 2000.

[6] G. Krafft L. Merminga, D. Douglas. High-current energy-recovering electron linacs. *Annual Review of Nuclear and Particle Science*, 53:387–429, 2003.

[7] P. Kneisel. Latest developments in superconducting rf structures for beta=1 particle acceleration. In *Proceedings of the European Particle Accelerator Conference*, Edinburgh, Scotland, 2006.

[8] Thomas Wangler. *RF Linear Accelerators.* John Wiley & Sons Inc., 1998.

[9] S.Y. Lee. *Accelerator Physics.* World Scientific, 1999. p. 7.

[10] Tom Hays Hasan Padamsee, Jens Knobloch. *RF Superconductivity for Accelerators.* John Wiley & Sons, Inc., 1998.

[11] L. Merminga *et al.* Scaling of wakefield effects in recirculating linacs. In *Proceedings of the Particle Accelerator Conference*, Chicago, 2001.

[12] Robert E. Collin. *Foundations of Microwave Engineering.* John Wiley & Sons, Inc., second edition, 2001. Section 3.7.

[13] David M. Pozar. *Microwave Engineering.* John Wiley & Sons, Inc., second edition, 1998.

[14] John C. Slater. *Microwave Electronics.* D. Van Nostrand Company, Inc., 1950. Chapter IV.

[15] Sol Gruner. Concepts and applications of energy recovery linacs (ERLs). In *Eighth Internaional Conference on Synchrotron Radiation Instrumentation*, San Francisco, California, August 2003.

[16] Ilan Ben-Zvi *et al.* Energy recovery linacs in high-energy and nuclear physics. *Nuclear Instruments and Methods in Physics Research*, 557, 2005.

[17] B. Aune *et al.* Superconducting tesla cavities. *Physical Review Special Topics-Accelerators and Beams*, 3, 2001.

[18] R.F. Holsinger K. Halbach. Superfish- a computer program for evaluation of rf cavities with cylindrical symmetry. *Particle Accelerators*, 7(4):213–222, 1976.

[19] *et al.* R. Calaga. Study of higher order modes in high current multicell srf cavities. *Collider Accelerator Dept. BNL C-A/AP/111*, 2003.

[20] http://www.staarinc.com.

[21] H. Padamsee *et al.* Overview of the cornell erl injector cryomodule. In *Proceedings of the Particle Accelerator Conference*, 2003.

[22] Robert Wagner. Proton driver $\beta = 0.81$ cavities project. The descriptiopn of the e-beam welding is found in this summary., December 2005.

[23] T.L. Grimm *et al.* Experimental study of an 805 mhz cryomodule for the rare isotope accelerator. In *Proceedings of Linac 2004: XXII International Linear Accelerator Conference: Lbeck, Germany*, 2004.

[24] G. Ciovati *et al.* Superconducting prototype cavities for the spallation neutron source (SNS) project. In *Proceedings of the 2001 Particle Accelerator Conference: Chicago, Illinois*, 2001.

[25] W. Hartung *et al.* Niobium quarter-wave resonator development for the rare isotope accelerator. In *The* $11^{th}$ *Workshop on RF Superconductivity*, Travemunde, Germany, September 2003.

[26] Y.H. Chin. Users guide for abci version 8.8. Technical Report LBL-35258, Lawerence Berkeley Laboratory, 1994.

[27] A. Mosnier *et al.* Design of a heavilty damped superconducting cavity for soleil. In *Proceedings of the Particle Accelerator Conference*, Vancouver, 1997.

[28] Walter Hartung. Analysis of cw measurements on srf cavities. private communication, September 2006.

[29] Tom Powers. Theory and practice of cavity rf test systems. In *The 12th International Workshop on RF Superconductivity*, Ithaca, New York, July 2005.

[30] Jens Knobloch. Basic concepts of measurements made on superconducting rf cavities. Technical Report SRF 910927-07, Cornell Laboratory of Nuclear Studies, August 1991.